
CONVECTION AND OUTFLOWS FROM
ACCRETING NEUTRON STARS DURING
THERMONUCLEAR FLASHES

A dissertation presented by

Simon Guichandut

to the Department of Physics

in partial fulfillment of the requirements for the degree of

Doctor of Philosophy

McGill University

Montréal, Québec

December 2024

© 2024 — Simon Guichandut

All rights reserved.

Convection and Outflows from Accreting Neutron Stars during Thermonuclear Flashes

Abstract

Type I X-ray bursts are the most common type of high energy transient in the Universe. They arise from thermonuclear runaway events in the atmospheres of neutron stars that accrete hydrogen and helium from a companion star. In some instances, the energy liberated can be so high that the luminosity of the star temporarily exceeds the Eddington limit, pushing the photosphere away from the neutron star surface. In these photospheric radius expansion (PRE) bursts, a radiatively-driven wind ejects matter, progressively revealing deeper layers of the atmosphere. In this thesis, we use numerical simulations to model these bursts and attempt to make connections to what is seen through X-ray telescopes. Our first models are steady-state solutions for the PRE outflow, including general relativity and a transition from optically thick to optically thin using flux-limited diffusion. With these, we investigate the potential sizes of blueshifts and redshifts of spectral features from metal absorption, and the evolution of the photospheric radius as the luminosity transitions from sub- to super-Eddington. We also discuss the potential application of this grid of models as an outer boundary for more detailed simulations of the burning layer. Next, we perform full time-dependent simulations of a PRE burst using one-dimensional stellar evolution calculations. These start with accretion onto the star, track the detailed nuclear burning of the gas, the ignition of the burst, and the outflow. We show that convection at the onset of the burst leaves an imprint onto the lightcurve, namely a short pause during the initial rise, as the wind ejects a thin hydrogen shell before the helium envelope. We find that outcomes of the mixing and the lightcurve are sensitive to the treatment of convection within the code. This is because one-dimensional theories of convection are not well suited to situations of rapid nuclear burning. Therefore, we move on to two-dimensional simulations of convection, using low Mach number hydrodynamics. We find significant differences in the behaviour of convection compared one-dimensional results. We analyze the details of the mixing near the convective boundary, as overshooting fluid elements penetrate the stable layer. These motions carry chemical species out of and into the convective zone, changing the nature of the nuclear burning. They also accelerate the growth of the convection zone by cooling the stable layer. Our results are especially relevant to recent and upcoming burst observations with the NICER telescope.

Convection et Écoulements d'Étoiles à Neutrons durant des Explosions Thermonucléaires

Abrégé

Les sursauts rayons X de type I sont les phénomènes transitoires à haute énergie les plus fréquents dans l'Univers. Ils proviennent de réactions thermonucléaires dans l'atmosphère d'étoiles à neutrons qui accrètent de l'hydrogène et de l'hélium d'une étoile compagne. Dans certains cas, l'énergie libérée est si grande qu'elle peut excéder la limite d'Eddington, repoussant la photosphère de l'étoile hors de sa surface. Dans ces sursauts à expansion du rayon photosphérique (ERP), un vent propulsé par la radiation éjecte de la matière, révélant progressivement les couches profondes de l'atmosphère. Dans cette thèse, nous utilisons des simulations numériques pour modéliser ces sursauts, en tentant d'établir des liens avec ce qui est observé au travers des télescopes rayons X. Nos premiers modèles sont des solutions stationnaires des écoulements durant l'ERP, incluant la relativité générale et une transition de l'optiquement épais à l'optiquement mince par diffusion à flux limité. Avec ceux-ci, nous étudions l'ampleur des décalages vers le bleu et le rouge des caractéristiques spectrales dues à l'absorption des métaux, ainsi que l'évolution du rayon photosphérique à mesure que la luminosité passe de sous à super-Eddington. Nous discutons également l'applicabilité de ces modèles en tant que condition limite pour des simulations plus détaillées de la couche enflammée. Ensuite, nous effectuons des simulations temporelles complètes d'un sursaut ERP à l'aide de calculs d'évolution stellaire. Ces simulations débutent par l'accrétion sur l'étoile, suivent la combustion nucléaire, le déclenchement du sursaut, et l'écoulement. Nous démontrons que la convection à l'amorce du sursaut laisse une empreinte sur la courbe de lumière, notamment une courte pause durant la montée initiale, à mesure que le vent éjecte une mince couche d'hydrogène avant l'enveloppe d'hélium. Nous constatons que le résultat de la convection et la courbe de lumière sont sensibles au traitement de la convection par le code. Cela s'explique par le fait que les théories uni-dimensionnelles de la convection ne sont pas adaptées au situations de combustion nucléaire rapide. C'est pourquoi nous passons à des simulations à deux dimensions de la convection, en utilisant l'hydrodynamique à bas nombre de Mach. Nous constatons des différences importantes dans le comportement de la convection comparé aux résultats en une dimension. Nous analysons les détails du mélange près des frontières de la zone de convection, alors que des éléments de fluide pénètrent la couche stable. Ces mouvements transportent des espèces chimiques à l'extérieur et à l'intérieur de la zone de convection, ce qui change la nature de la combustion nucléaire. Ils accélèrent également la croissance de la zone de convection en refroidissant la couche stable. Nos résultats sont particulièrement pertinents pour les observations récentes et à venir de sursauts avec le télescope NICER.

Acknowledgments

This thesis is the culmination of 6 years of work. Besides my own effort, this would not have been possible without the help of many people around me.

First and foremost, I wish to thank my advisor Andrew Cumming for his support over the years. When I first stepped into his office as a recent engineering graduate, I had essentially no clue about astrophysics. I just thought it sounded interesting! As he started telling me about neutron stars and stellar winds with his usual enthusiasm, I was instantly captivated, and knew I had made the right decision. As an advisor, Andrew has forged my approach to problem-solving. I aspire, only rarely with success, to match his level of intuition for physics. More importantly, he inspired confidence in myself and encouraged me to step out of my comfort zone.

The Trottier Space Institute has been a wonderful place to work at (and spend countless hours) over the years. Thank you to all of the professors, administrative staff, and postdocs, for fostering a community where we can all learn from each other. Thank you to all of my student peers and friends from the TSI for walking down the thorny road of grad school alongside me, reminding me not to take things too seriously and to have fun.

I thank Mike Zingale and his group for welcoming me at Stony Brook during the spring of 2023. They helped make my time there truly enriching and beneficial to my PhD. I am grateful to the Centre de Recherche en Astrophysique du Québec whose financial support made this experience possible.

Finally, I must thank Rafael Fuentes, my mentor, partner in office antics, and great friend. Thank you for all the memorable fun times, many enlightening scientific discussions, and for always encouraging me to be at my best.



On dit qu'il faut tout un village pour élever un enfant; je dirais que c'est aussi le cas pour former un doctorant. Merci à tous mes amis qui m'ont soutenu et divertie durant ces années. Merci à mon frère Julien, à mes soeurs Marie Anne et Laurence, et à tout le reste de ma grande famille, pour leurs encouragements. Merci à Laura pour son soutien indéfectible, en particulier au cours des derniers mois durant lesquels elle m'a permis de rester sain d'esprit et de corps. À vous tous, merci de m'avoir aidé à garder les deux pieds sur Terre pendant que ma tête était dans les étoiles.

Le dernier remerciement est pour ma mère Diane, qui aura été la source de ma curiosité et de ma détermination. Cette thèse lui est dédiée.

Contribution to Original Knowledge

The work presented in this thesis expands upon previous models and simulations of bursting neutron star atmospheres, and presents previously unknown or underappreciated physical elements, which impact not only our theoretical understanding of these events, but also our observational interpretations.

Chapter 2, “Expanded Atmospheres and Winds in Type I X-Ray Bursts from Accreting Neutron Stars” ([Guichandut et al. 2021](#)), revisits old models of radiation-driven outflows. For the first time, we include both sub-Eddington expanded atmospheres and super-Eddington winds in the same grid of models, using the same theoretical framework. We include a transition from optically thick to optically thin, which had not been considered before for expanded atmospheres, and makes an important difference for the photospheric radius. We demonstrate an important issue with the touchdown method, which has been used to infer the radii of multiple neutron stars.

Chapter 3, “The Imprint of Convection on Type I X-Ray Bursts: Pauses in Photospheric Radius Expansion Lightcurves” ([Guichandut & Cumming 2023](#)), presents the first full time-dependent simulations of the ejection of a hydrogen shell in Type I X-ray bursts. We make a clear connection between convection at the onset of the burst and the observed lightcurve. We add one more example to the list of astrophysical situations where the mixing-length theory of convection has trouble resolving the full dynamics of mixing, due to the rapid nuclear burning.

Chapter 4, “Hydrodynamical simulations of proton ingestion flashes in Type I X-ray Bursts” ([Guichandut et al. 2024](#)), is the fourth installment of low Mach number number simulations of Type I X-ray burst convection in two dimensions. For the first time, our setup includes layers of different compositions, which is relevant to many bursts occurring in nature. We show how the entrainment of new fuel from the upper layer into the convection zone affects its dynamics. We also outline a mechanism for the growth of the convection zone which had not been discussed previously in this context.

Contribution of Authors

This thesis is comprised of three original papers for which I am the lead author. Professor Andrew Cumming, my thesis advisor, was involved in all stages of the research and writing of these works and this thesis.

CHAPTER 2

This chapter was published as: Guichandut, Cumming, Falanga, Li and Zamfir, *Expanded Atmospheres and Winds in Type I X-Ray Bursts from Accreting Neutron Stars*, The Astrophysical Journal, 914, 49, June 2021.

Maurizio Falanga was involved in early discussions on observational motivations for this work. Michael Zamfir created an initial version of Figure 2.12 which also motivated this project. Zhaosheng Li wrote a code which was used as a starting point for the calculations.

CHAPTER 3

This chapter was published as: Guichandut, Cumming, *The Imprint of Convection on Type I X-Ray Bursts: Pauses in Photospheric Radius Expansion Lightcurves*, The Astrophysical Journal, 954, 54, September 2023.

Andrew Cumming provided the initial set of MESA simulations and assisted in adapting them to the new physical scenario.

CHAPTER 4

This chapter was published as: Guichandut, Zingale, and Cumming, *Hydrodynamical simulations of proton ingestion flashes in Type I X-ray Bursts* , The Astrophysical Journal, 975, 250, November 2024.

Michael Zingale assisted in all aspects of developing and running the simulations in this project, and is a core developer of the code being used, MAESTROeX.

List of Abbreviations

- LMXB** Low-Mass X-ray Binary
PRE Photospheric Radius Expansion
GR General Relativity
FLD Flux-Limited Diffusion
MLT Mixing-Length Theory
EoS Equation of State
NICER Neutron Star Interior Composition Explorer
RXTE Rossi X-ray Timing Explorer
1D 1-Dimensional
2D 2-Dimensional
3D 3-Dimensional

List of Figures

1.1	Light curve of a PRE burst from 4U 1820–30 and how it depends on the instrumental spectral range. The solid line shows the count rate seen by NICER, while the gray shaded area shows the count rate (scaled up by a factor of 5) for instruments with no soft X-ray response. The dotted line shows the count rate for the persistent emission prior to the burst. Adapted from Figure 1 of Keek et al. (2018).	15
1.2	Fit residuals of the absorbed blackbody model for the stronger (pair 1) and weaker (pair 2) PRE bursts from 4U 1820–30. In the bottom panel, the residuals are added after the pair 2 residuals have been shifted by the best fitting line ratio of 1.046. An emission line is seen at 1 keV, and absorption lines are seen at 1.7 and 3 keV. From Figure 8 of Strohmayer et al. (2019).	16
1.3	PRE burst from SAX J1808.4–3658. The gray band in the inset shows the location of the pause. Adapted from Figure 1 of Bult et al. (2019)	17
1.4	Schematic of a PRE burst with relevant scales in the different regions, notable locations, and the aspects that are treated in each chapter. .	18
2.1	Radial profiles of the temperature (top left), velocity (top right), density (bottom left) and flux-energy ratio (bottom right), for pure helium winds (blue) and envelopes (red). Crosses and dots indicate the positions of the sonic points and photospheric radii respectively. Following the arrow direction, the winds have mass-loss rates $\log \dot{M} = (17.25, 17.5, 17.75, 18.0, 18.25, 18.5)$ and base luminosities $L_b^\infty / L_{\text{Edd}} = (1.10, 1.17, 1.30, 1.51, 1.89, 2.55)$. The envelopes have photospheric radii $r_{\text{ph}} = (13, 15, 20, 30, 40, 50)$ km, and luminosities $L^\infty / L_{\text{Edd}} = (0.89, 0.92, 0.95, 0.98, 0.99, 1.00)$. The black arrows in the bottom right panel point toward the optically thick and thin limits. .	41

2.2	Gradients of the temperature, density and velocity for the same wind and envelope models as in Figure 2.1. Crosses and dots mark the locations of r_s and r_{ph} respectively. Blue arrows show the direction of increasing \dot{M} for winds.	42
2.3	Density-temperature profiles of the same wind and envelope models as in Figure 2.1. Crosses and dots mark the locations of r_s and r_{ph} . Blue and red arrows show the direction of increasing \dot{M} and r_{ph} for winds and envelopes respectively. The black lines indicate the points of transition from one pressure regime to another. $P_{\text{nd}} \propto T\rho$ and $P_{\text{d}} \propto \rho^{5/3}$ are the pressures of non-degenerate and degenerate electrons.	43
2.4	Density profiles of the luminosity in the same wind and envelope models as in Figure 2.1. Crosses and dots mark the locations of r_s and r_{ph} . Blue and red arrows show the direction of increasing \dot{M} and r_{ph} for winds and envelopes respectively. The dashed black line denotes $L = L_{\text{cr}}$. The inset zooms in to the locations of the wind sonic points and envelope photospheres.	43
2.5	Optical depth given by $\tau^* \equiv \rho\kappa r$ and τ (Equation (2.25)) throughout the wind (blue) and envelope (red) models. The wind models shown are $\log \dot{M} = (17, 18, 18.5)$, left to right), the envelope models are $r_{\text{ph}} = (15, 30, 60)$ km. Crosses and dots mark the locations of r_s and r_{ph} . The dotted lines mark specific values of $2/3$ and 3	45
2.6	Values of the mass-loss rate \dot{M} as a function of the nuclear energy produced at the base, according to Equation (2.50). The right axis shows values of β at the wind base. The dashed red lines mark the energy released by complete burning of helium to carbon and complete burning of helium to iron group elements.	47
2.7	Ratio of predicted mass-loss rates from Equation (2.2) to our model values, $\xi \equiv (L_b^\infty - L_{\text{Edd}})/(GM\dot{M}/R)$, as a function of the base luminosity redshifted to infinity.	49
2.8	Solution space for the base luminosity as seen by observers at infinity, for both winds (blue) and envelopes (red). Eddington luminosity is marked by the vertical black dashed line. <i>Top</i> : Temperature at the base. Mass-loss rates are indicated at various points for the winds. <i>Middle</i> : Sonic and photospheric radii of solutions. <i>Bottom</i> : Characteristic timescales of the solutions (see Section 2.4.2).	51

2.9	The energy per unit mass as a function of mass coordinate compared to an envelope with $r_{\text{ph}} = 12.005$ km. This shows the energy that must be given to the envelope above each mass coordinate in order to expand outward. The mass coordinate m measures the mass contained above a given point (to the photosphere). The total mass of the envelope is $\approx 10^{21}$ g.	56
2.10	Photospheric radii of wind and envelope models for neutron stars with varying masses and radii. The solid black line represents the models shown throughout this paper.	58
2.11	Wind spectral shifts, as a function of the radial coordinate for the $\log \dot{M} = 18$ model (top), and as a function of \dot{M} at the photosphere (bottom).	61
2.12	Difference between the photospheric (touchdown) radius based on the luminosity (top) and observed effective temperature (bottom). The dotted line in the top panel represents Newtonian atmospheres, for which we derive an analytical formula in Appendix 2.7.4. The dashed line in the bottom panel gives the color temperature of the atmosphere with the correction factor of Pavlov et al. (1991).	64
2.13	Parameter spaces for the wind (left) and envelope (right) models. The black lines trace points which allow a transition to optically thin and non-diverging integration to infinity. The thicker black lines are labelled by the mass-loss rates (in g s^{-1}) for winds, and the photospheric radii (in km) for envelopes. The blue and red lines trace out the points which satisfy the surface boundary condition.	73

- 3.1 Diagram illustrating the three main stages of the mixed H/He burst. *A*) As hydrogen burns stably throughout accretion, distinct hydrogen and helium-rich layers build up in the envelope, their boundary being at a known column depth of y_d (Equation (3.2)). We are interested in bursts that ignite at $y > y_d$ (red color indicates nuclear burning). *B*) Heat from nuclear burning creates a growing convection zone (blue semicircles) which penetrates into the H-rich layer, resulting in additional nuclear burning. *C*) As the convection zone retreats, it leaves behind a layer of constant hydrogen fraction at a column $y_{c,\min} < y_d$, a mixed H-He layer and nuclear ashes at depth. Winds progressively eject the layers, up to a column $y_w > y_{c,\min}$, during which the observed luminosity at infinity is the Eddington luminosity, which depends on the hydrogen fraction X of the material. Since X is initially constant, we first observe a pause after the initial burst rise. After the H layer is ejected, the luminosity once again rises in a manner that depends on the hydrogen gradient dX/dy . See text for further details. 86
- 3.2 Composition profiles before (left) and after (right) the thermonuclear flash, which ignites at $t = t_0$. The lines for different elements have the same color in left and right panels. In the ~ 1.4 s to reach the Eddington luminosity, convection has significantly mixed the He and H layers. Dotted lines show the depletion column y_d (left) and the minimum extent of convection $y_{c,\min}$ (right). All runs shown in this paper begin at the ignited model $t = t_0$, which the left panel leads up to. The panel on the right shows the result of mixing using the Schwarzschild criterion prescription for convective boundaries (see Section 3.3.2). . . 90
- 3.3 Kippenhahn diagrams for the Schwarzschild run, centered on the moment of collision between the convection zone and the H layer. The bottom panel is zoomed into a 1.5 ms window following the collision. The color scale traces the energy generation or loss (nuclear burning minus all neutrino losses), while the green hatches mark the convection zones. The solid black lines show the location of the depletion depth y_d . In the top panel, the dashed line shows the luminosity coming out of the atmosphere, normalized by the Eddington luminosity of the accreted gas (scale on the right-hand side). In the bottom panel, it shows the integrated nuclear power ($\int dm \epsilon_{\text{nuc}}$). Moments where certain reactions dominate are labeled (see Section 3.3.2). 92

3.4 Kippenhahn diagram for the Schwarzschild run as in Figure 3.3, now with the color scale representing the hydrogen abundance. The solid black and gray lines show y_d and $y_{c,\min}$ (same values as in Figure 3.2). The dashed line shows the relative change in the total mass of hydrogen at a given time compared to the initial amount at ignition (scale on the right-hand side).	95
3.5 The mass-loss rate of the wind as a function of time for the Schwarzschild run, in solid lines. The different colors show \dot{M} evaluated with Equation (3.4) at different locations (see text). The dashed lines show the ejected column y_{ej} (scale on the right-hand side). The red shaded region marks the pause in the lightcurve (bottom panel of Figure 3.6).	97
3.6 Results of the Schwarzschild run. <i>Top:</i> Hydrogen profile after convective mixing. To avoid numerical difficulties during the hydrodynamic wind (see Section 3.3.3), the profile was smoothed using a monotonic cubic spline. The dashed lines show the minimum column reached by convection $y_{c,\min}$, and the total column ejected by winds y_w . <i>Bottom:</i> Lightcurve of the burst. The pause occurs after surpassing L_{Edd} of the accreted material ($X = 0.7$, bottom dotted line). The following rise takes place over a much longer timescale since $y_w \gg y_{c,\min}$. In general, the outgoing luminosity follows the Eddington luminosity of the material which is currently being ejected (blue dotted line), which we can track using $y_{\text{ej}}(t)$ (see Section 3.3.4).	98
3.7 Results for all convective prescriptions and spatial resolutions tested in this work. <i>Left:</i> Mass fraction of ^1H in the atmosphere after the convective rise and before the ejection by winds. The circles label the locations of y_w resulting from each simulations. The black line shows the hydrogen gradient at ignition, from which all runs start. <i>Right:</i> Lightcurve of the bursts. The dotted lines mark the locations of L_{Edd} for $X = 0.7$ and $X = 0$, as in Figure 3.6. Some simulations could not integrate through the decay phase and were stopped short at the “x” symbols. The inset zooms in on the pauses.	104

4.1	Initial model from MESA (dash-dotted lines), and the initial model A fed into the fluid simulations (solid lines). The top panel shows the temperature profile as a function of height. The bottom panel shows the composition profiles of the main chemical species, where the green color combines all CNO species. The offset in the position of the solar layer is due to the temperature kick given to the initial fluid model. An alternate initial model (model B) including deep carbon is shown in the dotted lines for CNO and helium mass fractions. See Appendix 4.5 for details.	121
4.2	Peak values of the temperature (left axis, solid lines) and mach number (right axis, dashed lines) as a function of time for the same burst at different resolutions.	125
4.3	Flow, burning, and composition at different times in the 3 cm MAESTROeX simulation of model A. From top to bottom: vorticity, burning rate, mass fraction of hydrogen, mass fraction of carbon. Note the different scales in the bottom two rows. The left column is during the initial growth of the convection zone in the helium layer, the middle column is roughly at the collision with the hydrogen layer, and the right column is later during the expansion into the hydrogen. An animated version of this figure is available in the online journal.	127
4.4	Evolution of the temperature as a function of column depth (note that the x-axis is reversed), at intervals of 10 ms. The colors get darker as time increases. The labeled and thicker lines are the three times from Figure 4.3. The circle and square markers show the convective boundaries according to the Schwarzschild and Ledoux criteria respectively. The vertical dotted line is the depletion depth, i.e. the depth of the hydrogen layer. As convection approaches this line, the Schwarzschild and Ledoux boundaries begin to separate. The inset zooms into the evolution near the hydrogen boundary.	128
4.5	<i>Top:</i> evolution of the nuclear luminosity (Equation (4.4)) with time, for helium-burning and metal burning reactions (including CNO), and the total. The production of the most important CNO rates is plotted in dashed lines. <i>Bottom:</i> size of the convective and semiconvective regions as a function of time. The dotted line shows the depletion depth.	129

- 4.6 Bulk properties of the flow around the interface between the convective and stable zone prior to the collision, i.e. a moment where this boundary is below the hydrogen layer (at a column depth $y > y_d$, the vertical blue line). In each panel, the solid black line and the color dashed lines are scaled on the left-hand and right-hand sides respectively. Every quantity is horizontally averaged over the domain and each height. Overbarred quantities are time-averaged over 2 ms. *Top*: temperature profile and burning rate. *Middle*: rms velocity fluctuation and adiabatic excess. The crossing of the dashed orange with zero sets the location of the vertical orange line (Schwarzschild boundary). *Bottom*: convective heat flux and composition fluxes of ^1H and ^{12}C 135
- 4.7 Same as Figure 4.3, but for the 6 cm resolution including initial carbon (model B). Note that the scales for nuclear burning and carbon mass fractions are different than in Figure 4.3. We are also showing a larger portion of the box (8–27 m, instead of 8–22 m), to better show the growth of the convection zone. An animated version of this figure is available in the online journal. 137
- 4.8 Illustration of the temperature profile considered for the toy model. In each zone demarcated by the vertical dotted lines (except for the isothermal substrate at large depths $y > y_{\text{base}}$), the best-fitting temperature gradient $\nabla = d \ln T / d \ln y$ is obtained from the MESA model. This temperature profile is then fed into a hydrostatic solver, which determines the density at every point, while the composition is an analytical function of the pressure with Equation (4.5). See text for further details. 146
- 5.1 Velocity profile of a wind from Chapter 2 (solid line). Starting at an arbitrarily chosen temperature of 10^7 K (square markers), we enhance the opacity by 1%, 2%, and 3% (dashed, dotted, dash-dotted lines). The mass-loss rate is held constant, which is why the models are different even before the modified opacity takes effect. The crosses and dots indicate the location of the sonic point and photosphere in each model. The model with the most enhanced opacity has a its photosphere truncated by 110 km. 154
- 5.2 Vertical velocity in the convection zone of model A, 0.15 s after ignition. Upflows are in red colors, downflows are in blue colors. 157

Contents

Abstract	iii
Résumé	iv
Acknowledgments	v
Contribution to Original Knowledge	vi
Contribution of Authors	vii
List of Figures	viii
1 Introduction	1
1.1 Neutron Stars	2
1.2 The Physical Picture of Type I X-ray Bursts	4
1.2.1 Accretion and Nuclear Burning up to Ignition	5
1.2.2 Convective Rise	7
1.2.3 Radiation-driven Outflows	11
1.3 Key Recent Observations	14
1.4 Thesis Outline	17
2 Expanded Atmospheres and Winds in Type I X-Ray Bursts from Accreting Neutron Stars	19

2.1	Introduction	21
2.1.1	Observational Motivation	21
2.1.2	Static Envelopes and Winds	24
2.1.3	Outline of the Paper	28
2.2	Model Description and Methods	29
2.2.1	Steady-state Radiation Hydrodynamics with FLD	29
2.2.2	Winds	34
2.2.3	Static Expanded Envelopes	37
2.3	Properties of the Solutions	39
2.3.1	Solution Profiles	39
2.3.2	Optical Depth at the Photosphere	44
2.3.3	The Maximum Mass-loss Rate	46
2.3.4	Analytic Formula for the Mass-loss Rate	48
2.4	The Transition between Expanded Envelopes and Winds	50
2.4.1	Comparison between Expanded Envelopes and Winds as a Function of Base Luminosity	50
2.4.2	The Timescale to Reach a Steady state	53
2.4.3	Energetics of the Expansion	55
2.5	Observational Implications	57
2.5.1	Photospheric Radii	58
2.5.2	Spectral Shifts	60
2.5.3	Compact Envelopes and Touchdown Radius	62
2.6	Summary and Discussion	65
2.7	Appendix	69
2.7.1	Derivation of the Steady-state Hydrodynamics Equations	69
2.7.2	Parameter Spaces	72

2.7.3	Pressure Conditions at the Wind Base	74
2.7.4	Analytical Newtonian Envelopes	75
Interlude I: From steady-state to time-dependent		78
3	The Imprint of Convection on Type I X-Ray Bursts: Pauses in Photospheric Radius Expansion Lightcurves	79
3.1	Introduction	81
3.2	Evolution of the Composition Profile and Lightcurve Shape	84
3.3	MESA Simulations	87
3.3.1	Accumulation and formation of the layers	88
3.3.2	Ignition and Convective Rise	90
3.3.3	Wind and Collapse	94
3.3.4	Lightcurve	99
3.4	Impact of Changing the Treatment of Convection	101
3.5	Summary and Discussion	106
Interlude II: From 1D to 2D		113
4	Hydrodynamical Simulations of Proton Ingestion Flashes in Type I X-ray Bursts	114
4.1	Introduction	116
4.2	Methodology	119
4.2.1	Numerical Method	119
4.2.2	Initial Model	120
4.3	Results	123
4.3.1	Resolution Dependence and Convergence	124
4.3.2	Evolution of Convection	126
4.3.3	Convective Boundary Mixing	133

4.3.4	Burst with Initial Carbon	136
4.4	Summary and Discussion	139
4.5	Appendix: Building the initial model	144
5	Discussion and Conclusion	148
5.1	Summary	148
5.2	Future Work	151
5.2.1	Outflows	151
5.2.2	Stellar Evolution Calculations	154
5.2.3	Multidimensional Convection	155
5.2.4	Observational Prospects	158
5.3	Final Thoughts	161
References		162

“Tonight I ask you to look both ways.

For the road to a knowledge of the stars leads through the atom;
and important knowledge of the atom has been reached through the stars.”

— Sir Arthur Eddington, *Stars and Atoms*, Lecture 1, 1927

Chapter 1

Introduction

In contrast to the buzzing frenzy of life on earth, the night sky appears remarkably silent and uneventful. The laws of physics have conspired to give the stars lifetimes of billions of years. Throughout this time, these stars shine a constant light, they move around the sky in predictable patterns, and nothing else happens. This has been the observation of humankind for as long as we have stared at the sky. And yet, it is false!

A major accomplishment of astronomy over the last century has been the uncovering of the cosmos at wavelengths invisible to the eye. Doing so has revealed that many different types of *transients* animate the sky on short timescales. One notable example is type I X-ray bursts. These very bright, 10–100 seconds-long flashes of high-energy radiation are regularly observed from over 100 sources in our galaxy.

In this thesis, we model various aspects of these bursts in order to understand the extreme objects from which they originate: neutron stars. And this is where we now ought to begin.

1.1 Neutron Stars

Unlike stars similar to our Sun, which spend their main-sequence lifetime primarily burning hydrogen to helium, massive stars go through further sequences of nuclear reactions and make progressively heavier elements in their cores. Most stars with masses $\gtrsim 10 M_{\odot}$ will end up forming an iron core (Woosley et al. 2002). Because further reactions to make even heavier elements are endothermic, the core can no longer support the weight of the star above, and a core-collapse supernova ensues. In this collapse, iron nuclei are photodisintegrated into smaller constituents, allowing for the very energetic electrons to capture onto protons, creating neutrons and releasing neutrinos which rapidly escape the star. If the neutron degeneracy pressure and nuclear forces of the collapsed core — the proto-neutron star — are still not sufficient to support the overlying matter, a black hole is formed; otherwise, a neutron star remains (Woosley & Weaver 1986; Heger et al. 2003). This mechanism is well supported by observations of supernova (SN) 1987a, with the detection of neutrinos hours before it appeared in the optical (Bionta et al. 1987; Hirata et al. 1987), and more recently by infrared evidence for the presence of a neutron star in the center of its remnant (Page et al. 2020; Fransson et al. 2024).

For physicists, neutron stars are laboratories of the extreme. With masses and radii on the order of $1 M_{\odot}$ and 10 km, their average density is $\sim 10^{14} \text{ g cm}^{-3}$, comparable to the density of an atomic nucleus (and exceeding it in the inner regions of the star). Due in part to conservation of angular momentum and magnetic flux from their progenitor star, neutron stars also harbor the highest rotation rates (up to $\sim \text{k}\text{Hz}$ angular frequencies) and magnetic fields (up to $\sim 10^{15} \text{ G}$) of any object in

the universe (see Lattimer & Prakash 2004 for a review of neutron star properties). With their high compactness (mass over radius, M/R), neutron stars can be used to test and apply general relativity (Oppenheimer & Volkoff 1939; Yakovlev 2016).

An interesting quantity which connects the micro- and macroscale physics of neutron stars is their mass to radius relationship. While efforts to determine the equation of state (EoS) of the dense nuclear medium from the theoretical perspective are ongoing (Baldo & Burgio 2012), observational constraints on M and R can be used to distinguish between different models (Özel & Freire 2016). The EoS determines how stiff or deformable the star is, and what its maximum mass is. These questions are especially relevant today as they have implications for understanding binary neutron star (and neutron star plus black hole) mergers. These events are being observed increasingly frequently in gravitational waves (Abbott et al. 2023), with so far one confirmed associated electromagnetic counterpart (Drout et al. 2017). But measuring these quantities is a difficult task, and, especially in the case of R , requires a good understanding of the neutron star surface (Lattimer 2012).

There is one type of system in particular in which the neutron star surface — specifically, its *atmosphere* — can become very bright: low mass X-ray binaries (LMXBs). In these, a neutron star and $\lesssim 1 M_\odot$ companion orbit each other with periods of minutes to days (Lewin et al. 1993). In such compact configurations, Roche-lobe overflow of the companion is easily achieved, and mass-transfer occurs via an accretion disk around the neutron star (Paczynski 1971; Savonije 1978; Podsiadlowski 2014). As this gas of mostly hydrogen and helium accumulates onto the star, it burns by nuclear fusion, increasing the temperature until the ignition of a thermonuclear runaway, which we observe as a *type I X-ray burst*.

These “bursts” provide a great opportunity to study the neutron star directly, as it briefly outshines the accretion disk by at least an order of magnitude. On the observational side, they are quite frequent, with over 7100 burst events detected from 115 sources (according to the MINBAR catalogue, [Galloway et al. 2020](#), see also <https://burst.sci.monash.edu>). On the theory side, they arise from controlled situations, in the sense that the LMXBs are long-lived and stable systems, and bursts occur during periods of steady accretion. Finally, it is important to point out some of the many connections to other areas of astrophysics. First, it is well known that LMXBs are the progenitors to milisecond pulsars ([Bhattacharya & van den Heuvel 1991](#)), and bursts may inform us about their rotation and magnetic fields. Second, as will be discussed at length in this thesis, Type I X-ray bursts synthesize heavy elements, some of which may be expelled from the star and contribute over time to nucleosynthesis ([Parikh et al. 2013](#)). Lastly, they are the most common example of a thin shell flashes, which also occur in the late stages of stellar evolution of most stars ([Iben & Renzini 1983](#)) and in accreting white dwarfs ([Chomiuk et al. 2021](#)).

1.2 The Physical Picture of Type I X-ray Bursts

Type I X-ray bursts result from the combination of many physical ingredients: accretion, nuclear reactions, heat transfer by convection and radiation, and fluid dynamics. Moreover, the objects on which they take place add complexity in the form of large magnetic fields, high rotation rates, and a strongly curved spacetime. No single burst model has incorporated all of these elements. Instead, historically and in this thesis, the approach has been to combine a few of these at a time for the stages of bursts

where they are relevant, and slowly build up a comprehensive picture for how these bursts function. In this section, we go through the chronology of a typical burst and give an overview of the physics at play. We discuss previous works in the literature and the advances made in this thesis. Figure 1.4 at the end of the section presents of a visual overview.

1.2.1 Accretion and Nuclear Burning up to Ignition

The rate \dot{M}_{acc} at which the neutron star accretes¹ can be estimated from observations. Bursting sources typically have persistent count rates of $\approx 10\text{--}100 \text{ s}^{-1}$ on detectors with $\approx 100 \text{ cm}^2$ effective area, and at photon energies of $\approx 1\text{--}10 \text{ keV}$ (see e.g. [Galloway et al. 2008a](#)). Most LMXBs are found toward the center of the galaxy, at distances of \approx few to 20 kpc. This flux comes from the conversion of gravitational to thermal energy, i.e. the accretion luminosity is $L_{\text{acc}} \sim GM\dot{M}_{\text{acc}}/R$. We thus find typical luminosities in the range of $\sim 10^{34}$ to $\sim 10^{38} \text{ erg s}^{-1}$, and accretion rates in the range of $\sim 10^{-12}$ to $\sim 10^{-8} \text{ M}_\odot \text{ yr}^{-1}$ ².

Most of this thermal energy will be released into the upper, optically thin, regions of the neutron star atmosphere, and will not contribute to heating the deeper layers. As the accumulating gas gets buried to higher densities, it will convert to iron-group elements (the minimal energy configuration until electron-capture densities, $\rho \gtrsim 10^7 \text{ g cm}^{-3}$). Complete burning of hydrogen to helium releases $\sim 7 \text{ MeV}$ per

¹Note that we reserve the \dot{M} variable without a subscript for mass-loss (Section 1.2.3).

²The true maximum should be close to the Eddington rate $\dot{M}_{\text{Edd}} = 4\pi R m_p c / \sigma_T \approx 1.5 \times 10^{-8} \text{ M}_\odot \text{ yr}^{-1} \approx 10^{18} \text{ g s}^{-1}$, assuming a radius of 10 km and a pure hydrogen composition.

nucleon. This is more than enough to raise the temperature of the atmosphere to $\gtrsim 10^8$ K. It was first noticed by Hansen & van Horn (1975, months before the first detection of Type I X-ray bursts) that this will lead to unstable nuclear burning. What exactly will burn unstably (hydrogen, helium, some combination of both, or even carbon) will depend on the initial temperature profile of the atmosphere, the accretion rate, and the composition of the accreted material. Investigations of these different ignition regimes were performed early on by Joss (1977), Lamb & Lamb (1978), Taam & Picklum (1978, 1979), and Fujimoto et al. (1981) (see also Section 1.1.4 of Galloway & Keek 2021, for a summary).

Let us now narrow in on the regime relevant to this thesis: deep ignition of helium in a hydrogen-deficient layer. This occurs in sources accreting from a solar-like companion, at rates $0.01\dot{M}_{\text{Edd}} \lesssim \dot{M}_{\text{acc}} \lesssim 0.1\dot{M}_{\text{Edd}}$, where the temperature is high enough for hydrogen to burn stably via the hot CNO cycle (Bildsten 1998), but low enough for helium burning to become unstable (Keek & Heger 2015). Cumming & Bildsten (2000) computed models of this type of ignition by integrating the steady-state entropy and heat flux equations of the accumulating fuel. They found that hydrogen will deplete at a column depth³ $y_d \lesssim 10^8 \text{ g cm}^{-2}$ (after ~ 10 hours to a few days of accretion), but ignition will only happen once a column $\sim 10^8 - 10^9 \text{ g cm}^{-2}$ has been built up (see Figure 1 of Cumming & Bildsten 2000). Therefore, the mass of helium at ignition will be much greater than that of hydrogen. This has led many

³Column depth, defined by $dy = -\rho dr$ where r is the radial coordinate and ρ is the mass density, measures the amount of mass per surface area above a certain location. The depletion depth y_d is used in Chapters 3 & 4. Note also that in hydrostatic equilibrium, $dp/dr = -\rho g$ implies $p = gy$, where p is the pressure.

authors to categorize these bursts as pure helium. In this thesis, we demonstrate that the remaining hydrogen plays a critical role in both the evolution of the burst and its observational outcomes.

In Chapter 3, we present time-dependent calculations of this type of ignition, from the accretion through the end of the burst. Our simulations include a complete nuclear reaction network with hydrogen (CNO) and helium burning up to magnesium. To do this, we use the open source *Modules for Experiments in Stellar Astrophysics* (MESA) code ([Paxton et al. 2011, 2013, 2015, 2018, 2019](#)) which self-consistently solves the equations of stellar structure: conservation of mass, hydrostatic balance, energy balance, and diffusion of heat and chemical species.

1.2.2 Convective Rise

For the thermonuclear energy to lead to an X-ray *burst*, with observationally constrained rise times of $\lesssim 1$ s, the heat needs to rapidly traverse the upper layers of the atmosphere. Consider the burst discussed in the previous section which ignites at $y \sim 10^8$ g cm $^{-2}$, where the density ρ is $\sim 10^5$ g cm $^{-3}$. Numerical models (e.g. [Cumming & Bildsten 2000](#)) show that unstable helium burning will increase the temperature to $T \gtrsim 10^9$ K. For heat transported via near isotropic radiation in an optically thick medium, the entropy equation yields

$$c_p \frac{\partial T}{\partial t} = -\frac{1}{\rho} \frac{\partial F_{\text{rad}}}{\partial r} \quad (1.1)$$

$$\begin{aligned} &= \frac{1}{\rho} \frac{\partial}{\partial r} \left(\frac{c}{3\kappa\rho} \frac{\partial(aT^4)}{\partial r} \right) \\ &\approx -\frac{acT^4}{3\kappa y^2}. \end{aligned} \quad (1.2)$$

The opacity is dominated by electron scattering at high temperatures ($\kappa \approx 0.2 \text{ cm}^2 \text{ g}^{-1}$ for pure helium). A lower estimate for the heat capacity⁴ is that of an ideal gas, $c_p = 5k_B/2\mu m_p$ with $\mu = 4/3$ for ionized helium. Therefore, the local cooling timescale is

$$\tau_{\text{rad}} \approx c_p T \left(\frac{acT^4}{3\kappa y^2} \right)^{-1} \approx 4 \text{ s} \left(\frac{y}{10^8 \text{ g cm}^{-2}} \right)^2 \left(\frac{T}{10^9 \text{ K}} \right)^{-3}. \quad (1.3)$$

We see that radiation is not sufficient; convection must be what is carrying the heat to the surface.

What is the nature of this convection? We know that the rising fluid must carry a flux which is at least the radiative flux, $F_{\text{rad}} \approx acT^4/3\kappa y \sim 10^{24} \text{ erg cm}^{-2} \text{ s}^{-1}$. Through simple arguments, one can show that a few percent of the convective heat flux F_{conv} is in the form of a kinetic energy flux $F_{\text{kin}} = \rho v_{\text{conv}}^3$ (Meakin & Arnett 2007). This gives a convective velocity v_{conv} of $\sim \text{km s}^{-1}$. The size of the convective region is on the order of the pressure scale height, $p/\rho g = y/\rho \sim 10 \text{ m}$, and so the convective turnover time is on the order of milliseconds. As it rises from the bottom of the convection zone to the top, a convective parcel does not have any time to leak energy via radiation. In other words, convection is very efficient (as it tends to be in most scenarios of stellar convection, Kippenhahn et al. 2012). Note that numerical simulations give similar numbers to the ones derived here (e.g. Lin et al. 2006, Zingale et al. 2015, our work in Chapters 3 & 4.)

While radiation is inefficient deep into the layer, this does not hold true all the

⁴At high T , radiation pressure is important and increases the heat capacity. For example if half of the pressure comes from radiation, c_p is increased by a factor ≈ 15 (Clayton 1983). This only makes the cooling timescale longer. Note that we are ignoring the effects of degeneracy pressure, since degeneracy is lifted at the high temperatures of the runaway.

way to the surface. At some point, diffusive heat transport will be faster than convection, which sets the maximal extent of the convection zone (Hanawa & Sugimoto 1982), or equivalently the minimum column $y_{c,\min}$. Joss (1977) first showed that convection could not reach the photosphere. This is important because it means that the spectrum of bursts should be determined by the opacity of the light elements from the accreted material (hydrogen and helium), and not heavier metals from the ashes of nuclear burning. And yet, there sometimes is evidence for such metals in the spectrum, as we will discuss in Section 1.3. Determining $y_{c,\min}$ is therefore observationally relevant, and requires detailed numerical modeling.

Various calculations have found that convection in helium-triggered bursts would reach $\lesssim 1\%$ of the ignition depth (Joss 1978; Hanawa & Sugimoto 1982; Weinberg et al. 2006). Weinberg et al. (2006) noted that the presence of hydrogen would impede the growth of the convection zone, due to the compositional gradient between the convection zone, full of heavy elements, and the unburnt hydrogen above. It is simply more difficult for a convective element to be buoyant when its surroundings have less mass per particle (lower mean molecular weight μ) (Ledoux 1947). This highlights the fact the distribution of chemical species in the convection zone and above it plays an important role in its evolution, particularly when hydrogen is present.

In Chapter 3, we show that the exact value of $y_{c,\min}$ is sensitive to the treatment of convection. In 1D, convection is handled in a physically-motivated but approximate manner, with the mixing-length theory (MLT) of convection (e.g. Cox & Giuli 1968). One uncertainty is the location of the convective boundaries, which is usually determined by either the Schwarzschild or the Ledoux criterion. The first accounts for thermal stability only, while the second also considers the composition gradient. In

typical stellar scenarios, the two tend to agree over evolutionary timescales (because of entrainment of material across the convective boundary, [Anders et al. 2022](#)), but not necessarily over shorter ones (e.g. [Kaiser et al. 2020](#)). Our type I X-ray burst is another such example.

Following the rate of growth of the convection zone over time and the nuclear reactions taking place, we find that there is a particular moment where the convective prescriptions begin to diverge. All goes as expected while the convection zone is still in the pure helium layer, above the depletion depth. As soon as it hits the location $y = y_d$ however, ionized hydrogen (free protons) starts to get entrained below. This is new fuel, and proton-captures rapidly overtake the energy generation from helium burning. How far the protons travel and where their energy is deposited depends on the details of the convective treatment. We call this moment the “collision” (of the convection zone with the hydrogen shell). It is interesting to note that similar “proton-ingestion” events also occur in the outer shells of post main-sequence stars ([Herwig et al. 2011](#)).

What is clear is that in this situation where rapid burning interacts with convection on similar timescales, MLT is not appropriate. We must instead model the convection with multidimensional hydrodynamics. This is what motivated the third and final project of this thesis, presented in Chapter 4. Using the open source hydrodynamics code **MAESTROeX** ([Fan et al. 2019](#)), we simulate the convection at the onset of this burst in 2D. Previous hydrodynamical simulations have modeled pure helium bursts ([Lin et al. 2006](#); [Malone et al. 2011](#); [Zingale et al. 2015](#)), and homogeneously-mixed hydrogen and helium bursts ([Malone et al. 2014](#)). This is the first time a “layered” configuration (helium at the bottom, hydrogen at the top) is studied. These

simulations help us understand how the convection zone grows, what the mixing is like above the convective boundary, and how this affects the collision.

`MAESTROeX` is a low Mach number code, meaning it is appropriate for flows where the Mach number \mathcal{M} (the ratio of the velocity to the sound speed) is small, which is the case in bursting atmospheres ($\mathcal{M} \sim 10^{-4} (v_{\text{conv}}/\text{km s}^{-1})(T/10^9 \text{ K})^{-1/2}$). The fluid equations are simplified such that acoustic perturbations (sound waves) are filtered out (Almgren et al. 2006a,b). The compression of the gas due to density stratification and local cooling are still taken into account however. This is an application of the pseudo-incompressible equation, introduced by Durran (1989). The benefit of this method is that the timestep is no longer limited by the sound speed, and is thus increased by a factor $1/\mathcal{M}$. However, the overall error on the approximation is $\mathcal{O}(\mathcal{M}^2)$. We will discuss the implications of this for when \mathcal{M} reaches \sim tens of percent in the later stages of the simulations, where convective velocities exceed 100 km s^{-1} .

1.2.3 Radiation-driven Outflows

During bursts, the strong gravity of neutron stars can be overcome by strong enough radiation pressure. The Eddington luminosity is

$$L_{\text{Edd}} = \frac{4\pi GMc}{\kappa_0} = 3.5 \times 10^{38} \text{ erg s}^{-1} (1 + X)^{-1} \left(\frac{M}{1.4 M_{\odot}} \right), \quad (1.4)$$

where $\kappa_0 = 0.2(1 + X) \text{ cm}^2 \text{ g}^{-1}$ is the classical electron scattering opacity and X is the mass fraction of hydrogen. Complete burning of helium to iron-group releases $E_{\text{He}} \approx 1.6 \text{ MeV/nucleon}$. Burning the whole layer ($y = 10^8 \text{ g cm}^{-2}$) produces

$4\pi R^2 y E_{\text{He}} \approx 10^{39}$ erg, which is the total fluence that must come out during the burst. This energy is produced on timescales of $\lesssim 1$ s, and escapes the surface in a few seconds (Equation (1.3)). Therefore, the most powerful bursts (high ignition depth) will produce a luminosity exceeding L_{Edd} . What necessarily follows is a radiatively-driven expansion of the atmosphere — a super-Eddington wind — which causes the star’s photosphere to move out to large radii. This is observed as a sudden decrease in the effective blackbody temperature of the spectrum (Lewin et al. 1993). These events are called photospheric radius expansion (PRE) bursts, and they account for about a fifth of all type I X-ray bursts (Galloway et al. 2020).

In the outflow, the “excess” luminosity $L - L_{\text{Edd}}$ is reprocessed to raise the enthalpy of the expanding gas, to give it kinetic energy, and to extract it from the gravitational potential (Kato 1983). Therefore, what we observe during a PRE is just L_{Edd} itself, including the $(1 + X)$ dependence. This idea is central to Chapter 3, in which we show that the hydrogen profile $X(y)$ leftover by convection directly maps to the lightcurve.

The gravitational binding energy of the accreted material is $GM/R \approx 160$ MeV/nucleon for $M = 1.4 M_{\odot}$ and $R = 12$ km (the actual neutron star parameters used throughout this thesis). This is ~ 100 times larger than the energy from nuclear burning, which means we can only expect about 1% of the material to be ejected, a column $y_{\text{ej}} \sim 10^6$ g cm $^{-2}$. Still, this is often larger than $y_{\text{c,min}}$, which means that some of the convectively mixed nuclear ashes can be ejected (Weinberg et al. 2006). Note that it takes ≈ 10 s to eject this mass at a mass-loss rate \dot{M} equal to the Eddington rate, which is consistent with the observed duration of PRE bursts.

While metals should be fully ionized in the deep layers of the atmosphere, they will begin to recombine in the outflow, producing spectral features such as lines and photoionization edges (Bildsten et al. 2003). We will see examples of lines in the next section. These will be redshifted by a factor $(1 - 2GM/r_0c^2)^{-1/2}$, where r_0 is the location where the photon is absorbed/emitted. Also, the wind velocity should cause a blueshift $\approx (1 - v/c)$. In a typical wind model (Paczynski & Proszynski 1986), the photosphere extends to > 100 km and the terminal velocity is $\sim 0.01c$, such that both factors are limited to the percent level. In principle, one could use these lines to place constraints on the neutron star mass, and its radius if the line is produced close to the surface. But detailed outflow models are needed to determine the size of these factors, and how they combine depending on location.

Another way to measure the radius is by tracking the photosphere in the tail of the burst, as the wind begins to die down. The photospheric radius r_{ph} at the moment where the blackbody temperature hits a maximum is referred to as the touchdown radius r_{td} (Damen et al. 1990). It is often assumed that $r_{\text{td}} = R$, the neutron star radius. In this way, the radii of six neutron stars have been inferred (Özel & Freire 2016). In combination with other measurements, this has led to strongly disfavoring some EoS (Özel et al. 2016). However, because the radiative flux remains large at touchdown, the photosphere may still be extended. Even below L_{Edd} , i.e. when there is not a wind, Paczynski & Anderson (1986) showed that hydrostatic structures exist with photospheres tens of kilometers above the neutron star radius. As they explained, such extended solutions are only possible in general relativity.

This observational paradigm of PREs motivates the creation of models of the radiation dominated neutron star envelope. In the first project of this thesis, Chap-

ter 2, we present the first set of self-consistent static expanded envelopes and super-Eddington wind models in general relativity. They are self-consistent in the sense that they are solved using the exact same set of equations, under the same assumptions. One important ingredient when it comes to the location of the photosphere is the radiation transfer. We use the theory of flux-limited diffusion of Levermore & Pomraning (1981) to model the transition from the optically thick to thin regimes. This improves over previous models of Paczynski & Anderson (1986), Paczynski & Proszynski (1986), and Guichandut (2020) (my Master’s thesis), which only considered the optically thick regime. We analyze these models in the context of recent observations, and find that spectral shifts are small, and touchdown radii are large.

1.3 Key Recent Observations

Since their discovery in the 1970’s by the *Astronomical Netherlands Satellite* (Grindlay et al. 1976), Type I X-ray bursts have been observed by multiple generations of X-ray instruments. The largest number of them were observed by the *Rossi X-ray Timing Explorer* (RXTE). These telescopes were not well adapted to observe PRE bursts however, because their lower spectral cutoff was too high (2 keV in the case of RXTE, Jahoda et al. 1996). In PREs, as the photosphere moves out, the peak of the blackbody moves to <1 keV. The successor to RXTE, the *Neutron Star Interior Composition Explorer* (NICER), was launched in 2017. NICER does have a soft X-ray response, down to 0.2 keV (Gendreau et al. 2012), allowing it to track the full evolution of PRE bursts (Keek et al. 2018, and see Figure 1.1). Two observations from NICER provide important motivation for our work.

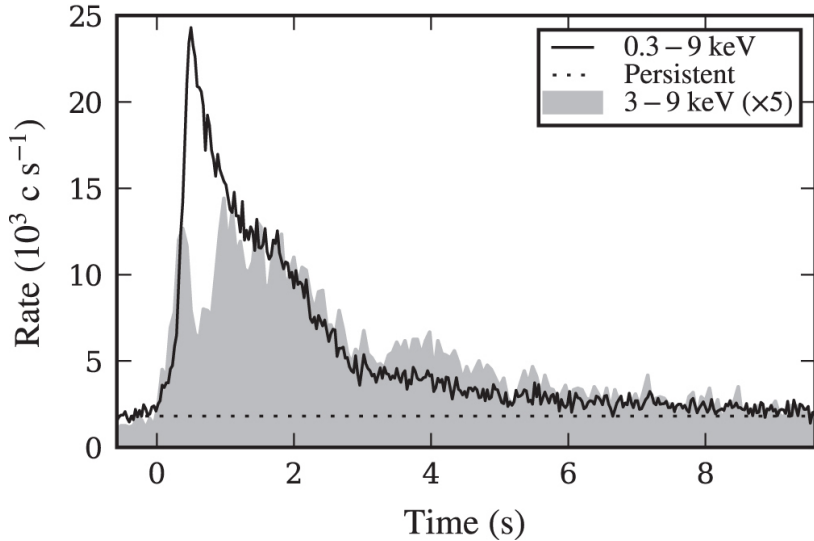


Figure 1.1: Light curve of a PRE burst from 4U 1820–30 and how it depends on the instrumental spectral range. The solid line shows the count rate seen by NICER, while the gray shaded area shows the count rate (scaled up by a factor of 5) for instruments with no soft X-ray response. The dotted line shows the count rate for the persistent emission prior to the burst. Adapted from Figure 1 of Keek et al. (2018).

One of the first systems targeted was 4U 1820–30, an ultracompact binary with an orbital period of 11 minutes, known for its recurrent helium-triggered bursts which often reach the Eddington limit (Kuulkers et al. 2003; Cumming 2003; in ’t Zand et al. 2012). Five bursts were detected from this source in 2017 (Keek et al. 2018), four of which had a PRE phase (one is shown in Figure 1.1). Two had expansions of $r_{\text{ph}} \approx 75$ km, while the other two had $r_{\text{ph}} \approx 100$ km. By combining the spectra of bursts in the same pair, Strohmayer et al. (2019) found good evidence for one emission and two absorption lines. Moreover, the locations of these lines were at a constant offset from one pair to the other. This is illustrated in Figure 1.2. These results show that weaker PREs (smaller r_{ph}) produce spectral lines that are redshifted compared to stronger ones. This is expected from the gravitational redshift alone, which is smaller for larger photospheric radii. However, Strohmayer et al. (2019) could not explain

the 4.6% offset with realistic neutron star masses, and suggested the possibility of a blueshift contribution from the wind velocity as well.

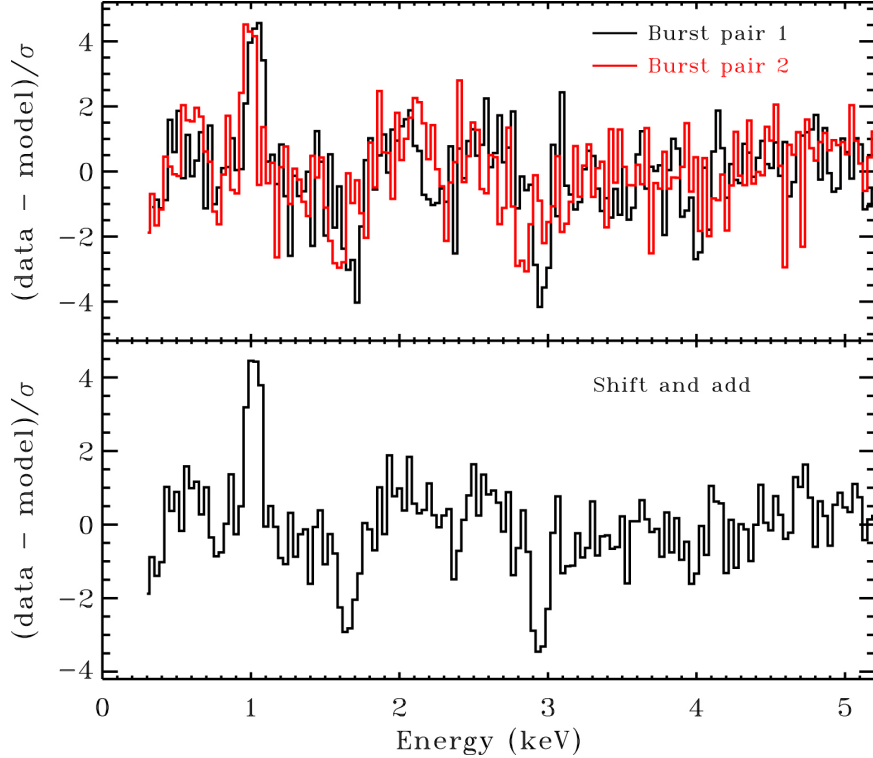


Figure 1.2: Fit residuals of the absorbed blackbody model for the stronger (pair 1) and weaker (pair 2) PRE bursts from 4U 1820–30. In the bottom panel, the residuals are added after the pair 2 residuals have been shifted by the best fitting line ratio of 1.046. An emission line is seen at 1 keV, and absorption lines are seen at 1.7 and 3 keV. From Figure 8 of Strohmayer et al. (2019).

Another well-known LMXB is SAX J1808.4–3658, which contains an accreting millisecond pulsar and a hydrogen-rich companion in a 2 hour orbit (Wijnands & Van Der Klis 1998; Galloway & Cumming 2006), was observed in 2019 by NICER. Two type I X-ray bursts were seen, the second being a PRE (Bult et al. 2019). The high time-resolution data showed an interesting feature in the lightcurve. In the initial rise of the burst, the flux stalled for ≈ 0.7 s, then continued on, at a lower rate, toward the burst peak. The authors labeled this feature as a “pause”. Moreover, the ratio

of the bolometric luminosity between the peak and the pause was ≈ 1.68 , which is close to the ratio of L_{Edd} for pure helium ($X = 0$) and solar-like ($X \approx 0.7$) gas (Equation (1.4)). The implication is that the pause represents the rapid ejection of a hydrogen-rich shell at its Eddington luminosity. Once the shell has become optically thin, the helium layer appears and is ejected at the higher value of L_{Edd} .

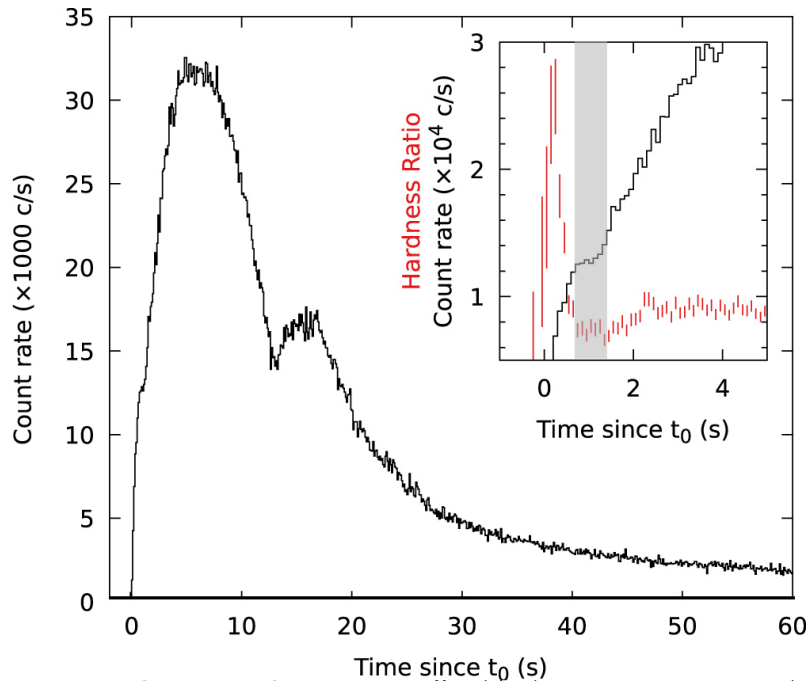


Figure 1.3: PRE burst from SAX J1808.4–3658. The gray band in the inset shows the location of the pause. Adapted from Figure 1 of [Bult et al. \(2019\)](#)

1.4 Thesis Outline

This thesis explores one by one the burst stages introduced in Section 1.2, though in a different order. Figure 1.4 below serves as a visual overview of the work we will present. We begin in Chapter 2 with steady-state models of the radiatively-driven outflows during the PRE phase, including general relativity and flux-limited

diffusion. There, we simply treat the burning layer as a hot and luminous inner boundary condition. In Chapter 3, we follow the time-dependent transition from accretion of the fuel, to ignition and the convective rise, to the outflow. This outflow is now Newtonian and optically thick, but has a composition which evolves over time, changing the observed L_{Edd} . In Chapter 4, we are specifically focused on fluid simulations of convection in the deep layers of the atmosphere, starting after the ignition and ending before the flux makes its way to the surface. Finally, we conclude in Chapter 5, summarizing our results and discussing avenues for future work and observations.

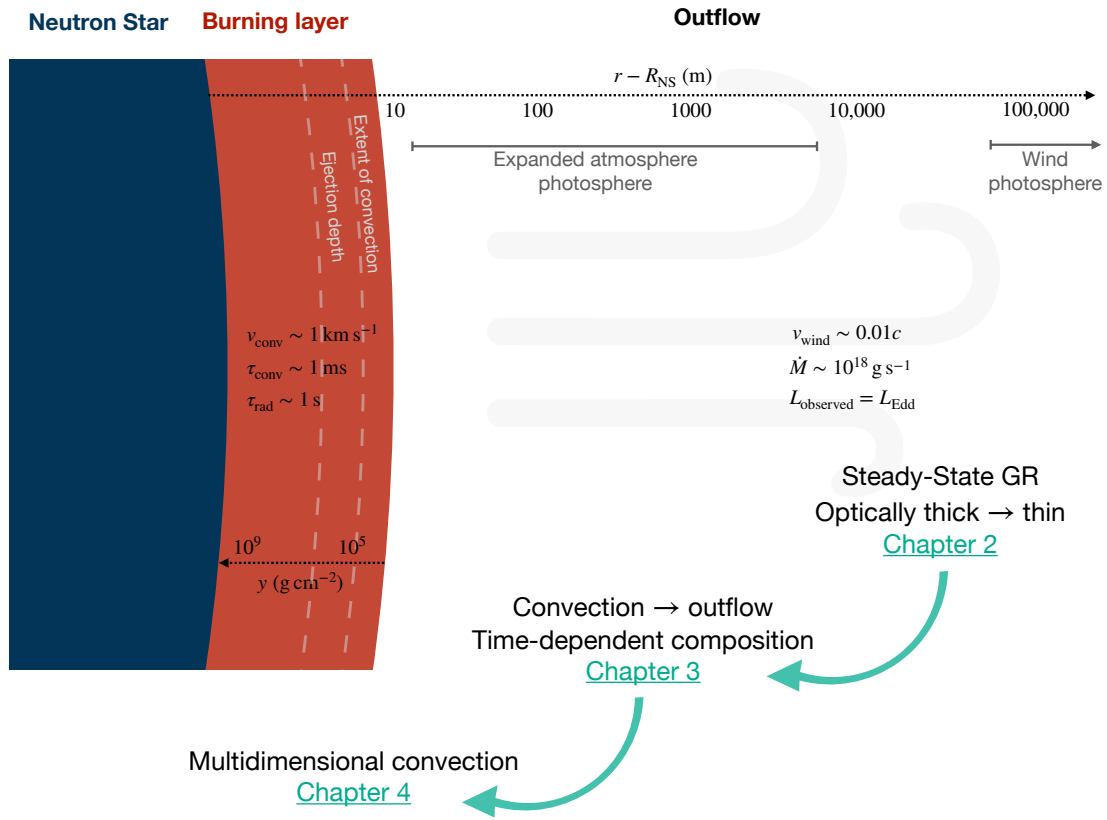


Figure 1.4: Schematic of a PRE burst with relevant scales in the different regions, notable locations, and the aspects that are treated in each chapter.

Chapter 2

Expanded Atmospheres and Winds in Type I X-Ray Bursts from Accreting Neutron Stars

*This thesis chapter originally appeared in the literature as
Guichandut, Cumming, Falanga, Li and Zamfir 2021, *The Astrophysical Journal (ApJ)*, 914, 49. <https://doi.org/10.3847/1538-4357/abfa13>*

Authors

Simon Guichandut¹, Andrew Cumming¹, Maurizio Falanga², Zhaosheng Li³, Michael Zamfir¹

¹Department of Physics and McGill Space Institute, McGill University, 3600 rue University, Montreal, QC, H3A 2T8, Canada

²International Space Science Institute (ISSI), Hallerstrasse 6, 3012 Bern, Switzerland

³Key Laboratory of Stars and Interstellar Medium, Xiangtan University, Xiangtan 411105, Hunan, P.R. China

Abstract

We calculate steady-state models of radiation-driven super-Eddington winds and static expanded envelopes of neutron stars caused by high luminosities in type I X-ray bursts. We use flux-limited diffusion to model the transition from optically thick to optically thin, and include effects of general relativity, allowing us to study the photospheric radius close to the star as the hydrostatic atmosphere evolves into a wind. We find that the photospheric radius evolves monotonically from static envelopes ($r_{\text{ph}} \lesssim 50\text{--}70$ km) to winds ($r_{\text{ph}} \approx 100\text{--}1000$ km). Photospheric radii of less than 100 km, as observed in most photospheric radius expansion bursts, can be explained by static envelopes, but only in a narrow range of luminosity. In most bursts, we would expect the luminosity to increase further, leading to a wind with photospheric radius $\gtrsim 100$ km. In the contraction phase, the expanded envelope solutions show that the photosphere is still ≈ 1 km above the surface when the effective temperature is only 3% away from its maximum value. This is a possible systematic uncertainty when interpreting the measured Eddington fluxes from bursts at touchdown. We also discuss the applicability of steady-state models to describe the dynamics of bursts. In particular, we show that the sub to super-Eddington transition during the burst rise is rapid enough that static models are not appropriate. Finally, we analyze the strength of spectral shifts in our models. Expected shifts at the photosphere are dominated by gravitational redshift, and are therefore predicted to be less than a few percent.

2.1 Introduction

Type I X-ray bursts are transient astronomical events that result from thermonuclear runaways on the surface of accreting neutron stars (see [Galloway & Keek 2021](#) for a comprehensive review). By making the neutron star shine brightly in X-rays for many seconds to minutes, these bursts provide a unique opportunity to study the properties of the star directly. A subset of bursts produce high enough fluxes that hydrostatic equilibrium on the surface is lifted, leading to an expansion of the star’s photosphere ([Lewin et al. 1993](#)). In these photospheric radius expansion (PRE) bursts, the observed blackbody temperature quickly drops from its initial state of $\sim 2\text{--}3$ keV to $\lesssim 0.5\text{--}1$ keV, then slowly rises back to its initial state during the burst decay, as the photosphere falls back down to the surface. The inferred blackbody or photospheric radius correspondingly rises and falls back down again. Traditionally, observations of PRE bursts show an artificial dip in flux as the peak energy of the emission moves out of the spectral band of the detector, although recently the Neutron Star Interior Composition Explorer (NICER), a modern X-ray telescope with a soft X-ray response, has been able to track the complete spectral evolution of PRE bursts ([Keek et al. 2018](#)). In this paper, we revisit models of the neutron star envelope as it expands and evolves into a wind.

2.1.1 Observational Motivation

A number of recent observations motivate our work. The first is the large sample of PRE bursts now available, including extreme events with very dramatic radius expansion, as well as long-lasting super-Eddington phases. Of the more than 7000

bursts from 85 sources in the MINBAR (*Multi-Instrument Burst Archive*) catalog (Galloway et al. 2020), about one fifth exhibit PRE. Most show moderate expansion in which the photosphere expands to tens of kilometres above the stellar surface, but in rare *superexpansion* bursts, the photosphere reaches a thousand kilometres in radius or more (in ’t Zand & Weinberg 2010). Superexpansion bursts occur in ultracompact binaries in which the neutron star accretes helium at low rates, giving rise to long duration bursts with Eddington phases lasting for minutes (in ’t Zand et al. 2005). An extreme example is the 4U 1820-30 superburst, which was at the Eddington limit for approximately 20 minutes (Strohmayer & Brown 2002; in ’t Zand & Weinberg 2010). in ’t Zand & Weinberg (2010) noted that whereas the overall duration of the Eddington phase scales with the burst fluence, so that more energetic bursts have longer Eddington phases, the duration of the superexpansion phase is always short, approximately a few seconds. The reason for this is not clear, but could be the result of ejection of a shell of material during the onset of a wind (in ’t Zand & Weinberg 2010), or the timescale for the wind to be polluted with heavy nuclear burning ashes (Yu & Weinberg 2018).

The second motivation is to address systematic effects in using PRE bursts to determine neutron star radii, and thereby constrain the dense matter equation of state (see Özel & Freire 2016 for a review). The expansion of the photosphere at the Eddington luminosity provides a means to place joint constraints on both mass and radius of the star (Lewin et al. 1993; Özel et al. 2016). The principal way of doing this is by interpreting the peak of the blackbody temperature curve, after the expansion phase, as the *touchdown* point, i.e. the moment where the atmosphere collapses back down to the surface and the photospheric radius is equal to the neutron star radius.

However, the systematics of the photosphere’s evolution and touchdown point are not well understood, as discussed for example by [Galloway et al. \(2008b\)](#) and [Steiner et al. \(2010\)](#). [Steiner et al. \(2010\)](#) found that allowing the photospheric radius to be larger than the neutron star radius at touchdown gave a much larger number of physical solutions for the mass and radius. [Özel et al. \(2016\)](#) however argued against this interpretation and showed that including rotational corrections and the temperature-dependence of the opacity alleviates this issue (see [Suleimanov et al. 2020](#) for further discussion). Nonetheless, the extent to which the photosphere remains elevated at the touchdown point is still an open question.

Third, recent observational evidence of spectral edges and lines in type I X-ray burst spectra ([in ’t Zand & Weinberg 2010](#); [Kajava et al. 2017](#); [Li et al. 2018](#); [Strohmayer et al. 2019](#)) suggests that heavy elements are present near the photosphere during the expansion phase. This is of interest since type I X-ray bursts are sites of heavy element production by the rp-process (e.g. [Schatz et al. 2003](#)), and measuring the gravitational redshift of spectral features would provide an important constraint on the stellar mass and emission radius, and therefore the neutron star mass-radius relation. [Weinberg et al. \(2006\)](#) and [Yu & Weinberg \(2018\)](#) show that convection at the onset of the burst brings nuclear burning ashes to low enough column depths that they could be ejected by a wind. Both absorption/emission lines and photoionization edges are expected to be present in the burst spectra, though their observational signature will be subject to complicated effects such as rotational broadening in the case of lines ([Chang et al. 2005](#)) and the exact composition of the outflow in the case of edges ([Weinberg et al. 2006](#)).

[Strohmayer et al. \(2019\)](#) presented observations of bursts from 4U 1820-30 with

NICER that showed emission and absorption lines. They found three lines that were blueshifted by the same factor of ≈ 1.046 in a set of bursts with photospheric radii of ≈ 100 km compared to weaker bursts with photospheric radii of ≈ 75 km. This is consistent with line emission associated with heavy elements in the wind in the sense that the lines in the weaker bursts should be produced closer to the star, and thus have stronger gravitational redshift, and in addition have smaller wind velocities and therefore weaker Doppler blueshifts. [Strohmayer et al. \(2019\)](#) suggested that both of these effects could work together to create the observed shifts, although they noted that the observed shifts are perhaps larger than expected from wind models. The gravitational redshift difference corresponding to a change in emission radius from 75 to 100 km is only $\approx 1\%$, with a $\lesssim 1\%$ addition effect from Doppler shift due to the wind velocity.

2.1.2 Static Envelopes and Winds

There are two types of solution for the neutron star envelope in which the photosphere moves to large radius, depending on whether the luminosity at the base of the envelope as seen at infinity, L_b^∞ , is larger or smaller than the Eddington luminosity,

$$\begin{aligned} L_{\text{Edd}} &\equiv \frac{4\pi GMc}{\kappa_0} \\ &= 3.5 \times 10^{38} \text{ erg s}^{-1} \left(\frac{M}{1.4M_\odot} \right) \left(\frac{1}{1+X} \right), \end{aligned} \tag{2.1}$$

where $\kappa_0 = 0.2(1+X) \text{ cm}^2 \text{ g}^{-1}$ is the constant electron scattering opacity, and X is the hydrogen fraction ([Clayton 1983](#)). When $L_b^\infty > L_{\text{Edd}}$, the luminosity in excess of Eddington is used to drive mass loss, and a super-Eddington wind forms with

radiative luminosity $\approx L_{\text{Edd}}$, and a mass-loss rate

$$\dot{M} \approx \frac{L_b^\infty - L_{\text{Edd}}}{GM/R} \sim 10^{18} \text{ g s}^{-1} \left(\frac{L_b^\infty - L_{\text{Edd}}}{L_{\text{Edd}}} \right) \quad (2.2)$$

(Paczynski & Proszynski 1986). At luminosities below, but close to, the Eddington luminosity ($0.7 \lesssim L_b^\infty/L_{\text{Edd}} \lesssim 1$), Paczynski & Anderson (1986) showed that in general relativity there is a sequence of expanded hydrostatic envelopes which can extend outward as much as ~ 200 km.

Both of these solutions depend crucially on the fact that at the high temperatures $\gtrsim 10^9$ K reached in bursts, Klein-Nishina corrections reduce the electron scattering opacity. This leads to a significant increase in the local Eddington luminosity or *critical luminosity*

$$L_{\text{cr}} = \frac{4\pi GMc}{\kappa(\rho, T)} \left(1 - \frac{2GM}{rc^2} \right)^{-1/2}. \quad (2.3)$$

This means that even when the luminosity is super-Eddington, it can be well below the critical luminosity at the base of the envelope, allowing the hydrostatic envelope to carry the super-Eddington flux (Hanawa & Sugimoto 1982). At larger radii, the temperature and L_{cr} drop, so that L approaches and can eventually exceed L_{cr} , leading to outward expansion. This leads to a compact geometrically-thin inner envelope in hydrostatic equilibrium that transitions into an extended outer region. In the case of static envelopes, the structure adjusts such that the luminosity at each radius is slightly below the local critical luminosity (to one part in 10^4 ; Paczynski & Anderson 1986), maintaining hydrostatic balance but with a very extended structure. In the case of winds, the luminosity is similarly close to the critical luminosity until the fluid reaches the sound speed, at which point the luminosity becomes super-critical (typically by $\sim 1\%$, e.g. Paczynski & Proszynski 1986), furthering the acceleration of

the material to velocities $\sim 0.01c$.

The burst wind regime has been studied extensively, with different approximations. The first studies calculated steady-state wind solutions assuming Newtonian gravity and optically-thick radiative transfer (Ebisuzaki et al. 1983; Kato 1983). Quinn & Paczynski (1985) improved the treatment of the outer boundary with an approximate form for the transition from optically-thick to optically-thin parts of the wind. More recently, Herrera et al. (2020) carried out a more detailed survey of the available parameter space for these kinds of models, with an emphasis on predicting correlations between photospheric quantities. These studies established the basic features of super-Eddington winds from type I X-ray bursts, namely the radiative luminosity is within a few percent of the Eddington luminosity, the outflow velocity is $\sim 0.01c$, and photospheric radii range from tens of km to $\gtrsim 1000$ km for the highest mass-loss rates. These conclusions carried over into the works of Joss & Melia (1987), Titarchuk (1994) and Shaposhnikov & Titarchuk (2002), that included a more detailed discussion of the radiative transfer in the wind, and Yu & Weinberg (2018) who calculated the first time-dependent models.

In contrast to Newtonian models, Paczynski & Proszynski (1986) showed that in wind models that include general relativity, the photospheric radius is always more than an order of magnitude larger than the neutron star radius, even at low mass-loss rates. This is very different from Newtonian models, in which the photospheric radius reduces smoothly to the neutron star radius at low mass-loss rates. This behavior is consistent with the expanded hydrostatic envelopes that Paczynski & Anderson (1986) found when general relativity was included. The results of Nobili et al. (1994), which included general relativity as well as a more sophisticated treatment of radiative

transfer, show a similar result that the photospheric radius is $\gtrsim 100$ km at low mass-loss rates.

These results suggest that it is crucial to include general relativity if we are interested in photospheric radii $\lesssim 100$ km, as observed in the majority of PRE bursts, or if we are interested in understanding how the photospheric radius behaves as the burst luminosity drops below Eddington and touches down. For example, based on their results, [Paczynski & Proszynski \(1986\)](#) concluded that a super-Eddington wind should have a photospheric temperature too low to be detected by available X-ray instruments, implying that observed PRE bursts had hydrostatic expanded atmospheres rather than winds.

In this paper, we study the evolution of the envelope around the transition from hydrostatic to wind, when the photospheric radii are expected to be close to the star. We include general relativity and use flux-limited diffusion to model the transition from optically thick to optically thin regions, allowing us to extend both static atmosphere and wind solutions out to low optical depths and thereby use a consistent definition of the photosphere in both. This improves on the calculations of [Paczynski & Anderson \(1986\)](#) and [Paczynski & Proszynski \(1986\)](#), which assumed optically thick radiation transport and had different prescriptions for the photosphere. For static envelopes, [Paczynski & Anderson \(1986\)](#) set $\tau = \int \rho \kappa dr = 2/3$ at the location where $T = T_{\text{eff}} \equiv (L/4\pi r^2 \sigma)^{1/4}$, whereas for winds [Paczynski & Proszynski \(1986\)](#) instead set the optical depth parameter $\tau^* = \rho \kappa r = 3$.

We focus here on light element envelopes. We show results for pure helium envelopes, but also check that pure hydrogen or solar composition models are not

substantially different. It is important to point out that heavy elements may play an important role in the radiative transfer in the wind, and may explain the smaller observed photospheric radii compared to light element winds. [in 't Zand & Weinberg \(2010\)](#) point out the possible importance of line driving from hydrogenic ions of Ni or other heavy elements. [Yu & Weinberg \(2018\)](#) performed the first time-dependent calculations of optically-thick Newtonian winds, with a focus on tracking the composition of different elements over time and space, and proposed that heavy element pollution terminates the superexpansion phase ([in 't Zand & Weinberg 2010](#)). While there can be no doubt that heavy elements must be integrated into models of PRE bursts to take advantage of the observations now available, we start in this paper with a self-consistent set of steady-state, light element models that we can use as a basis for future work.

2.1.3 Outline of the Paper

We start in Section 2.2 by describing the general equations for steady-state flow in general relativity, and how we apply flux-limited diffusion to model the radiative transfer. We then describe the methods we use to calculate wind and static envelope solutions, including the change of variables proposed by [Joss & Melia \(1987\)](#) to integrate near the critical point of the wind. In Section 2.3, we present the solution profiles, and discuss the location of the photosphere as the base luminosity varies and the maximum and minimum mass-loss rates. In Section 2.4, we discuss the transition between expanded envelopes and winds as the base luminosity rises during a burst, and the applicability of steady-state solutions. In Section 2.5, we discuss some

observational implications of our results, including the expected photospheric radii, spectral shifts, and the behavior of the photosphere near touchdown. We conclude in Section 2.6.

2.2 Model Description and Methods

In this section, we explain how we obtained our wind and envelope solutions. In Section 2.2.1, we derive the equations for the steady-state flow of an ideal gas, considering general relativity (GR) under a Schwarzschild metric, and radiation transport described by flux-limited diffusion (FLD). In Section 2.2.2, we explain our numerical method for obtaining wind solutions that satisfy boundary conditions at the stellar surface and at large radii, and similarly in Section 2.2.3 for envelopes.

2.2.1 Steady-state Radiation Hydrodynamics with FLD

For both the wind and static envelope case, we consider a fluid and radiation field in a spherically symmetric Schwarzschild spacetime, which is characterized by the curvature parameter $\zeta = (1 - 2GM/c^2r)^{1/2}$, where G is the gravitational constant, c is the speed of light, M is the mass of the neutron star and r is the radial coordinate.

The parameter

$$\Psi \equiv \sqrt{\frac{1 - 2GM/c^2r}{1 - v^2/c^2}} = \zeta\gamma, \quad (2.4)$$

where v is the velocity and γ is the usual Lorentz factor, is often referred to as the *energy parameter* for the flow, written as “ Y ” in Paczynski & Proszynski (1986) and Thorne et al. (1981), or “ y ” in Park (2006).

In steady-state, the relativistic radiation hydrodynamics equations can be manipulated to yield conservation equations for mass and energy,

$$\dot{M} = 4\pi r^2 \rho v \Psi, \quad (2.5)$$

$$\dot{E} = L \Psi^2 \left(1 + \frac{v^2}{c^2} \right) + \dot{M} \Psi \left(c^2 + \frac{P + U}{\rho} \right), \quad (2.6)$$

and a momentum equation for the fluid and radiation ,

$$(\rho c^2 + P_g + U_g) \frac{d \ln \Psi}{dr} + \frac{d P_g}{dr} - \frac{1}{c \Psi} \rho \kappa F = 0, \quad (2.7)$$

where \dot{M} and \dot{E} are the mass and energy-loss rates, ρ is the rest-mass density, F is the local (or comoving) radiative flux and $L = 4\pi r^2 F$ is the local luminosity. The total pressure $P = P_g + P_R$ and energy $U = U_g + U_R$ are the sum of the gas and radiation contributions. In Appendix 2.7.1, we show how to obtain these equations from the time-dependent hydrodynamics equations.

For the electron scattering opacity, we use the fitting formula¹ from [Paczynski \(1983\)](#),

$$\kappa = \kappa_0 \left[1 + \left(\frac{T}{4.5 \times 10^8 \text{ K}} \right)^{0.86} \right]^{-1}, \quad (2.8)$$

where $\kappa_0 = 0.2(1 + X)$ is the classical scattering opacity from the Thomson cross-section ([Clayton 1983](#)). When the local temperature of the gas T , becomes large, the cross-section is reduced by Klein-Nishina corrections. [Paczynski \(1983\)](#) also provides a density correction to κ_0 from electron degeneracy, which we can safely ignore at the densities in our solutions. We have also verified a posteriori that free-free opacity

¹[Poutanen \(2017\)](#) presents a more accurate version of this formula, but also shows that Equation (2.8) is accurate to a few percent (see Figure 2 of [Poutanen 2017](#)) which is adequate for our purposes.

was not important anywhere in our models. Even near the base where the densities are large ($\rho \sim 10^4$ g cm $^{-3}$), the temperatures are large enough ($T \sim 10^9$ K) that electron-scattering dominates (Schatz et al. 1999).

We assume an ideal monatomic gas equation of state, with pressure and internal energy

$$P_g = \frac{kT\rho}{\mu m_p} \quad ; \quad U_g = \frac{3}{2}P_g, \quad (2.9)$$

where k is the Boltzmann constant, m_p is the proton mass and μ is the mean molecular weight. Note that we treat μ as a constant of the model, meaning the composition of the gas is fixed. We write the radiation energy density as $U_R = aT^4$ where a is the radiation constant, and we will define the radiation pressure P_R later in this section. We use the usual ratio $\beta = P_g/P$ to track the relative importance of these pressures throughout the flow. As discussed by Quinn & Paczynski (1985) and Joss & Melia (1987), at moderate to high optical depths, LTE applies and the gas and radiation can be described with a single temperature T (even though the opacity is scattering dominated, Compton scattering is able to keep the photons and gas at the same temperature; Joss & Melia 1987). In regions of low optical depth, T measures the radiation energy density via $T^4 = U_R/a$. We still use Equations (2.8) and (2.9) in these regions since the gas pressure is negligible ($\beta \ll 1$) and $\kappa \approx \kappa_0$, independent of temperature.

We model the transition between optically thick and optically thin regions using FLD as described by Levermore & Pomraning (1981), but with added factors of Ψ to account for general relativity and produce the correct limits (see Rahman et al. 2019

for a similar approach to neutrino transport in GR). The radiative flux is given by

$$F = \frac{-\lambda c \nabla (\Psi^4 U_R)}{\kappa \rho \Psi^3}, \quad (2.10)$$

where the interpolating factor λ is

$$\lambda = \frac{2 + \mathcal{R}}{6 + 3\mathcal{R} + \mathcal{R}^2} \quad ; \quad \mathcal{R} = \frac{1}{\kappa \rho \Psi^3} \frac{|\nabla(\Psi^4 U_R)|}{U_R}. \quad (2.11)$$

In the optically thick regions, a short mean free path results in $\mathcal{R} \rightarrow 0$, $\lambda \rightarrow 1/3$, and Equation (2.10) becomes the standard photon diffusion equation, with additional factors of Ψ because of GR (see Flammang 1984; Paczynski & Proszynski 1986). In the optically thin regions, \mathcal{R} becomes large such that $\lambda \rightarrow 1/\mathcal{R}$ and $F \rightarrow cU_R$, the correct photon streaming limit. Note that this limit gives an analytical expression for the radiation temperature in the optically thin limit,

$$T_{\lambda \rightarrow 0} = \left(\frac{L}{4\pi r^2 ac} \right)^{1/4}, \quad (2.12)$$

which is useful since the luminosity is nearly constant there. In the transition between the two regions, it is not possible to exactly describe the radiation without explicitly solving the full radiative transfer equations, but the smooth and monotonic transition controlled by λ should be satisfactory. At any point, if the flux and temperature are known, λ can be calculated by solving

$$6\lambda^2 + \lambda(3x - 2) + x(x - 1) = 0 \quad ; \quad x \equiv \frac{F}{cU_R}. \quad (2.13)$$

FLD can also be used to interpolate the radiation pressure tensor with the flux limiter λ (Levermore 1984). In 1D, this gives a simple relation for the radiation pressure in the radial direction,

$$P_R = (\lambda + \lambda^2 \mathcal{R}^2) U_R. \quad (2.14)$$

This has limits of $P_R = U_R/3$ in optically thick regions, where the radiation is isotropic, and $P_R = U_R$ in optically thin regions, where the radiation is beamed in the radial direction².

By combining the fluid equations (Equation (2.5)–(2.7)) with the radiative flux limited diffusion prescription (Equation (2.10)) and the equation of state (Equation (2.9)), the equations of structure can be derived in the form of three coupled first order ordinary differential equations for the velocity, density and temperature of the gas. These are

$$\frac{d \ln v}{d \ln r} (c_s^2 - v^2 A) \gamma^2 = \frac{GM}{r \zeta^2} \left(1 + \frac{1}{2} \frac{c_s^2}{c^2} \right) - 2c_s^2 - C, \quad (2.15)$$

$$\frac{d \ln \rho}{d \ln r} (c_s^2 - v^2 A) = \left(2v^2 - \frac{GM}{r \Psi^2} \right) A + C, \quad (2.16)$$

$$\frac{d \ln T}{d \ln r} = -T^* - \frac{GM}{c^2 \zeta^2 r} - \frac{\gamma^2 v^2}{c^2} \frac{d \ln v}{d \ln r}, \quad (2.17)$$

with the sound speed defined by $c_s^2 \equiv P_g/\rho$, and the parameters

$$\begin{aligned} T^* &= \frac{\kappa \rho r F}{4acT^4 \lambda \Psi} = \frac{1}{\lambda \Psi} \frac{L}{L_{\text{Edd}}} \frac{\kappa}{\kappa_0} \frac{GM}{4r} \frac{\rho}{U_R}, \\ A &= 1 + \frac{3}{2} \frac{c_s^2}{c^2}, \\ C &= \frac{1}{\Psi} \frac{L}{L_{\text{Edd}}} \frac{\kappa}{\kappa_0} \frac{GM}{r} \left(1 + \frac{\beta}{12\lambda(1-\beta)} \right). \end{aligned} \quad (2.18)$$

Equations (2.15)–(2.18) allow us to extend the calculations of [Paczynski & Proszynski \(1986\)](#) to optically thin regions. In the optically thick limit ($\lambda = 1/3$), they reduce to the exact equations written in this previous paper.

²Previous work such as [Quinn & Paczynski \(1985\)](#) took the radiation pressure as the optically thick expression even in optically thin regions, and explained that this only resulted in errors of order v/c . We made models with both prescriptions for P_R , and while it is true that they give similar qualitative results, the accumulation of errors displaces the photosphere by up to 5%.

2.2.2 Winds

For winds, we look for solutions to equations (2.15) and (2.17) that have a small velocity near the surface of the neutron star and that continuously accelerate to large radii. These solutions have an important location called the *sonic point*, where the fluid goes from being subsonic to supersonic. This is due to the sound speed c_s decreasing with temperature. This point always appears as a singularity in the velocity gradient equation, no matter the equation of state ([Lamers & Cassinelli 1999](#)).

In our Equation (2.15) (also Equation (2.16)), the singularity occurs when $v = v_s \equiv c_s/\sqrt{A}$. Note that this is not exactly the sound speed due to small GR corrections of order $(c_s/c)^2$ (see [Paczynski & Proszynski 1986](#)). In order for the solutions to smoothly pass through the sonic point, the right-hand side of Equation (2.15) also needs to vanish, which defines the sonic point radius r_s , and its temperature T_s .

To avoid numerical difficulties around r_s , we adapt the approach of [Joss & Melia \(1987\)](#) (who solved the Newtonian equations), and introduce a new dimensionless variable

$$\Phi = A^{1/2} \mathcal{M} + A^{-1/2} \mathcal{M}^{-1}, \quad (2.19)$$

where $\mathcal{M} = v/c_s$ is the Mach number. Φ has a value of exactly 2 at the sonic point.

The gradient is given by

$$\begin{aligned} \frac{d\Phi}{dr} = & \frac{(A\mathcal{M}^2 - 1)(3c_s^2 - 2Ac^2)}{4\mathcal{M}A^{3/2}c^2r} \frac{d\ln T}{d\ln r} \\ & - \frac{c_s^2 - Av^2}{vc_s r \sqrt{A}} \frac{d\ln v}{d\ln r}. \end{aligned} \quad (2.20)$$

When substituted into equation (2.15), the singularity at the sonic point cancels, allowing a smooth integration through r_s . As for equation (2.17), the last term may easily be ignored since $v^2 \ll c^2$.

We constructed wind solutions for every value of the mass-loss rate \dot{M} with the following method. We first set a trial value for the energy-loss rate \dot{E} , which allows us to solve for the luminosity at any point r given values for T and v using Equation (2.5)-(2.6). We then choose a trial value for the sonic point location r_s . The sonic point temperature T_s can be found by requiring that the right-hand side of Equation (2.15) be zero, using a simple root-finding algorithm. We then integrated T and Φ outward from the sonic point with Equation (2.17) and (2.20) to a maximum radius $r_{\max} = 10^9$ cm. We used these same equations to integrate inward from the sonic point to $0.95 r_s$, enough to step away from the sonic point and avoid numerical divergences. We then switched to integrating r and T with ρ as the independent variable, all the way down to the surface of the star, constructing equations for $dr/d\rho$ and $dT/d\rho$ from Equation (2.16) and Equation (2.17). We used ρ as the independent variable instead of r at this stage to avoid taking many small steps in r in the geometrically thin region near the stellar surface, whereas ρ changes by orders of magnitude in this region.

In order to have a single wind model per value of \dot{M} , two boundary conditions must be imposed, which fix the final values \dot{E} and r_s . Our inner boundary serves as a matching point between the wind and the burning layer. Since the inner part of the wind close to the surface is in near-hydrostatic equilibrium, this relates to a pressure condition via the relation $P = gy$, where $g = (GM/R^2)\zeta^{-1}(R)$ is the surface gravity of the star with radius R , and y is the integrated column depth of the wind. We define the wind base r_b as the location where a column depth $y_b = 10^8$ g cm⁻² is reached, and require that this be the radius of the star, that is

$$r_b \equiv r(P/g = y_b) = R. \quad (2.21)$$

Note that while we integrate our models to this high column depth, only a column $y_{\text{ej}} \sim 10^6\text{--}10^7 \text{ g cm}^{-2}$ can be ejected in the wind, due to the limited supply of nuclear fuel (Weinberg et al. 2006). But by going to high pressure, we simply calculate the gradual transition to a shell in hydrostatic balance. Similarly, Paczynski & Proszynski (1986) required $r = R$ to occur at constant T , and Joss & Melia (1987) required a constant ρ , both of which yield similar results. However, matching with y is more useful if these wind models are to be used to connect to simulations of the burning layer, as y is the more convenient coordinate in a hydrostatic layer. Finally, note that the exact spatial location of the matching point is not important and has no impact on the outer regions of the wind.

Our outer boundary condition is different from what has typically been used in the literature. Whereas previous studies used a thermal outer boundary condition such as $T = T_{\text{eff}}$ where $\kappa\rho r \approx 1\text{--}3$ (see Paczynski & Proszynski 1986 and Section 2.3.2), or added a free parameter v_∞ to integrate inward from a large radius (e.g. Quinn & Paczynski 1985), we simply require that the velocity be finite at infinity,

$$v(r \rightarrow \infty) > 0. \quad (2.22)$$

With our ability to integrate in the optically thin regions, we have found that the equations of structure (2.15)–(2.17) are very stiff, in that their behaviour at large radii is strongly dependent on the exact values of the initial conditions. This was studied in detail by Turolla et al. (1986), who cautioned against trying to fine-tune initial parameters to shoot out to the correct solution at radial infinity. An alternative is to match to a second solution integrated inward from infinity, as Quinn & Paczynski (1985). Instead, we integrated our solutions outward with a simple but

consistent step-wise shooting method, which we explain in Appendix 2.7.2. This always worked and naturally lead the temperature profiles to the optically thin limit (Equation (2.12)).

Our procedure for determining the values for the parameters (r_s, \dot{E}) at every model value \dot{M} is a simple root-finding method for the two boundary conditions. First, for a range of values for \dot{E} , we find the value of r_s that allows numerical integration to r_{\max} without having the velocity diverge in either direction. Then, we integrate inward from r_s to the wind base r_b , and evaluate the error on the boundary condition Equation (2.21). The final values of (r_s, \dot{E}) are then found by searching for where this error vanishes, i.e. where the inner boundary condition is satisfied. In Appendix 2.7.2, we show a visualization of the (\dot{M}, \dot{E}, r_s) parameter space and the root-finding procedure.

2.2.3 Static Expanded Envelopes

The equations of structure for relativistic static atmospheres can simply be taken from the wind equations with $v = 0$. In particular, we may integrate the equations for dT/dr and $d\rho/dr$, Equation (2.17) and (2.16). In the optically thick limit, these equations reduce to the same equations as [Paczynski & Anderson \(1986\)](#).

Because there is no mass loss, there is no net transfer of energy from the radiation to the gas, i.e. the luminosity must be conserved through the atmosphere. Therefore, each model, labeled by its photospheric radius r_{ph} , is parametrized by a unique value of L^∞ , the luminosity seen by observers at infinity (in Equation (2.6), $L^\infty = \dot{E}$). The

local luminosity L is then a function of the radial coordinate with

$$L(r) = L^\infty \left(1 - \frac{2GM}{c^2 r}\right)^{-1} = L^\infty \zeta(r)^{-2}.$$

The method to find envelope solutions is similar to the wind case. We start at some middle point where we can specify an initial condition, then integrate outward to a maximum radius, and inward to the stellar surface, and verify that boundary conditions are satisfied on both ends. We start with a trial value of L^∞ at the photosphere, $r = r_{\text{ph}}$. The photosphere is defined as the location where $T = T_{\text{eff}}$, the effective blackbody temperature of the atmosphere, as in [Paczynski & Anderson \(1986\)](#). This gives an initial condition for the temperature,

$$T_{\text{ph}} = \left(\frac{L_{\text{ph}}}{4\pi r_{\text{ph}}^2 \sigma} \right)^{1/4}, \quad (2.23)$$

where $T_{\text{ph}} = T(r_{\text{ph}})$, $L_{\text{ph}} = L(r_{\text{ph}})$, and $\sigma = ac/4$. This condition fixes the FLD parameters of Equation (2.13) to $x = 0.25$, $\lambda \approx 0.309$, meaning the photosphere is neither optically thick nor thin, but in the transition between the two.

We then search for the value of the density at the photosphere, $\rho_{\text{ph}} = \rho(r_{\text{ph}})$, that allows us to integrate outward from the photosphere to a large radius r_{max} , and reach the expected optically thin limit given by Equation (2.12) – this is our outer boundary condition. Similarly to the wind case, we found that this required high precision on the initial values, or the integration would diverge. In particular, we found that the [Paczynski & Anderson \(1986\)](#) prescription for ρ_{ph} , based on fixing the optical depth of the photosphere (the outer boundary for their optically-thick calculations), always resulted in ρ crashing to zero just after the photosphere. We will show in Section 2.3.2 that fixing the optical depth of the photosphere is not accurate for envelopes.

We finally integrate inward to the surface, where we require the same condition based on column depth as in the wind case, Equation (2.21). For each choice of r_{ph} , we search for the values of $(L^\infty, \rho_{\text{ph}})$ that lead to both outer and inner boundary conditions being satisfied. We show the $(L^\infty, r_{\text{ph}}, \rho_{\text{ph}})$ parameter space in the Appendix 2.7.2. In this way, we construct a family of envelope solutions parametrized by L^∞ .

2.3 Properties of the Solutions

We now discuss our solutions for winds and static envelopes. We calculate solutions for a neutron star of mass $1.4M_\odot$ and radius 12 km, giving a surface gravity $g = 1.60 \times 10^{14} \text{ cm s}^{-2}$ and surface redshift factor $(1 - 2GM/Rc^2)^{-1/2} = 1.24$. For the composition, we take fully ionized helium ($\mu = 4/3$). We begin by showing profiles for temperature, density, velocity and flux in Section 2.3.1, comparing the static envelope and wind solutions.

In Section 2.3.2, we discuss our treatment of the photosphere and compare it to previous papers which did not model the optically thick to thin transition. In Section 2.3.3, we discuss the maximum mass-loss rate for winds, and in Section 2.3.4, we discuss the dependence of the mass-loss rate on base luminosity.

2.3.1 Solution Profiles

Figure 2.1 shows the radial profiles of temperature, density, velocity and flux for solutions of winds and envelopes. Close to the surface, both temperature and density drop sharply with radius in a thin layer in hydrostatic equilibrium (in the wind case

the velocities are very subsonic at the stellar surface, so hydrostatic balance applies). In winds, the hydrostatic region slowly transitions to an outflowing one, where v settles to $\sim 0.01 c \sim 3 \times 10^8 \text{ cm s}^{-1}$ at large distance. Note that in the wind solutions, the profiles continue smoothly through the photosphere, whereas in envelopes the density drops exponentially above the photosphere. In all cases, at large distances the temperature goes to the correct optically thin power law, Equation (2.12). For winds, the luminosity at large distance is within 1% of L_{Edd} . The bottom right panel shows the radiative flux parametrized by x (Equation (2.13)). When $x \ll 1$, $\lambda \approx 1/3$ and the photons diffuse through the optically thick medium. The photosphere is at a fixed value of $x = 0.25$ because of Equation (2.23), and shortly after the streaming limit $x = 1$ is reached.

We show the gradient of T , v , and ρ in Figure 2.2. At the photosphere, the gradients are close to those expected for a constant velocity, in which case mass conservation (Equation (2.5)) implies $\rho \propto r^{-2}$ (actual values near the photosphere are $d \ln v / d \ln r \approx 0.5$ and $d \ln \rho / d \ln r \approx -2.5$, similar for all \dot{M}). Near the sonic point, these gradients are steeper, $d \ln v / d \ln r \approx 2$ and $d \ln \rho / d \ln r \approx -4$ for the larger \dot{M} winds; $d \ln v / d \ln r \approx 1$ and $d \ln \rho / d \ln r \approx -3$ for the lowest \dot{M} . For comparison, [Titarchuk \(1994\)](#) and [Shaposhnikov & Titarchuk \(2002\)](#) assumed that $v \propto r$ and $\rho \propto r^{-3}$ as an approximate background profile for their radiative transfer calculations. We see that in reality the power law indices vary continuously with r through the region near the photosphere.

Figure 2.3 shows the corresponding density–temperature profiles. The models are all radiation pressure dominated in the extended regions, transitioning to a gas dominated regime in the surface regions. Note that at the high temperatures at the

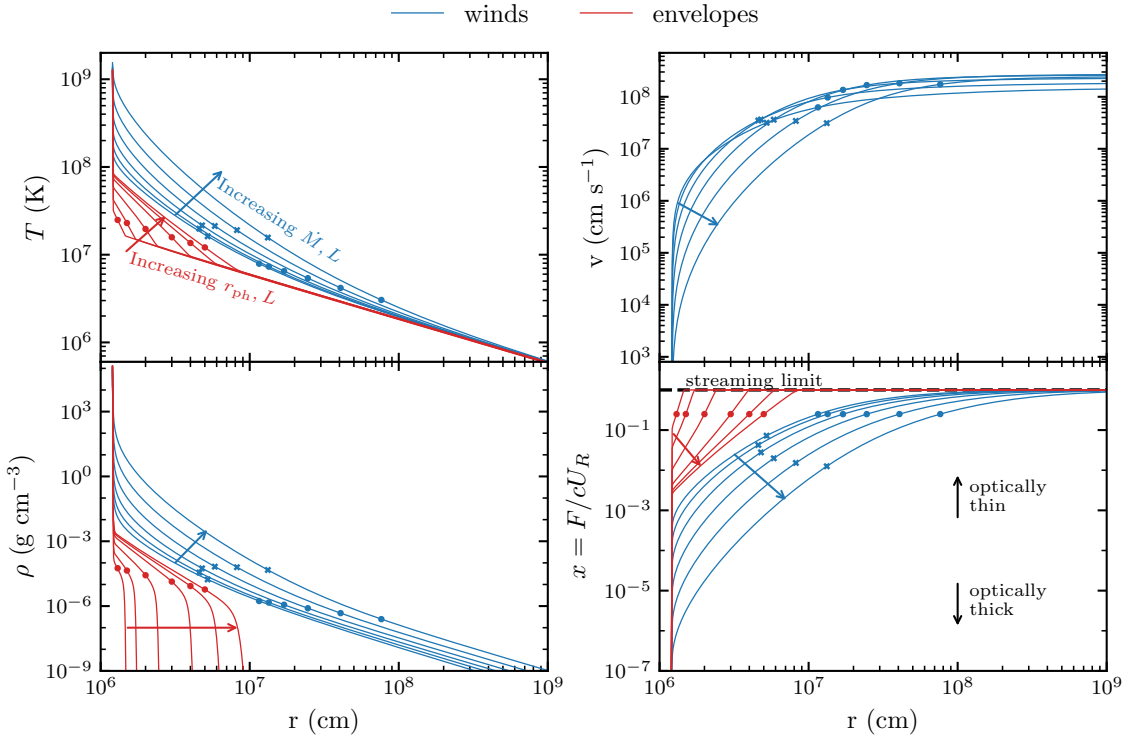


Figure 2.1: Radial profiles of the temperature (top left), velocity (top right), density (bottom left) and flux-energy ratio (bottom right), for pure helium winds (blue) and envelopes (red). Crosses and dots indicate the positions of the sonic points and photospheric radii respectively. Following the arrow direction, the winds have mass-loss rates $\log \dot{M} = (17.25, 17.5, 17.75, 18.0, 18.25, 18.5)$ and base luminosities $L_b^\infty/L_{\text{Edd}} = (1.10, 1.17, 1.30, 1.51, 1.89, 2.55)$. The envelopes have photospheric radii $r_{\text{ph}} = (13, 15, 20, 30, 40, 50)$ km, and luminosities $L^\infty/L_{\text{Edd}} = (0.89, 0.92, 0.95, 0.98, 0.99, 1.00)$. The black arrows in the bottom right panel point toward the optically thick and thin limits.

base of these envelopes, electron degeneracy is lifted so that our approximation of ideal gas applies even near the base.

The sonic points for the winds range from ≈ 40 km to more than 100 km (indicated by crosses in Figure 2.1). It is interesting to note that the sonic points of these super-Eddington winds are much closer to the star than in a thermally-driven wind. The standard isothermal wind has $r_s = GM/2c_s^2 \sim 10^6$ km ($T/10^7$ K) $^{-1}$ (e.g. Parker

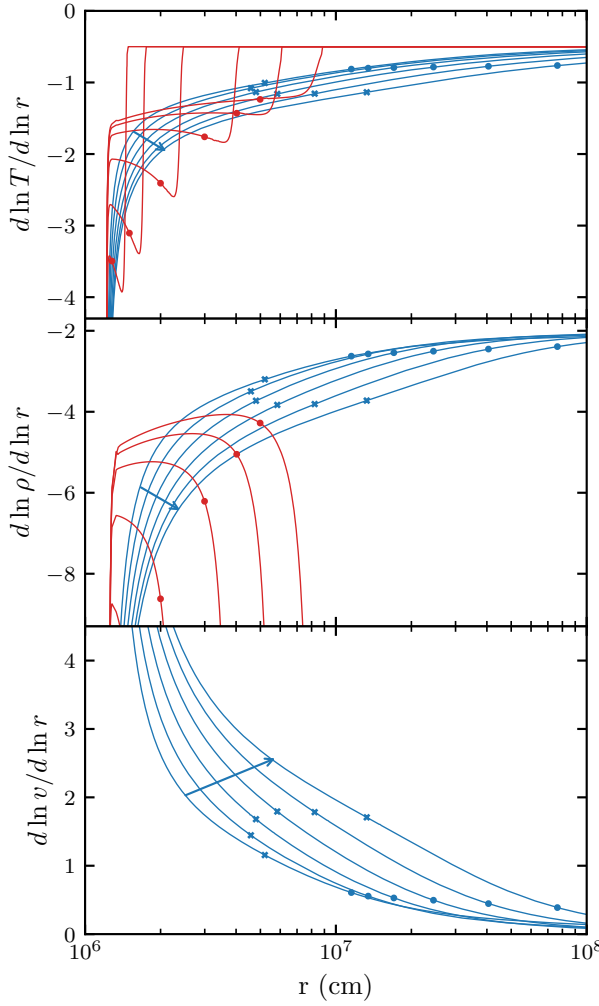


Figure 2.2: Gradients of the temperature, density and velocity for the same wind and envelope models as in Figure 2.1. Crosses and dots mark the locations of r_s and r_{ph} respectively. Blue arrows show the direction of increasing \dot{M} for winds.

1963). In our case, setting the right-hand-side of Equation (2.15) (the numerator of dv/dr) equal to zero, and assuming that $\lambda \approx 1/3$ and $c_s^2 \ll c^2$ at $r = r_s$, gives

$$r_s \approx \frac{GM}{2c_s^2} \zeta^{-2} \left[1 - \left(\frac{4-3\beta}{4-4\beta} \right) \frac{L}{L_{\text{cr}}} \right]. \quad (2.24)$$

With a sonic point temperature of $\approx 2 \times 10^7$ K and density $\approx 10^{-4}$ g cm $^{-3}$, $\beta \sim 10^{-4}$. Similarly, the luminosity lies slightly below the critical luminosity at the sonic point by a similar amount, $1 - L/L_{\text{cr}} \sim 10^{-4}$, as we show in Figure 2.4. The overall effect is to reduce the sonic point radius to $\sim 10^{-4}GM/2c_s^2 \sim 100$ km.

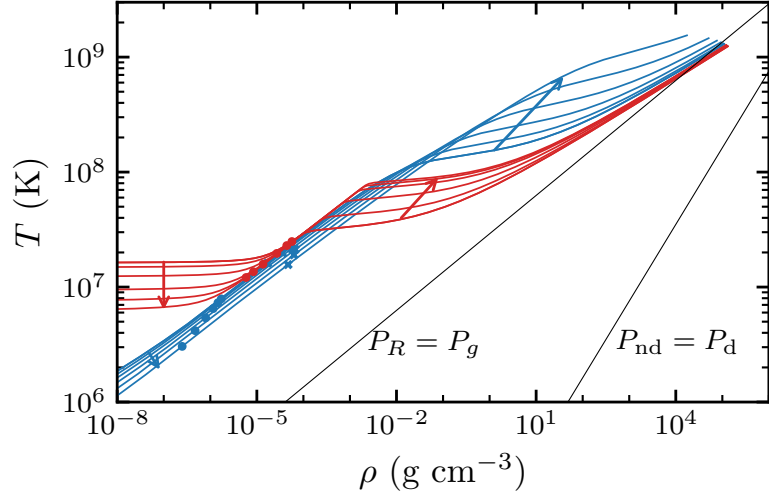


Figure 2.3: Density-temperature profiles of the same wind and envelope models as in Figure 2.1. Crosses and dots mark the locations of r_s and r_{ph} . Blue and red arrows show the direction of increasing \dot{M} and r_{ph} for winds and envelopes respectively. The black lines indicate the points of transition from one pressure regime to another. $P_{\text{nd}} \propto T\rho$ and $P_{\text{d}} \propto \rho^{5/3}$ are the pressures of non-degenerate and degenerate electrons.

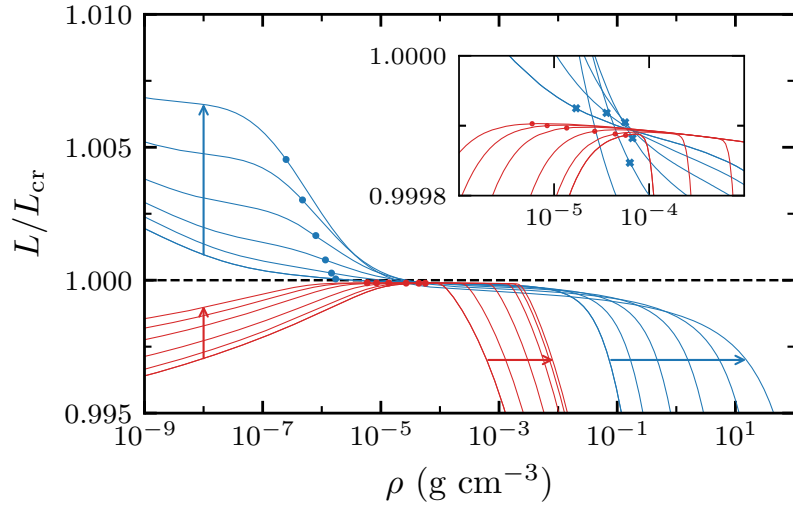


Figure 2.4: Density profiles of the luminosity in the same wind and envelope models as in Figure 2.1. Crosses and dots mark the locations of r_s and r_{ph} . Blue and red arrows show the direction of increasing \dot{M} and r_{ph} for winds and envelopes respectively. The dashed black line denotes $L = L_{\text{cr}}$. The inset zooms in to the locations of the wind sonic points and envelope photospheres.

2.3.2 Optical Depth at the Photosphere

Optically-thick calculations typically set their outer boundary by specifying the optical depth at the photosphere, where $T = T_{\text{eff}}$. For example, for their static envelope models, Paczynski & Anderson (1986) set the optical depth of the photosphere to be $\tau = 2/3$ (corresponding to the plane-parallel grey atmosphere). Specifying the optical depth in turn specifies the pressure through the relation $P = gy = g\tau/\kappa$. In wind calculations, typically the optical depth parameter $\tau^* = \kappa\rho r$ is specified at the photosphere, e.g. Paczynski & Proszynski (1986) set $\tau^* = 3$ when $T = T_{\text{eff}}$ and Herrera et al. (2020) set $\tau^* = 8/3$.

Figure 2.5 compares these optical depths at the photosphere (where $T = T_{\text{eff}}$) for our solutions. Since we model optically thin regions and go to arbitrarily large radii, we can calculate the true optical depth,

$$\tau(r) = \int_r^\infty \kappa(r)\rho(r) \frac{dr'}{\zeta(r')}, \quad (2.25)$$

where the curvature parameter ζ is included to give the proper length in the Schwarzschild geometry (Niedzwiecki & Zdziarski 2006). We see that for winds, τ and τ^* are approximately equal to each other. Indeed, one can show that $\tau \approx \tau^*/(n-1)$ if $\rho \sim r^{-n}$ (Quinn & Paczynski 1985), and as discussed in Section 2.3.1, ρ is a power law in r with $n \approx 2$ at $r > r_{\text{ph}}$.

Figure 2.5 shows that the optical depth at the photosphere increases from $\tau < 1$ for the most compact extended atmosphere solutions, to $\tau \approx 3$ for the winds. Whereas Paczynski & Anderson (1986) assumed that $\tau = 2/3$ at the photosphere of their static envelopes, we see that in fact τ increases as the envelopes become more extended. For the winds, $\tau(r_{\text{ph}}) \approx 2.7\text{--}3$, and $\tau^*(r_{\text{ph}}) \approx 3.7\text{--}3.9$ which compare well with the values

$\tau^* = 3$ and 5 used by Paczynski & Proszynski (1986). Yu & Weinberg (2018) also found $\tau \approx 3$ for the photosphere in their (Newtonian) hydrodynamic calculations. The result that $\tau = 3$ for the wind solutions matches the expectation for a grey spherical atmosphere with a constant opacity and density profile $\rho \propto r^{-2}$. Larson (1969) derived an expression for the temperature profile in the case where $\rho\kappa \propto r^{-n}$, finding

$$T^4 = \frac{L}{16\pi r^2 \sigma} \left[1 + 3\tau \left(\frac{n-1}{n+1} \right) \right]. \quad (2.26)$$

For $n = 2$, this gives $T^4 = (T_{\text{eff}}^4/4)(1 + \tau)$, which implies that $T = T_{\text{eff}}$ for $\tau = 3$. When $\tau \rightarrow 0$, we recover the optically thin limit Equation (2.12).

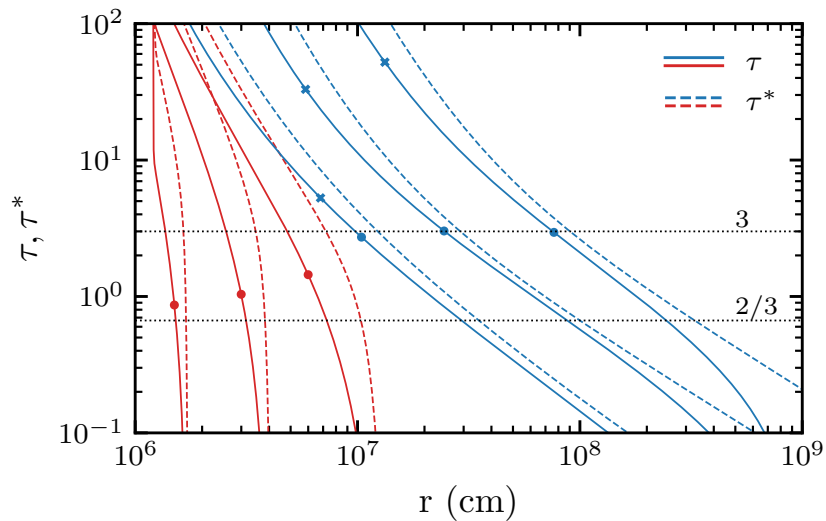


Figure 2.5: Optical depth given by $\tau^* \equiv \rho\kappa r$ and τ (Equation (2.25)) throughout the wind (blue) and envelope (red) models. The wind models shown are $\log \dot{M} = (17, 18, 18.5)$, left to right, the envelope models are $r_{\text{ph}} = (15, 30, 60)$ km. Crosses and dots mark the locations of r_s and r_{ph} . The dotted lines mark specific values of $2/3$ and 3 .

2.3.3 The Maximum Mass-loss Rate

Figure 2.3 shows that as \dot{M} increases, the transition from radiation pressure to gas pressure being dominant happens at larger and larger densities. The highest \dot{M} models are still radiation dominated ($\beta \ll 1$) at the base r_b . [Paczynski & Proszynski \(1986\)](#) pointed out that because models with high \dot{M} maintain the steeply increasing temperature to large depths, they are too hot to match onto a nuclear burning envelope, placing an upper limit on the mass-loss rate that can be achieved.

We can relate the expected mass-loss rate to the amount of nuclear energy deposited in the burst. In Appendix 2.7.3, we derive an analytic expression for the value of β expected in the burning layer after a release of nuclear energy $E_{\text{nuc}} = E_{18} 10^{18} \text{ erg g}^{-1}$. In the limit of large energy release, we find $\beta \approx 4k_B T_R / \mu m_p E_{\text{nuc}} \approx 0.06 g_{14}^{1/4} y_8^{1/4} \mu^{-1} E_{18}^{-1}$, where T_R is the radiation-pressure-limited temperature given by $gy = aT_R^4/3$. Burning helium to carbon releases $E_{\text{nuc}} \approx 0.6 \text{ MeV per nucleon}$, and complete burning of helium to iron group elements gives $E_{\text{nuc}} \approx 1.6 \text{ MeV per nucleon}$. So we expect the amount of energy that can be released rapidly at the start of a burst to be $E_{18} \sim 1$, meaning that the value of β achieved in the initial stages of a burst is limited to be $\gtrsim 0.1$, with a corresponding limit on the mass-loss rate.

Figure 2.6 shows the mass-loss rate \dot{M} as a function of the energy deposited E_{nuc} . We calculate this curve using our wind models to relate β and \dot{M} , and using the result in Appendix 2.7.3 to relate β to E_{nuc} . We see that a nuclear energy release of order 1 MeV per nucleon limits the mass-loss rate in the resulting wind to be $\lesssim 2 \times 10^{18} \text{ g s}^{-1}$. A similar sharp increase in the enthalpy per particle with mass-loss rate can be seen in Table 2 of [Kato \(1983\)](#). In what follows, we show results only for

wind models going up to $\dot{M} = 10^{18.5} \text{ g s}^{-1}$, corresponding to $L_b^\infty \approx 2.5 L_{\text{Edd}}$. Note that [Paczynski & Proszynski \(1986\)](#) rejected models with $\dot{M} > 10^{19} \text{ g s}^{-1}$ for similar reasons (their larger \dot{M} range was because they matched to a higher temperature at the base). [Herrera et al. \(2020\)](#) found no solutions with $\dot{M} \gtrsim 10^{19.5} \text{ g s}^{-1}$, even with a more flexible inner boundary condition.

Figure 2.6 also shows that the mass-loss rate drops off dramatically for $E_{\text{nuc}} \lesssim 0.4 \text{ MeV}$ per nucleon. This is roughly consistent with the estimate from [Fujimoto et al. \(1987\)](#) that in order for a burst to show radius expansion, the helium fraction in the fuel layer at ignition should be $\gtrsim 0.5$. The implication is that pure helium flashes should be able to readily provide enough nuclear energy to drive a wind. Expanded envelopes have similar values of β at the base to the low \dot{M} wind solutions ($\beta_b \approx 0.59\text{--}0.63$ for envelopes shown in Figure 2.1–2.5), and so require similar energy releases $\approx 0.4 \text{ MeV}$ per nucleon.

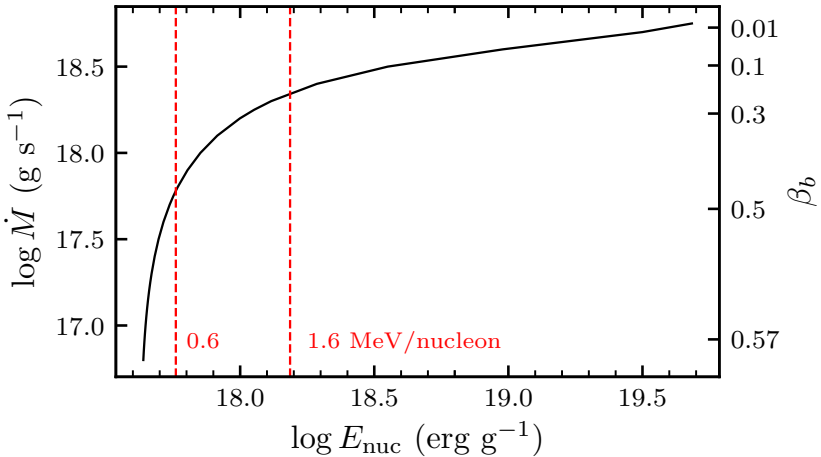


Figure 2.6: Values of the mass-loss rate \dot{M} as a function of the nuclear energy produced at the base, according to Equation (2.50). The right axis shows values of β at the wind base. The dashed red lines mark the energy released by complete burning of helium to carbon and complete burning of helium to iron group elements.

2.3.4 Analytic Formula for the Mass-loss Rate

A common prescription for mass-loss rates is the one derived by [Paczynski & Proszynski \(1986\)](#) and given in Equation (2.2). This is obtained by equating the constant \dot{E} (Equation (2.6)) at the base of the envelope with that at the photosphere, neglecting the contributions from the enthalpy and kinetic energies, which are sub-dominant. In Figure 2.7, we plot $\xi \equiv (L_b^\infty - L_{\text{Edd}})/(G M \dot{M} / R)$, the ratio of the prediction to our model values, as a function of the base luminosity. At low base fluxes and mass-loss rates, the prediction is 50% larger than the true value, and remains 10% larger even at higher mass-loss rates.

These differences are straightforward to understand. At the base of the envelope, $\dot{E} \approx L_b^\infty + \dot{M} c^2 (1 - 2GM/Rc^2)^{1/2}$. At large distance from the star, $\dot{E} \approx L_{\text{Edd}} + \dot{M}(c^2 + w)$, where w is the enthalpy per unit mass. We neglect the contribution from enthalpy at the base, assume the gravitational redshift factor is unity far away from the star, and neglect the kinetic energy $\propto v^2$ at both locations. With Equation (2.12) for T in the optical thin region, and writing $\rho = \dot{M}/4\pi r^2 v_\infty$, the enthalpy in the outer part of the wind, $w = 2aT^4/\rho$, can be written

$$\frac{\dot{M}w}{L_{\text{Edd}}} = \frac{2v_\infty}{c}, \quad (2.27)$$

independent of r . Equating the two expressions for \dot{E} and solving for the mass-loss rate gives

$$\dot{M}c^2 [1 - \zeta(R)] = L_b^\infty - L_{\text{Edd}} \left(1 + \frac{2v_\infty}{c} \right) \quad (2.28)$$

where $\zeta(R) = (1 - 2GM/Rc^2)^{1/2}$ is the curvature parameter at the base. With $c^2(1 - \zeta(R)) \approx GM/R$ and neglecting the v_∞ term, this reduces to Equation (2.2).

Without making these approximations, we find

$$\begin{aligned}\xi &= \frac{L_b^\infty - L_{\text{Edd}}}{G\dot{M}/R} \\ &= \frac{1 - \zeta(R)}{GM/Rc^2} \left[1 - \frac{2v_\infty}{c} \frac{L_{\text{Edd}}}{L_b^\infty - L_{\text{Edd}}} \right]^{-1}. \end{aligned} \quad (2.29)$$

The first term in equation (2.29) is ≈ 1.12 for our choice of M and R , and causes the overall offset of ξ from the dotted line in Figure 2.7. The second term causes ξ to increase sharply at low luminosities, where the enthalpy at large distances is significant, and consequently Equation (2.2) overpredicts the true mass-loss rate.

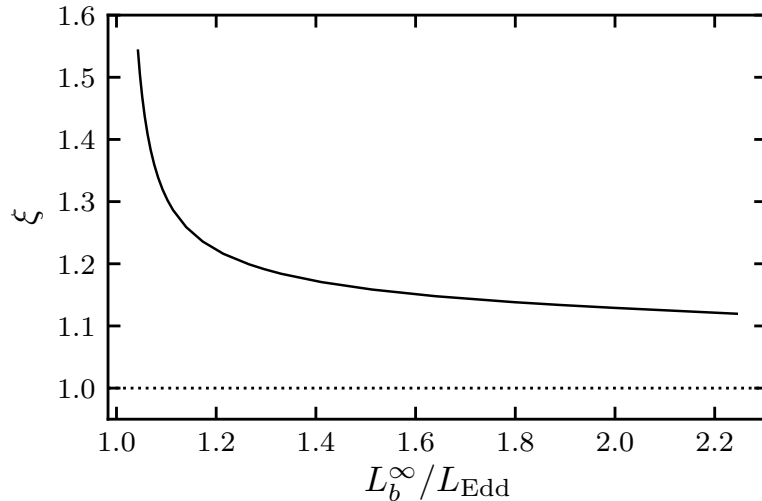


Figure 2.7: Ratio of predicted mass-loss rates from Equation (2.2) to our model values, $\xi \equiv (L_b^\infty - L_{\text{Edd}})/(G\dot{M}/R)$, as a function of the base luminosity redshifted to infinity.

2.4 The Transition between Expanded Envelopes and Winds

In this section, we discuss the evolution of the envelope during PRE bursts, where the luminosity L_b^∞ is time-dependent. We explore our grid of models as a function of the base flux, and discuss its applicability for quasi-static calculations of bursts.

2.4.1 Comparison between Expanded Envelopes and Winds as a Function of Base Luminosity

Figure 2.8 shows the base temperature (at a column depth $y_b = 10^8 \text{ g cm}^2$), photospheric and sonic radius, and sound-crossing and flow timescales, all as a function of the base luminosity in Eddington units. The static envelope models lie to the left ($L_b^\infty \lesssim L_{\text{Edd}}$) and the winds to the right ($L_b^\infty \gtrsim L_{\text{Edd}}$). The corresponding values of \dot{M} are shown in the top panel.

In the top panel of Figure 2.8, we see that the envelope and wind models lie on a common track in the T_b – L_b plane. The scaling is close to $L_b \propto T_b^4$. At large \dot{M} , the base temperature approaches the radiation-pressure-limiting temperature given by $gy = aT_R^4/3$, or $T_R = 1.59 \times 10^9 \text{ K}$ ($g_{14}/1.6)^{1/4} y_8^{1/4}$ (see Appendix 2.7.3)). As discussed in Section 2.3.3, we show models up to a maximum mass-loss rate of $3 \times 10^{18} \text{ g s}^{-1}$. The static envelope models extend slightly to the right of the $L_b^\infty/L_{\text{Edd}} = 1$ line; this is because there is a small Klein-Nishina correction to the electron scattering opacity in the outer layers of our models where $T \sim 10^7 \text{ K}$ (Equation (2.8) gives $\kappa_0/\kappa \approx 1.04$ at $T = 10^7 \text{ K}$).

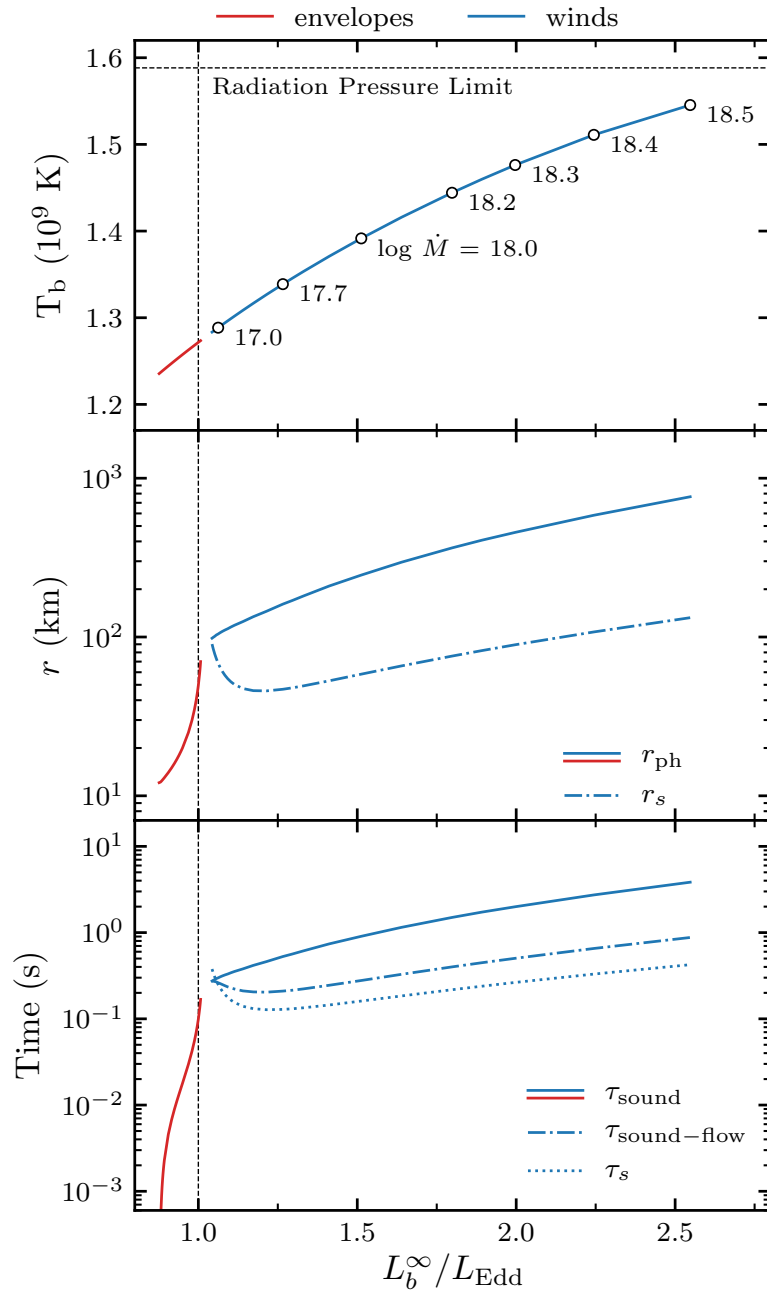


Figure 2.8: Solution space for the base luminosity as seen by observers at infinity, for both winds (blue) and envelopes (red). Eddington luminosity is marked by the vertical black dashed line. *Top:* Temperature at the base. Mass-loss rates are indicated at various points for the winds. *Middle:* Sonic and photospheric radii of solutions. *Bottom:* Characteristic timescales of the solutions (see Section 2.4.2).

We show wind solutions down to a mass-loss rate of $\dot{M} = 10^{17}$ g s⁻¹. We have not been able to obtain solutions for lower mass-loss rates than this due to numerical difficulties (see Appendix 2.7.2 for a discussion); there is a small range of luminosity between $1 \lesssim L_b^\infty / L_{\text{Edd}} \lesssim 1.05$ where we do not have a solution. As shown in the middle panel of Figure 2.8, this value of \dot{M} corresponds to the point at which the critical point of the wind becomes optically thin ($r_{\text{ph}} \approx r_s$). As discussed by [Kato & Hachisu \(1994\)](#) in the context of nova winds, acceleration becomes very inefficient when the sonic point is far outside the photosphere; steady-state wind solutions may then not be possible. [Kato & Hachisu \(1994\)](#) argued that the envelopes should smoothly evolve into wind solutions, and adjusted the boundary condition in their optically-thick models so that was the case. However, we do not see this behaviour in our models, but instead have a small luminosity difference between the maximally-extended static atmosphere and the lowest \dot{M} optically-thick wind.

With the exception of the gap between $1 \lesssim L_b^\infty / L_{\text{Edd}} \lesssim 1.05$, the middle panel of Figure 2.8 shows that the photospheric radius in our models does appear to smoothly evolve from the static envelopes to the winds. The maximally extended envelope that we find has $r_{\text{ph}} \approx 70$ km, whereas the lowest \dot{M} wind has $r_{\text{ph}} \approx 100$ km. Note that this is very different in the optically thick models. [Paczynski & Anderson \(1986\)](#) found static envelopes with photospheric radius ≈ 200 km, and we have found, reproducing their calculations, that $r_{\text{ph}} \sim 1000$ km is possible with the boundary condition $\tau = 2/3$ at the photosphere. These large photospheric radii are much greater than the ~ 100 km of the wind solutions. Our models show instead that the optical depth at the photosphere in the extended envelopes increases toward $\tau \approx 3$ as the envelope becomes more extended (see Figure 2.5), and the photospheric radius

monotonically increases, smoothly transitioning into the wind solutions.

2.4.2 The Timescale to Reach a Steady state

With wind velocities of $v_\infty \approx 3 \times 10^8 \text{ cm s}^{-1}$, the flow timescale is $t_{\text{flow}} = r/v_\infty \sim 0.03 \text{ s}$ ($r/100 \text{ km}$). This is much shorter than the typical $\gtrsim 1 \text{ s}$ timescale of the super-Eddington phases of bursts, justifying the use of steady-state hydrodynamic equations to calculate the wind structure. Indeed, as long as the ratio of flow time to evolution time remains small, it should be appropriate to use steady-state wind solutions as outer boundary conditions for calculations of the interior evolution ([Joss & Melia 1987](#)). Because the wind photospheres with GR effects included remain at large radii $\sim 100 \text{ km}$ even for small mass-loss rates, it means that the photosphere has to adjust by a large amount when the base luminosity crosses the Eddington limit, perhaps calling into question whether this quasi-static approach is applicable.

The bottom panel of Figure 2.8 shows the flow and sound crossing timescales for the different models. Hydrostatic balance is established on a timescale given by the sound crossing time,

$$\tau_{\text{sound}} = \int_R^{r_{\text{ph}}} c_s^{-1} dr, \quad (2.30)$$

which gives the time taken for a sound wave to travel the structure, from the base to the photosphere. For winds, a characteristic timescale for the flow is

$$\tau_s = \frac{r_s}{c_s(r_s)} = \frac{r_s}{v(r_s)}. \quad (2.31)$$

We could also define the flow crossing time

$$\tau_{\text{flow}} = \int_R^{r_{\text{ph}}} v^{-1} dr, \quad (2.32)$$

but this has the problem that the velocity is so small near the neutron star surface that the flow time is dominated by these regions, and is therefore not representative of the whole solution. Instead, we take a timescale that combines the sound crossing time of hydrostatic regions, up to the sonic point, followed by the flow crossing time in the outflowing regions of the wind, up to the photosphere,

$$\tau_{\text{sound-flow}} = \int_R^{r_s} c_s^{-1} dr + \int_{r_s}^{r_{\text{ph}}} v^{-1} dr. \quad (2.33)$$

Figure 2.8 shows that these wind timescales have similar values and progressions with L_b^∞ , except for low mass-loss rates where the increase in sonic point radii results in larger crossing times. In every model, by looking at the bottom two panels in Figure 2.8, it is clear that it is the photospheric radius which largely dictates the timescales. This means that more extended structures take longer to form, and that they cannot exist under a rapidly varying luminosity.

Typical PRE bursts have a duration of $\lesssim 10$ s, with Eddington phases shorter than a few seconds ([Galloway et al. 2008a](#)), although as discussed in Section 2.1.1, there are bursts with much longer durations ([in 't Zand & Weinberg 2010](#)). Since the rising phase is so fast in transitioning from sub to super-Eddington luminosities, it is clear that our stationary solutions are not appropriate for describing its dynamics. At the high end of luminosities for static envelopes, the extended region takes ~ 0.1 s to adjust to a small change in surface flux and expand its photosphere further. This is too long for the burst rise to go through each solution in succession. A time-dependent calculation is therefore needed to model this part of the burst. However, our timescales would allow for the Eddington and decaying phase to be reasonably be modelled by steady-state winds and envelopes respectively. The quasi-static approach

is therefore appropriate to PRE model bursts once they reach Eddington. For bursts with $r_{\text{ph}} \ll 100$ km, static envelope models can be used as well, since they never reach Eddington and cross into the wind regime. Our timescales appear consistent with the time-dependent Newtonian calculations of [Yu & Weinberg \(2018\)](#), which have fairly constant \dot{M} profiles after ≈ 1 s.

2.4.3 Energetics of the Expansion

A further consideration in modelling the evolution of the envelope quasi-statically is the energy required to establish the expanded configuration, i.e. to move from one model to the next as L_b^∞ increases. We compute the energy of a given model above radius r as

$$E(r) = \int_r^{r_{\text{ph}}} [U\zeta^{-1} + \rho c^2(1 - \zeta^{-1})] 4\pi r'^2 dr', \quad (2.34)$$

where the first term is the internal energy and the second is the gravitational binding energy ([Fowler 1964](#)). The energy of the static envelope solutions is shown in Figure 2.9 as a function of the mass coordinate

$$m \equiv \int_r^{r_{\text{ph}}} \rho 4\pi r'^2 dr', \quad (2.35)$$

which measures the mass between radius r and the photosphere. In order to focus on the change in energy as the envelope expands outward, we show the difference in energy $\Delta E = E - E_0$, where E_0 is the energy of the most compact envelope that we calculated.

We see that small increases in the photospheric radius (up to ~ 50 m) are associated with an energy per gram $\lesssim 10^{18}$ erg g $^{-1}$ or equivalently $\lesssim 1$ MeV per nucleon

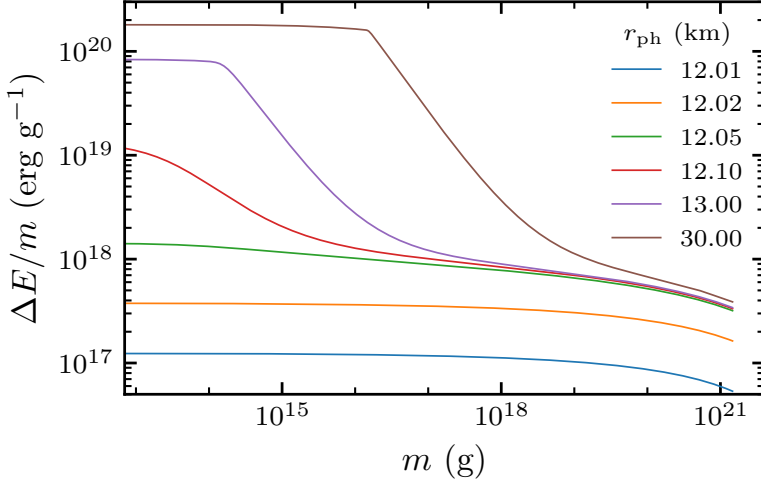


Figure 2.9: The energy per unit mass as a function of mass coordinate compared to an envelope with $r_{\text{ph}} = 12.005$ km. This shows the energy that must be given to the envelope above each mass coordinate in order to expand outward. The mass coordinate m measures the mass contained above a given point (to the photosphere). The total mass of the envelope is $\approx 10^{21}$ g.

that is fairly uniformly distributed across the envelope. With a total mass $\sim 10^{21}$ g, the total energy is $\sim 10^{39}$ erg (note that this is roughly what we would expect to lift $m = 10^{21}$ g a height $H \sim 100$ m with $g \sim 10^{14}$ cm s $^{-2}$, i.e. $mgH \sim 10^{39}$ erg). At this point, the base temperature has increased to a value where radiation pressure is becoming important at the base of the model. Further expansion occurs by lifting the outer parts of the envelope outward. For example, in the model with photospheric radius of 30 km, the outermost $\approx 10^{16}$ g is given an energy $\sim 10^{20}$ erg g $^{-1} \sim GM/R$, allowing it to move to large radius. However, this represents only $\sim 10^{-5}$ of the mass of the envelope; the rest remains in a compact configuration.

Because only a small fraction of the mass is lifted outward, the amount of energy required for the solutions with extended photospheres is not significantly more than the compact envelopes, and is readily supplied by nuclear burning. For example, in

the model with $r_{\text{ph}} = 30$ km, lifting 10^{16} g outward requires $\sim 10^{36}$ erg, which is supplied in < 0.01 s at the Eddington luminosity. As long as the base luminosity evolves on a longer timescale, these energetic requirements are easily met.

For wind models, since the energy released from nuclear burning $E_{\text{nuc}} \sim 1$ MeV/nucleon is ~ 100 times smaller than the gravitational binding energy GM/R , no more than $\sim 1\%$ of the accreted mass may be fully ejected. In steady-state, this leads to the requirement that the ratio of mass within the sonic point to mass outside the sonic point $m_{r < r_s}/m_{r > r_s}$ should be larger than ≈ 100 (where the mass m is given by Equation (2.35) with modified integration bounds) ([Paczynski & Proszynski 1986](#)). Note that with the equation for the mass-loss rate (Equation (2.5)), this mass ratio can be re-written as the ratio of flow times (Equation (2.32)) between subsonic and supersonic regions (up to a factor of Ψ), which [Quinn & Paczynski \(1985\)](#) used to rule out models with large \dot{M} . In our case, these ratios are larger than 500 for all models. Our criterion for the maximum mass-loss rate based on β_b (Section 2.3.3) turned out to be more restrictive.

2.5 Observational Implications

We now discuss the implications of our models for observations of PRE bursts. We first discuss the expected photospheric radii in PRE bursts (Section 2.5.1). In Section 2.5.2, we calculate gravitational redshifts and velocity blueshifts for our wind models and review them in the context of [Strohmayer et al. \(2019\)](#). In Section 2.5.3, we discuss the location of the photosphere when the luminosity is close to Eddington and implications for identifying the touchdown point in observations of PRE bursts.

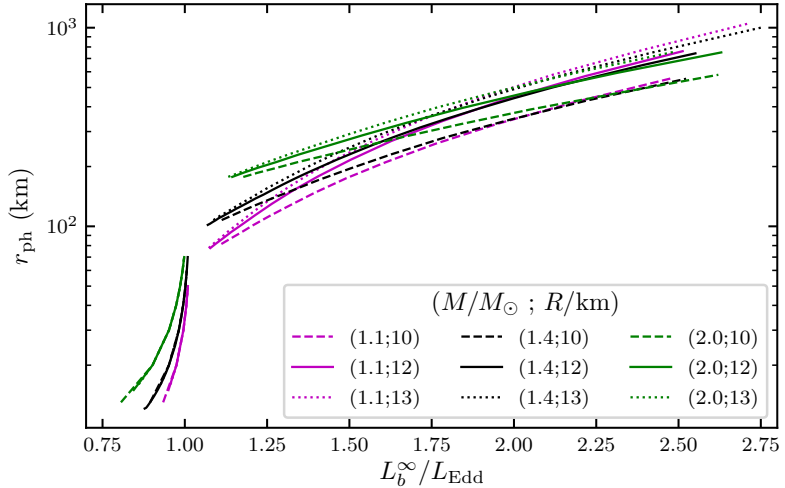


Figure 2.10: Photospheric radii of wind and envelope models for neutron stars with varying masses and radii. The solid black line represents the models shown throughout this paper.

2.5.1 Photospheric Radii

We find in our models that there is a separation between the photospheric radii of envelopes and winds. Static envelopes have photospheric radii $\lesssim 100$ km; winds have $r_{\text{ph}} > 100$ km (see middle panel of Figure 2.8). Whereas optically-thick envelopes are able to extend to $r_{\text{ph}} > 100$ km, we find that once we relax that assumption, the photospheric radius evolves smoothly between envelopes and winds, as discussed in Section 2.4.2.

Figure 2.10 shows further results for the photospheric radius, now for different choices of neutron star mass and radius. Interestingly, for static envelopes and winds with low mass-loss rates, the photospheric radius is independent of neutron star radius, whereas for high mass-loss rate winds the photospheric radius becomes independent of neutron star mass. We also calculated pure hydrogen and solar composition ($X = 0.7, Y = 0.28, Z = 0.02$) models, instead of pure He, and found only minor

differences. The largest change in photospheric radius was an increase by $\approx 30\%$ for H or solar composition winds compared to helium winds.

We define the photospheric radius as the location where the gas temperature T is equal to the effective temperature T_{eff} . Observationally, the photospheric radius is inferred from blackbody fits, with a color correction applied to correct the measured color (blackbody) temperature to the effective temperature. In a scattering atmosphere with coherent scattering, the radiation temperature is set at the thermalization depth where the last absorption occurs and then photon scatter outward to the scattering photosphere. [Joss & Melia \(1987\)](#) found that the ratio of absorption to scattering opacity at the photosphere is ~ 0.01 , leading to thermalization depths $\approx 3\text{--}5$ times smaller than the scattering photosphere. However, they also showed that Compton scattering in the region between the thermalization depth and the scattering photosphere is effective in coupling the radiation and gas temperatures (although with constant photon number).

For compact atmospheres near the Eddington limit, calculations of the spectrum find color correction factors $f_c = T_c/T_{\text{eff}} \approx 1.5\text{--}2$ near Eddington luminosity ([Pavlov et al. 1991](#); [Suleimanov et al. 2011](#)). The spectrum is harder than a blackbody, so that the blackbody radius underestimates the true emission radius by a factor of $f_c^2 \approx 2\text{--}4$. For winds, [Titarchuk \(1994\)](#) and [Shaposhnikov & Titarchuk \(2002\)](#) found that the situation reverses, $f_c < 1$, so that the blackbody radius overestimates the true emission radius.

Observationally, most PRE bursts have modest expansions of tens of km ([Gal- loway et al. 2008a](#)), consistent with being due to expanded atmospheres rather than

winds. Paczynski & Proszynski (1986) made a similar point, that with large photospheres and therefore correspondingly low temperatures, wind solutions did not appear to match observations of bursts. Superexpansion bursts (in 't Zand & Weinberg 2010) do have blackbody radii of hundreds of km, consistent with wind solutions. The color corrections described earlier do not appear to change the conclusion that in the context of light element models, most observed PRE bursts do not have a wind.

2.5.2 Spectral Shifts

Next, we investigate the importance of spectral shifts in our wind models. Redshift comes from relativistic curvature,

$$1 + \frac{\Delta\lambda_{\text{red}}}{\lambda_0} = \left(1 - \frac{2GM}{r_0c^2}\right)^{-1/2} = \frac{1}{\zeta(r_0)}, \quad (2.36)$$

where r_0 is the emission radius and λ_0 is the emission wavelength. Blueshift comes from the special relativistic Doppler effect,

$$1 + \frac{\Delta\lambda_{\text{blue}}}{\lambda_0} = \sqrt{\frac{1 - v_0/c}{1 + v_0/c}}, \quad (2.37)$$

where v_0 is the gas velocity at r_0 . In the top panel of Figure 2.11, we see that redshift dominates everywhere before the sonic point, where it can reach values of several percent. After the sonic point and approaching the photosphere, redshift and blueshift become comparable to the point where the total spectral shift is close to zero. In the bottom panel, we note the changing sign of $\Delta\lambda$ at high \dot{M} , as both velocities and photospheric radii increase, although being able observing such small shifts is unlikely.

We can see from the bottom panel of Figure 2.11 the total shift of wind models

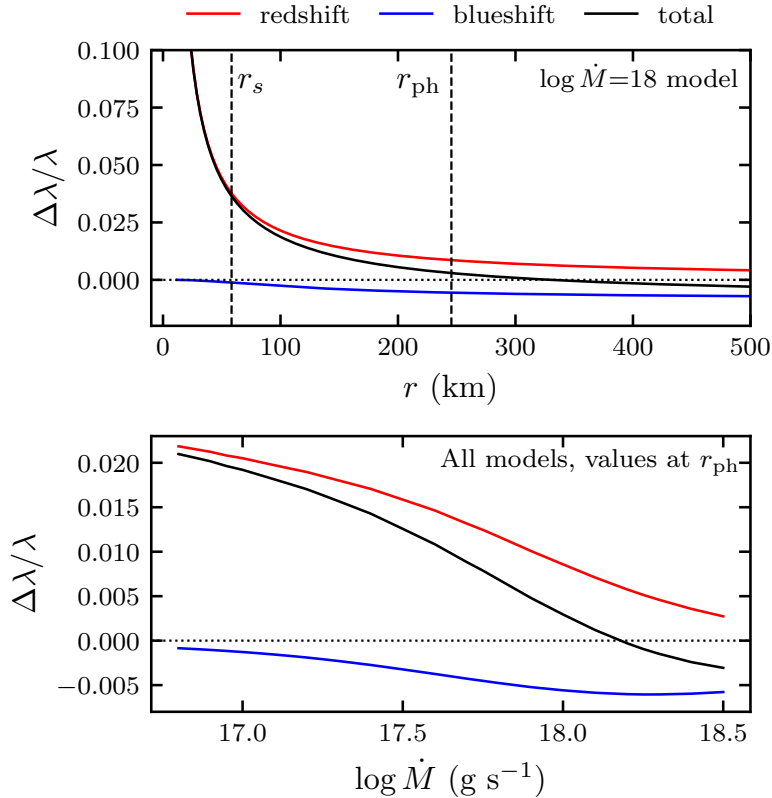


Figure 2.11: Wind spectral shifts, as a function of the radial coordinate for the $\log \dot{M} = 18$ model (top), and as a function of \dot{M} at the photosphere (bottom).

at the photosphere is of at most 2%. As for the relative shift of individual lines during different burst, if two lines λ_1 and λ_2 are shifted from their rest frame wavelength λ_0 by $\Delta\lambda_1$ and $\Delta\lambda_2$, then their relative shift is

$$\frac{\lambda_1}{\lambda_2} = \frac{\lambda_0 + \Delta\lambda_1}{\lambda_0 + \Delta\lambda_2} \approx 1 + \frac{\Delta\lambda_1}{\lambda_0} - \frac{\Delta\lambda_2}{\lambda_0}, \quad (2.38)$$

so that relative shifts of at most ≈ 1.02 are expected. For a heavier star, e.g. with a $2 M_\odot$ mass, the minimum photospheric radius is still > 100 km (Figure 2.10), and the maximum relative shift increases by 1%. This only applies for winds, as static envelopes can have stronger redshifts given their smaller photospheric radii. [Strohmayer et al. \(2019\)](#) found a relative shift of ≈ 1.046 , with the observed photospheres of the

weaker bursts being at ≈ 75 km. Even so, gravitational redshift alone cannot explain this value (if the mass is $\leq 2.0 M_{\odot}$, see their Figure 9), prompting them to suggest a blueshift contribution. Our results do not support this scenario, as the observed photospheric radii would imply static solutions rather than winds. Even in the wind case, models with small photospheric radii have very weak blueshifts ($\lesssim 1\%$) at the photosphere (Figure 2.11).

We must also note that the emission radius of spectral lines is likely not at the helium scattering photosphere. Heavier elements that are thought to be ejected have more complex interactions with radiation, and spectral lines and edges themselves are not a continuum effect, which is how radiation is treated in our model. Our wind models can describe the relative importances of redshift and blueshift, but true predictions on spectral lines will require a more sophisticated treatment of radiative transfer.

2.5.3 Compact Envelopes and Touchdown Radius

We discussed in Section 2.1.1 the common technique of finding the neutron star radius based on measuring the touchdown flux, i.e. the flux when the temperature peaks and the photosphere presumably touches back down to the surface following the PRE phase of the burst. But if the luminosity at the touchdown point is still near-Eddington, an expanded envelope could be present, which means that the photospheric (touchdown) radius is not the neutron star radius. This difference enters into the redshift factor that relates the Eddington flux at the neutron star surface and the observed luminosity. To investigate this question, we have extended our cal-

culation of envelopes to very compact ones with photospheres less than 1 km above the neutron star surface.

The top panel of Figure 2.12 shows the relation between the luminosity and the extension of the photosphere above the neutron star surface. The range of luminosities that would cause a significant difference between the touchdown and neutron star radius ($\gtrsim 100$ m) is quite narrow, from $\sim 0.85 L_{\text{Edd}}$ to $\sim L_{\text{Edd}}$. As [Paczynski & Anderson \(1986\)](#) pointed out, this large expansion is only possible in GR, as Newtonian envelopes can only be compact; we show Newtonian models as a dotted line in Figure 2.12 (an analytic solution for Newtonian envelopes is derived in Appendix 2.7.4). As luminosity increases, the envelope begins to expand significantly when the local luminosity at the surface of the star first becomes critical. Our range of luminosities where significant expansion occurs is smaller than [Paczynski & Anderson \(1986\)](#), who predicted expansion for $L \gtrsim 0.77 L_{\text{Edd}}$, derived with $L_{\text{ph}} \approx L_{\text{cr}}(r_{\text{ph}}) \approx L_{\text{Edd}}/\zeta(r_{\text{ph}})$, assuming $\kappa(r_{\text{ph}}) \approx \kappa_0$. This second approximation is incorrect, since the temperature at the photosphere for models with moderate expansion can still be quite high. For example, the model with $r_{\text{ph}} = 12.1$ km has a photospheric temperature of 2.6×10^7 K, giving $\kappa(r_{\text{ph}}) = 0.92 \kappa_0$ and thus $L^\infty = 0.87 L_{\text{Edd}}$.

In the bottom panel of Figure 2.12, we plot the effective temperature T_{eff} of the envelope (redshifted to infinity with $T^\infty = \zeta T$) as a function of the photospheric radius. To check for potential variations due to color corrections, we also show the expected color temperature calculated using the analytic result from [Pavlov et al. \(1991\)](#) that applies to compact atmospheres. The peak temperature occurs when the photosphere is close to the surface, within ~ 30 m. However, the temperature is very flat with increasing r_{ph} , which means that a small uncertainty in the peak temperature

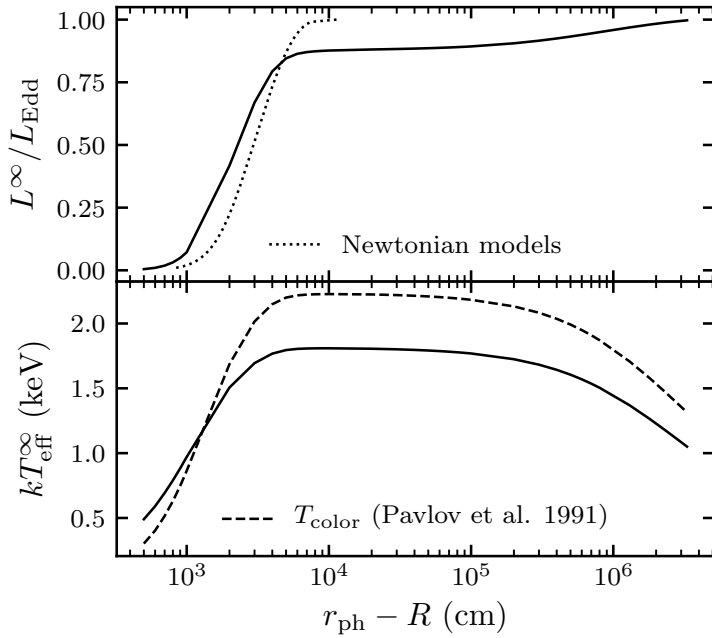


Figure 2.12: Difference between the photospheric (touchdown) radius based on the luminosity (top) and observed effective temperature (bottom). The dotted line in the top panel represents Newtonian atmospheres, for which we derive an analytical formula in Appendix 2.7.4. The dashed line in the bottom panel gives the color temperature of the atmosphere with the correction factor of Pavlov et al. (1991).

can correspond to a relatively large uncertainty in the position of the photosphere. For example, when the photosphere is 1 km from the surface, the observed temperature is within 3% of its peak value.

Our results provide evidence for the suggestion of Steiner et al. (2010) that the photosphere might still not have returned fully to the neutron star surface at the point of the burst identified as touchdown. They argued that the ratios of photospheric radius to neutron star radius implied by their analysis were > 1.1 , > 1.4 and > 5 for three different data sets that they considered. The last of these, a factor of 5, does not seem likely since the temperature is then well away from its peak value (even when including possible color correction variations; see Özel et al. 2016). However, overes-

timation of the photospheric radius at touchdown of order $\sim 10\%$ due to uncertainties in the measured temperature is more plausible given the results in Figure 2.12. Note that because the photospheric radius at touchdown appears inside a redshift factor, the corresponding uncertainty in the inferred neutron star radius will be smaller still by a factor of a few.

2.6 Summary and Discussion

We constructed a sequence of self-consistent models of light element static expanded envelopes and steady-state winds resulting from near or super-Eddington luminosities in type I X-ray bursts³. We included general relativistic corrections that are necessary to correctly model the expansion of the envelope when the photosphere is close to the stellar surface. We also improve upon the earlier work of Paczynski & Anderson (1986) and Paczynski & Proszynski (1986) by using flux-limited diffusion to model the transition from the optically-thick to optically-thin parts of the envelope. The optical depth at the photosphere then naturally transitions from close to $\tau = 2/3$ for geometrically thin envelopes to $\tau \approx 3$ in the wind solutions (Figure 2.5).

With this self-consistent treatment of the photosphere in hand, the models give the following picture for the evolution during the rising phase of a PRE burst. At low luminosity, the envelope is geometrically thin, and undergoes modest expansion with increasing luminosity. However, eventually, the luminosity at the stellar surface reaches the critical luminosity (the local Eddington limit), and the envelope adjusts by

³The models are available at <https://github.com/simonguichandut/GR-FLD-PRE>.

expanding outward. Over a narrow range of luminosity from $0.8 \lesssim L_b^\infty \lesssim 1$, the envelope remains in hydrostatic balance but the photospheric radius moves smoothly outward to a radius of $\approx 50\text{--}80$ km when $L_b^\infty \approx L_{\text{Edd}}$ (Figure 2.10). For $L_b^\infty \gtrsim 1.05 L_{\text{Edd}}$, an optically-thick wind develops, with photosphere located at > 100 km. The radiative luminosity of the wind is within 1% of the Eddington luminosity, with the remaining energy used to eject matter, thereby the base luminosity sets the mass-loss rate (Equation (2.28)). The maximum mass-loss rate is $\approx 2 \times 10^{18} \text{ g s}^{-1}$, determined by the available nuclear energy (Figure 2.6).

We find that there are two aspects of the burst rise that are likely not well-modeled by quasi-static evolution. For the static expanded envelopes, the large photospheric radius means that the sound crossing time of the envelope can be ~ 0.1 s, comparable to burst rise times (Figure 2.8). Second, in the range $1 \lesssim L_b^\infty / L_{\text{Edd}} \lesssim 1.05$, the sonic point of the wind is optically thin and we were not able to find steady-state solutions (Section 2.4.1). Time-dependent calculations are needed to model the evolution of the envelope as the base luminosity traverses the range from $\approx 0.8 L_{\text{Edd}}$ to $\approx 1.05 L_{\text{Edd}}$. [Yu & Weinberg \(2018\)](#) recently carried out the first time-dependent calculations of PRE bursts, and the onset of a wind, but in Newtonian gravity. It would be extremely interesting to extend this kind of work by including general relativistic corrections.

While it is encouraging that the range of photospheric radii in models agrees well with the range of observed blackbody radii in PRE bursts ($\sim 10\text{--}1000$ km; Figure 2.10), the fact that most observed PRE bursts show only modest expansion of a few tens of km is hard to explain. Photospheric radii $\lesssim 100$ km can be achieved with static envelopes, but only for a narrow range of luminosities. This requires a

fine-tuning of the energy release in the burst. A much more natural outcome of the models is that the luminosity at the base exceeds L_{Edd} , resulting in a wind with photospheric radius $\gtrsim 100$ km.

As proposed by [in 't Zand & Weinberg \(2010\)](#) and [Yu & Weinberg \(2018\)](#), heavy elements in the wind could truncate the wind and lead to smaller photospheres in agreement with observations. [in 't Zand & Weinberg \(2010\)](#) pointed out that line-driving due to hydrogenic heavy ions could play an important role. This may be particularly important to include for luminosities just above Eddington where the sonic point is optically thin and radiation pressure driving is inefficient. A truncated wind might also more naturally explain the lineshifts observed by [Strohmayer et al. \(2019\)](#), which are larger than predicted at the photospheres of our wind solutions.

The expanded envelope models also have implications for neutron star radius measurements by the touchdown method. Our models show that the photosphere is still 1 km above the surface when the effective temperature is only 3% away from its maximum value. This is a possible systematic uncertainty when interpreting the measured Eddington fluxes from bursts at touchdown. This uncertainty is not present when considering Newtonian envelopes, which remain within ≈ 100 m of the surface even close to the Eddington luminosity. The expanded nature of the envelope for $L^\infty \gtrsim 0.8 L_{\text{Edd}}$ should be included in spectral models.

The models presented in this paper are based on many assumptions, namely a non-rotating neutron star, no magnetic fields, spherical symmetry and steady-state outflows. To take full advantage of the observational data of PRE bursts, more work is needed to drop each of these assumptions. In these accreting systems, the neutron

star can have a short spin period such that the effective gravity at the surface is significantly reduced ($R\Omega^2/g = 0.01g_{14}^{-1}(R/10\text{ km})(f/500\text{ Hz})^2$). This effect changes along the latitude so that the photosphere may lift off at different times during the burst rise, or be differently extended at touchdown (Suleimanov et al. 2020). Further, magnetic field lines may entrain the ionized fluid out to an Alfvén radius, i.e. the point $r = r_A$ where $\rho u^2/2 = B^2/8\pi$ (Lamers & Cassinelli 1999). For example, in a split monopole configuration for the magnetic field, $B(r) = B_0(R/r)^2$, and a surface value $B_0 = 10^9$ G, our wind models give $r_A \approx 500\text{--}5000$ km, much farther out than the photosphere. For a dipole magnetic field $B \sim r^{-3}$, $r_A \approx 100\text{--}300$ km, closer in but still past the sonic point. This simple analysis shows that magnetic fields could very well have a strong influence on the dynamics of these outflows, and should be taken into account in future calculations. Lastly, the steady-state assumption prevents us from studying the evolution of multiple-stage bursts, such as ones in which the ejection of a hydrogen shell precedes the helium flash (see Kato 1986 for discussion), as is thought to have recently been observed by NICER (Bult et al. 2019). For all of these reasons, future work on PRE bursts modeling should aim toward multidimensional radiation magnetohydrodynamics calculations.

We thank Ninoy Rahman for useful discussions on flux-limited diffusion in general relativity. We also thank the anonymous referee for useful comments. SG is supported by an FRQNT scholarship. AC is supported by an NSERC Discovery grant and is a member of the Centre de Recherche en Astrophysique du Québec (CRAQ). ZL and AC thank the International Space Science Institute in Bern for hospitality. ZL was supported by National Natural Science Foundation of China (U1938107, U1838111), and Scientific Research Fund of Hunan Provincial Education Department (18B059).

2.7 Appendix

2.7.1 Derivation of the Steady-state Hydrodynamics Equations

In this Appendix, we derive the steady-state equations for conservation of mass (Equation (2.5)), energy (Equation (2.6)), and momentum (Equation (2.7)) from the time-dependent equations of radiation hydrodynamics in a Schwarzschild metric ([Park 2006](#)). We replace the notation of [Park \(2006\)](#) with ours, for symbols that we have previously defined. We recover c.g.s. units by adding the necessary factors of c , and remove the angular terms to consider the spherically symmetric case. The equations are:

$$\frac{1}{\zeta^2} \frac{\partial}{\partial t} (n\Psi) + \frac{1}{r^2} \frac{\partial}{\partial r} (r^2 n v \Psi) = 0$$

Continuity equation (2.39)

$$\frac{\Psi}{\zeta^2} \frac{\partial}{\partial t} (v\Psi) + \frac{1}{2} \frac{\partial}{\partial r} (v\Psi)^2 + \frac{GM}{r^2} + \frac{v\gamma^2}{\omega_g} \frac{\partial P_g}{\partial t} + \frac{c\Psi^2}{\omega_g} \frac{\partial P_g}{\partial r} = \frac{\Psi c}{\omega_g} \bar{\chi}_{\text{co}} F_{\text{co}}$$

Momentum equation (2.40)

$$\frac{n\Psi}{\zeta^2} \frac{\partial}{\partial t} \left(\frac{\omega_g}{n} \right) + nv\Psi \frac{\partial}{\partial r} \left(\frac{\omega_g}{n} \right) - \frac{\Psi}{\zeta^2} \frac{\partial P_g}{\partial t} - v\Psi \frac{\partial P_g}{\partial r} = \Gamma_{\text{co}} - \Lambda_{\text{co}}$$

Energy equation (2.41)

$$\frac{1}{\zeta^2} \frac{\partial E_{\text{fx}}}{\partial t} + \frac{1}{\zeta^2 r^2} \frac{\partial}{\partial r} (r^2 \zeta^2 F_{\text{fx}}) = \frac{\gamma}{\zeta} (\Lambda_{\text{co}} - \Gamma_{\text{co}} - \frac{v}{c} \bar{\chi}_{\text{co}} F_{\text{co}})$$

Zeroth radiation moment equation (2.42)

In these equations, n is the number density of particles, $\omega_g \equiv \rho c^2 + P_g + U_g$ is the sum of rest-mass energy and enthalpy of the gas and $\bar{\chi}$ is the mean opacity coefficient and E is the energy density of the radiation. Λ and Γ are heating and cooling functions that describe the interaction between the radiation and the gas. However, we will see that we can get rid of them to obtain our final equations. [Park \(2006\)](#) also derives higher order moment equations of radiation, however we do not need them for this work since we consider a spherically symmetric problem, and we have a standalone equation for the radiation flux (Equation (2.10)).

In GR, the notion of frames of reference is important, and two were used by [Park \(2006\)](#) to derive these equations; the fixed frame (subscript “fx”), which has no velocity with respect to the origin $r = 0$, and the comoving frame (subscript “co”), which travels with velocity u , along with the gas. A frame transformation is used to convert between quantities in both frames (see [Park \(2006\)](#) for the full details). What matters to us is that we are able to assign expressions to thermodynamic quantities in the comoving frame. The mean opacity coefficient in the frame of the moving gas can be related to the usual opacity, $\kappa \equiv \bar{\chi}_{\text{co}}/\rho$, since ρ is measured in the frame. The flux that we keep track of is always the comoving flux, so we define $F \equiv F_{\text{co}}$. The local energy density is just $E_{\text{co}} \equiv U_R = aT^4$, for thermal radiation. The comoving radiation pressure in the radial direction is $P_{\text{co}}^{rr} \equiv P_R$, which is a function of the energy density U_R and the flux limiter λ (Equation (2.14)).

We will now derive the steady-state equations. We will use the prime symbol ($'$) to denote derivatives with respect to r . From the continuity equation (2.39), it is easy to see that $r^2 n v \Psi$ is the conserved quantity in steady-state, and we can switch n for ρ since both densities are linked by the (constant) particle mass. Adding a

factor of 4π for spherical geometry leads to equation for conservation of mass and \dot{M} (Equation (2.5)). The momentum equation (2.40) can be written compactly by including both the v' and GM/r^2 terms into Ψ' , leading to our Equation (2.7).

For the steady-state energy equation, we combine Equation (2.41) and (2.42) to remove the Λ_{co} and Γ_{co} functions, giving

$$nv\Psi^2 \left(\frac{w}{n}\right)' + \frac{1}{r^2} (r^2 \zeta^2 F_{\text{fx}})' - v\Psi^2 P_g' + \frac{v\Psi}{c} \rho \kappa F = 0. \quad (2.43)$$

Adding $v\Psi^2$ times Equation (2.7) gets rid of the P_g' and F terms. We use mass conservation written as $(r^2 n u \Psi)' = 0$ to remove the n' term, giving

$$0 = \frac{1}{r^2} (r^2 \Psi^2 v w + r^2 \zeta^2 F_{\text{fx}})' . \quad (2.44)$$

We have arrived at a Bernoulli equation for the flow, where the energy in the steady-state is a balance of radiation (F_{fx}), and rest mass, gravitational, kinetic and internal energies (Ψw). To see this, we can expand Ψ to first order,

$$\Psi w \approx \left(1 - \frac{GM}{c^2 r}\right) \left(1 + \frac{1}{2} \frac{v^2}{c^2}\right) (\rho c^2 + P_g + U_g) \approx \rho \left(c^2 - \frac{GM}{r} + \frac{v^2}{2} + \frac{P_g + U_g}{\rho}\right) , \quad (2.45)$$

where we ignored cross-products of small terms. Notice that the quantity in parentheses in Equation (2.45) is the usual non-relativistic Bernoulli's constant for an ideal gas in a gravitational potential. Now to obtain the integration constant, we integrate Equation (2.44) and use the frame transformation for F_{fx} , giving

$$C = r^2 \Psi^2 v \rho \left(\frac{w + U_R + P_R}{\rho}\right) + \Psi^2 \left(1 + \frac{v^2}{c^2}\right) r^2 F . \quad (2.46)$$

Then, in Equation (2.6), $\dot{E} \equiv 4\pi C$ is the energy-loss rate.

2.7.2 Parameter Spaces

We illustrate in Figure 2.13 the parameter spaces that we search to make wind and envelope models. In our code, we first perform a grid search to find which values allow integration to infinity, which yields the black lines shown in both panels. Then, we search along these lines to find which point satisfies the surface boundary condition when integrating inward. Note that in practice, this numerical integration to infinity is not possible with a simple shooting method because of exponential growth in the stiff fluid equations ([Turolla et al. 1986](#)). To integrate our solutions outward, we always kept track of two separate solutions with similar initial values (equal to 1 part in 10^4), such that the two solutions would eventually diverge in opposite directions at some point in the integration. At that point, we interpolated values of ρ , T , v between the two initial solutions to restart the integration with new initial values, pushing the divergence to larger radii. We kept doing the same process until we reached $r_{\max} = 10^9$ cm. At the end, we verified that our models satisfied the equations of structure (Equation (2.15)]–(2.17)) by plugging values back in and comparing derivatives. This method turned out to be very useful, and we were also able to use it for some of the inward integrations to the neutron star surface that had similar stiffness issues.

In the left panel of Figure 2.13, we represented the \dot{E} free parameter as $\dot{E} - \dot{M}c^2$ to look at the energy-loss rate without the rest mass contribution. What we see is that the remaining contributions to the energy-loss rates are roughly constant and just above L_{Edd} . To explain this, we can take the energy conservation equation (2.6)

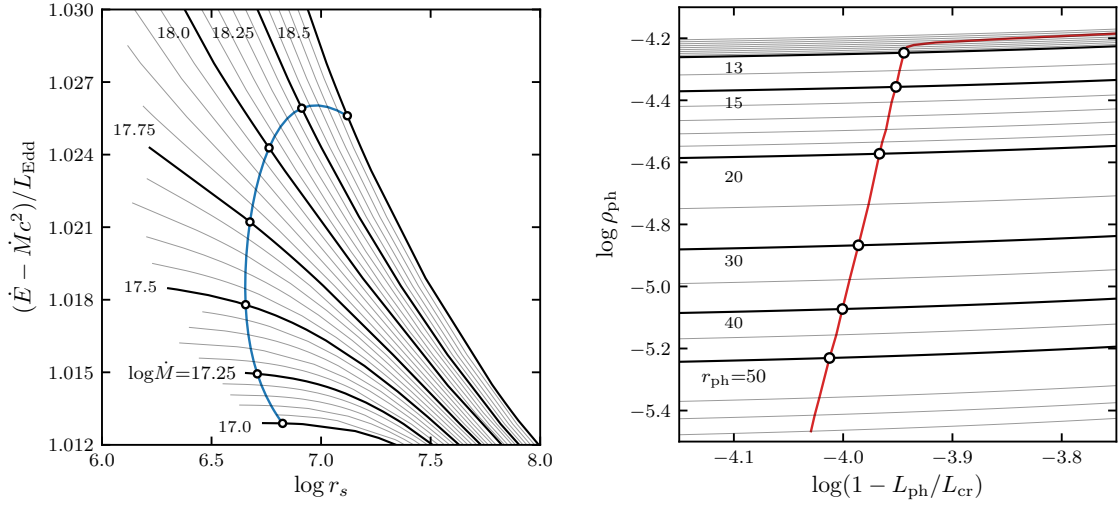


Figure 2.13: Parameter spaces for the wind (left) and envelope (right) models. The black lines trace points which allow a transition to optically thin and non-diverging integration to infinity. The thicker black lines are labelled by the mass-loss rates (in g s^{-1}) for winds, and the photospheric radii (in km) for envelopes. The blue and red lines trace out the points which satisfy the surface boundary condition.

and evaluate it at infinity,

$$\dot{E} = L^\infty \gamma_\infty^2 (1 + v_\infty^2/c^2) + \dot{M} \gamma_\infty (c^2 + w_\infty), \quad (2.47)$$

$$\dot{E} - \dot{M}c^2 \approx L^\infty \gamma_\infty^2 (1 + v_\infty^2/c^2) + \dot{M}c^2(\gamma_\infty - 1) + 2L^\infty \gamma_\infty v_\infty/c, \quad (2.48)$$

where the “ ∞ ” subscript indicates evaluation at infinity for all variables. For the enthalpy at infinity w_∞ , we took the same estimate as in Equation (2.27). Equation (2.48) shows that v_∞ essentially dictates the small variance of $\dot{E} - \dot{M}c^2$ in Figure (2.13). Indeed, in the first term, $L^\infty \sim L_{\text{Edd}}$ for all models, and the last term can be neglected since, naturally, $T_\infty \rightarrow 0$. All that is left are terms of v_∞ . This is consistent with the velocity profiles in Figure 2.1, where we see that the velocity asymptotically tends to higher values as \dot{M} increases, except at the very high end of mass-loss rates, where it then begins to decrease.

For winds, numerical difficulties arise at the low end of the mass-loss rate, and we stopped our parameter space exploration at $\log \dot{M} = 16.8$. This is because the sonic point radius quickly approaches the photosphere as \dot{M} decreases, which can be seen in the middle panel of Figure 2.8 (this was also the case in [Paczynski & Proszynski \(1986\)](#)). This makes the outer integration extremely sensitive to the exact value of r_s and \dot{E} , which can be seen in the left panel of Figure 2.13 with the lines of acceptable values becoming nearly flat.

In the right panel of Figure 2.13, we plotted against $q_{\text{ph}} \equiv (1 - L_{\text{ph}}/L_{\text{cr}})$ instead of L^∞ for better visualization. Note that there is a direct mapping between the two factors since $L_{\text{ph}} \equiv L(r_{\text{ph}}) = L^\infty \zeta(r_{\text{ph}})^{-2}$ and L_{cr} is a function of r_{ph} and T_{ph} , which is itself a function of L^∞ with Equation (2.23). The values of q_{ph} that we obtain for extended envelopes are much smaller than those of [Paczynski & Anderson \(1986\)](#) (see their Figure 2), likely because of our different treatment of the photosphere. For very compact envelopes, discussed in Section 2.5.3, q_{ph} becomes much larger, as can be seen in Figure 2.13. Static atmospheres generally become convective as L approaches L_{cr} ([Joss et al. 1973](#)). However, in our case the values of $\beta = P_g/P$ are sufficiently low that convection is avoided (see Figure 39 of [Paxton et al. 2013](#)), as discussed by [Paczynski & Anderson \(1986\)](#) for extended envelopes.

2.7.3 Pressure Conditions at the Wind Base

In this Appendix we derive the ratio of gas pressure to total pressure β expected in the initial stages of a burst. At constant pressure or column depth, nuclear burning generating an energy E_{nuc} will raise the temperature of matter from T_0 to T according

to

$$E_{\text{nuc}} = \int_{T_0}^T c_P dT, \quad (2.49)$$

where c_P is the heat capacity. For a mixture of ideal gas and radiation, $c_P = (5k_B/2\mu m_p)f(\beta)$ where $f(\beta) = (32 - 24\beta - 3\beta^2)/5\beta^2$ (Clayton 1983). Note that for $\beta \sim 1$ (gas pressure dominates), $f(\beta) \approx 1$ giving the standard ideal gas result for c_P . When $\beta \ll 1$, $f(\beta)$ diverges because fixing pressure also fixes temperature for a photon gas. The diverging heat capacity limits the final temperature to $T < T_R$, where T_R is the radiation-pressure-limited temperature given by $gy = aT_R^4/3$ or $T_R = 1.59 \times 10^9$ K ($g_{14}/1.6$) $^{1/4}y_8^{1/4}$.

We make the change of variables $\eta \equiv 1 - \beta = aT^4/3P$, where $P = gy$ in hydrostatic equilibrium. E_{nuc} is large enough that we can assume $T \gg T_0$ and Equation (2.49) can be re-written as

$$E_{\text{nuc}} = \frac{5}{8} \frac{k_B T_R}{\mu m_p} \int_0^\eta \frac{5 + 30\eta - 3\eta^2}{\eta^{3/4}(5 - 10\eta + 5\eta^2)} d\eta = \frac{1}{2} \frac{k_B T_R}{\mu m_p} \frac{\eta^{1/4}(3\eta + 5)}{1 - \eta}. \quad (2.50)$$

In the limit where $\beta = 1 - \eta \ll 1$, the expected value of β is $\beta \approx 4k_B T_R / \mu m_p E_{\text{nuc}} \approx 0.06 g_{14}^{1/4} y_8^{1/4} \mu^{-1} E_{\text{nuc},18}^{-1}$, which is the expression used in Section 2.3.3.

2.7.4 Analytical Newtonian Envelopes

Paczynski & Anderson (1986) showed a simple calculation for the most extended envelope in Newtonian gravity, one for which the luminosity ratio $\Gamma \equiv L/L_{\text{Edd}} = 1$. Here we extend this calculation to the general case $\Gamma \leq 1$. With no general relativistic corrections, the hydrostatic balance and photon diffusion equations are simply written

as

$$\frac{dP}{dr} = -\frac{GM\rho}{r^2} \quad ; \quad \frac{dP_R}{dr} = -\frac{\rho\kappa L}{4\pi r^2 c}. \quad (2.51)$$

This leads to

$$\frac{dP_R}{dP} = \frac{L}{L_{\text{cr}}} = \Gamma \frac{\kappa}{\kappa_0} = \Gamma \left[1 + \left(\frac{T}{T_0} \right)^\alpha \right]^{-1}, \quad (2.52)$$

where $T_0 = 4.5 \times 10^8$ K and $\alpha = 0.86$ are from the opacity formula Equation (2.8).

We may re-write Equation (2.52) as

$$dP = \frac{1}{\Gamma} \frac{4a}{3} \left[1 + \left(\frac{T}{T_0} \right)^\alpha \right] T^3 dT \quad (2.53)$$

which we integrate from the photosphere r_{ph} where we assume $T \approx 0$ and thus $P \approx 0$, giving the general expression

$$P(T) = \frac{1}{\Gamma} \frac{aT^4}{3} \left[1 + \frac{4}{4+\alpha} \left(\frac{T}{T_0} \right)^\alpha \right]. \quad (2.54)$$

This also leads to an expression for the density, since $P_g = P - P_R = kT\rho/\mu m_p$, such that

$$\rho(T) = \frac{1}{\Gamma} \frac{\mu m_p}{k} \frac{aT^3}{3} \left[1 - \Gamma + \frac{4}{4+\alpha} \left(\frac{T}{T_0} \right)^\alpha \right] \quad (2.55)$$

Putting this back into Equation (2.51), we obtain a differential equation for T ,

$$\left[1 + \left(\frac{T}{T_0} \right)^\alpha \right] \left[1 - \Gamma + \frac{4}{4+\alpha} \left(\frac{T}{T_0} \right)^\alpha \right]^{-1} dT = -\frac{1}{4} \frac{\mu m_p}{k} \frac{GM}{r^2} dr. \quad (2.56)$$

This can be integrated from the photosphere. The $\Gamma = 1$ case is straightforward and leads to the expression in [Paczynski & Anderson \(1986\)](#),

$$\frac{GM}{r} \frac{\mu m_p}{kT} \frac{1}{4+\alpha} \left(1 - \frac{r}{r_{\text{ph}}} \right) = 1 + \frac{1}{1-\alpha} \left(\frac{T_0}{T} \right)^\alpha. \quad (2.57)$$

If $\Gamma < 1$, we instead have

$$\begin{aligned} & \frac{GM}{r} \frac{\mu m_p}{kT} \frac{1}{4+\alpha} \left(1 - \frac{r}{r_{\text{ph}}} \right) \\ &= 1 - \left(1 - \frac{4}{(4+\alpha)(1-\Gamma)} \right) {}_2F_1 \left(1, \frac{1}{\alpha}; 1 + \frac{1}{\alpha}; \frac{-4(T/T_0)^\alpha}{(4+\alpha)(1-\Gamma)} \right), \end{aligned} \quad (2.58)$$

where ${}_2F_1$ is the hypergeometric function. All that is required to find r_{ph} for a given Γ is to have a known pair (r, T) somewhere in the envelope. For example, [Paczynski & Anderson \(1986\)](#) assumed a constant $T = 2 \times 10^9$ K at $r = R$. For consistency, we use our boundary condition $P = gy_b$ with $y_b = 10^8$ g cm $^{-2}$ at $r = R$, which we can easily solve for T since Equation (2.55) gives $\rho = \rho(T)$. This is how we computed the Newtonian envelope models shown in Figure 2.12.

From steady-state to time-dependent

This chapter presented our set of self-consistent burst outflow models. While some observational consequences could be extracted, such as the potential size of spectral shifts and the separation between the touchdown and neutron star radii, it became apparent that many other effects required a true time-dependent calculation. And while we showed that our models could in principle be coupled quasi-statically to a time-dependent calculation of the burning layer, it would be difficult to account for a wind with evolving composition, for example.

The timing of this realization was interesting, and fortunate. Months before we started working on this project, [Yu & Weinberg \(2018\)](#) published the first simulations of PRE bursts with `MESA`. Then, the NICER results (Section 1.3) started to come out. Motivated in particular by [Bult et al. \(2019\)](#), we decided to use `MESA` to simulate helium-triggered bursts underneath a hydrogen-rich shell.

We would be pleased to find that our simulations naturally produced observable pauses. Moreover, the exact shape of the lightcurve was directly determined by convection. However, looking at the details of how convection was being handled, we found that things were not so simple. These findings are the reason why the word “convection” features in the title of this thesis.

Chapter 3

The Imprint of Convection on Type I X-Ray Bursts: Pauses in Photospheric Radius Expansion Lightcurves

*This thesis chapter originally appeared in the literature as
Guichandut and Cumming 2023, *The Astrophysical Journal (ApJ)*, 954,
54. <https://doi.org/10.3847/1538-4357/ace43c>*

Authors

Simon Guichandut¹, Andrew Cumming¹

¹Department of Physics and Trottier Space Institute, McGill University, 3600 rue University, Montreal, QC, H3A 2T8, Canada

Abstract

Motivated by the recent observation by NICER of a type I X-ray burst from SAX J1808.4–3658 with a distinct “pause” feature during its rise, we show that bursts which ignite in a helium layer underneath a hydrogen-rich shell naturally give rise to such pauses, as long as enough energy is produced to eject the outer layers of the envelope by super-Eddington winds. The length of the pause is determined by the extent of the convection generated after ignition, while the rate of change of luminosity following the pause is set by the hydrogen gradient left behind by convection. Using the **MESA** stellar evolution code, we simulate the accumulation, nuclear burning and convective mixing prior to and throughout the ignition of the burst, followed by the hydrodynamic wind. We show that the results are sensitive to the treatment of convection adopted within the code. In particular, the efficiency of mixing at the H/He interface plays a key role in determining the shape of the lightcurve. The data from SAX J1808.4–3658 favors strong mixing scenarios. Multidimensional simulations will be needed to properly model the interaction between convection and nuclear burning during these bursts, which will then enable a new way to use X-ray burst lightcurves to study neutron star surfaces.

3.1 Introduction

As per the recent MINBAR catalogue (Galloway et al. 2020), about one fifth of type I X-ray bursts from accreting neutron stars (Lewin et al. 1993; Galloway & Keek 2021) reach high enough luminosities to provoke a radiatively-driven expansion of the neutron star envelope. In these “photospheric radius expansion” (PRE) bursts, the star’s photosphere moves outward and appears 10–100 times larger, for a few to tens of seconds. PRE bursts offer a unique opportunity to study not only the surface but also the interior of neutron stars. Indeed, they have been used to place joint constraints on both neutron star mass and radius and the dense matter equation of state (Özel et al. 2016, and references therein). Another way to constrain the mass is to measure the gravitational redshift of spectral features from heavy elements being ejected during the burst (Li et al. 2018; Strohmayer et al. 2019). These techniques rely on theoretical models which describe the expansion of the star’s envelope and the winds that drive it.

The recent deployment of the Neutron Star Interior Composition Explorer (NICER) telescope has drastically improved observations of PRE bursts, since the instrument’s soft X-ray response allows spectral evolution of the PRE to be followed as the blackbody temperature drops to $\lesssim 1$ keV (Keek et al. 2018). A most interesting PRE burst was recently observed by NICER from the millisecond pulsar SAX J1808.4–3658 (Bult et al. 2019). During the burst rise, the luminosity briefly “paused” for ≈ 0.7 s before reaching its peak. The ratio between the bolometric luminosity at the peak and pause was ≈ 1.68 , which is very similar to the ratio between the pure

helium and solar composition ($X \approx 0.7$) Eddington luminosities, given by

$$L_{\text{Edd}} = \frac{4\pi GMm_p c}{\sigma_T(1+X)}, \quad (3.1)$$

where M is the neutron star mass, σ_T is the Thomson scattering cross-section, m_p is the proton mass, and X is the mass fraction of ionized hydrogen (free protons). [Bult et al. \(2019\)](#) interpreted this as an observation of the rapid ejection of a solar or hydrogen-rich layer, followed by the usual helium PRE phase. This is consistent with the observed burst recurrence times and energetics which indicate that SAX J1808.4–3658 is in the burst regime where hydrogen is depleted by hot CNO burning well before unstable ignition of helium ([Galloway & Cumming 2006](#); [Goodwin et al. 2019](#)).

A similar idea for a two-staged mixed H/He PRE burst was put forward by [Sugimoto et al. \(1984\)](#) to explain the bursting behaviour of 4U/MXB 1636-53, which showed a bimodal distribution of peak luminosity (see also [Galloway et al. 2006](#)). Following this suggestion, [Kato \(1986\)](#) computed steady-state solutions of outflows from a small H layer on top of a He-layer, finding the timescale for the ejection of the H layer (and jump in luminosity) to be on the order of 0.1 to 1 s, inversely proportional to the luminosity of the model. However, this strongly depends on not only the mass of the H layer, assumed to be $10^{-16} M_\odot$, but also on the steady-state assumption, which cannot reproduce the actual ejection of the H layer. It is clear that in order to understand this type of burst, we need time-dependent hydrodynamic simulations combined with realistic neutron star envelopes.

X-ray bursts are challenging to model because of the many different types of physics involved. Previous studies have followed the time-dependent nuclear burning and convection during the thermonuclear runaway, using stellar evolution codes such

as KEPLER (Woosley et al. 2004; Cyburt et al. 2010), or Modules for Experiments in Stellar Astrophysics, MESA, (Paxton et al. 2011; Meisel 2018), but did not resolve the formation of the wind in PRE bursts. Yu & Weinberg (2018) first demonstrated the ability of MESA to resolve both the nuclear burning and convective mixing at the onset of bursts from pure He accretion, followed by the hydrodynamic ejection of a super-Eddington wind and the PRE phase. This opened up the possibility of simulating time-dependent PRE bursts with an emphasis on the role of composition in the resulting wind.

In this paper, we use MESA (version 15140; Paxton et al. 2011, 2013, 2015, 2018, 2019) to simulate the accumulation phase, ignition, super-Eddington wind, and decay of a mixed H/He PRE burst. This represents the first full simulation of PRE bursts resulting from accretion of H and He. Our main result is that the rise in luminosity at the start of the burst pauses temporarily once the luminosity reaches the Eddington luminosity. As a wind develops and mass is ejected, deeper layers are eventually exposed that have been depleted in hydrogen by a combination of convective mixing and nuclear burning. This ends the pause and the luminosity begins to rise again as the outflowing material becomes less hydrogen rich and therefore has a larger Eddington luminosity. The resulting lightcurve has a distinct shape in contrast to pure helium bursts, and it depends on the gradient of hydrogen left behind by convection. However, as we will show, these results are very sensitive to the treatment of convection within the code. Indeed, the entrainment of protons by convection from the H layer into the He burning zone below leads to short timescale nuclear burning, which feeds back into the convection. This is a regime that cannot be adequately simulated in one dimension, making the detailed shape of light curve uncertain.

We begin in Section 3.2 with a simple model of mixed H/He PRE bursts, and explain the connection between the hydrogen profile in the envelope post-convection and the shape of the lightcurve. The main stages and important parameters of this model are also summarized in Figure 3.1. In Section 3.3, we describe our MESA simulations and show detailed results using the simplest prescription for convection. In Section 3.4, we vary the prescription for convection and assess how the results are affected. In Section 3.5, we summarize our findings, elaborate on issues related to the treatment of convection in one-dimensional simulations, and give an interpretation for the SAX J1808.4–3658 data.

3.2 Evolution of the Composition Profile and Lightcurve Shape

The structure of the neutron star envelope at ignition is determined mainly by the accretion rate onto the neutron star and composition of the infalling gas. For $\dot{M}_{\text{acc}} \gtrsim 2 \times 10^{-10} M_{\odot} \text{ yr}^{-1}$, hydrogen burns via the hot CNO cycle at a constant rate (Bildsten 1998). Then, it can be shown that the column depth, $y(r) \equiv \int_{\infty}^r \rho(r') dr'$, at which hydrogen is depleted is

$$y_d = 2.7 \times 10^7 \text{ g cm}^{-2} \left(\frac{\dot{M}_{\text{acc}}}{0.01 \dot{M}_{\text{Edd}}} \right) \left(\frac{0.02}{Z_{\text{CNO}}} \right) \left(\frac{X_0}{0.7} \right) \quad (3.2)$$

where X_0 and Z_{CNO} are the initial hydrogen and CNO nuclei mass fractions (Cumming & Bildsten 2000)¹. We scale the accretion rate to the Eddington accretion rate

¹The expression for y_d from Cumming & Bildsten (2000) was re-evaluated for a 12 km radius and using a more accurate $E_{\text{H}} \approx 6.0 \times 10^{18} \text{ erg g}^{-1}$, instead of 6.4, to account for neutrino losses

corresponding to a neutron star with $R = 12$ km and accreted hydrogen mass fraction $X_0 = 0.7$, giving $\dot{M}_{\text{Edd}} = 8\pi R m_p c / (1 + X_0) \sigma_T = 2.1 \times 10^{-8} M_{\odot} \text{ yr}^{-1}$. Therefore at ignition, the envelope consists of two layers: an outer H-rich layer of depth y_d in which the hydrogen abundance drops from the accreted value to zero, and an inner layer of pure helium where ignition of the burst occurs. This initial state is illustrated in column A of Figure 3.1.

From an energetics standpoint, we know that only a column $y_w \sim 10^6\text{--}10^7 \text{ g cm}^{-2}$ can be ejected by winds (Weinberg et al. 2006), which is smaller than y_d . However, Weinberg et al. (2006) also showed that prior to the wind, a convection zone will grow and extend to a column smaller than y_w (Figure 3.1 column B), which will mix the H and He and result in a change in the composition of the ejecta as a function of time. We define the minimum column depth reached by convection as $y_{c,\min}$, below which hydrogen is not mixed and $X = X_0$ is roughly constant².

Wind models for PRE bursts (Ebisuzaki et al. 1983; Paczynski & Proszynski 1986; Joss & Melia 1987; Guichandut et al. 2021) show that the luminosity at infinity is always very close to the Eddington luminosity L_{Edd} (Equation (3.1)), as any “extra” energy in the form of a super-Eddington flux gets used up to drive mass-loss. Therefore, during the initial ejection of $y_{c,\min}$, $L \approx L_{\text{Edd}}$ will be constant. This is the

(Wallace & Woosley 1981).

² X in fact decreases linearly with y , but since $y_{c,\min}$ ends up being $\sim 1\%$ of y_d or less, the variation in X over this column is negligible.

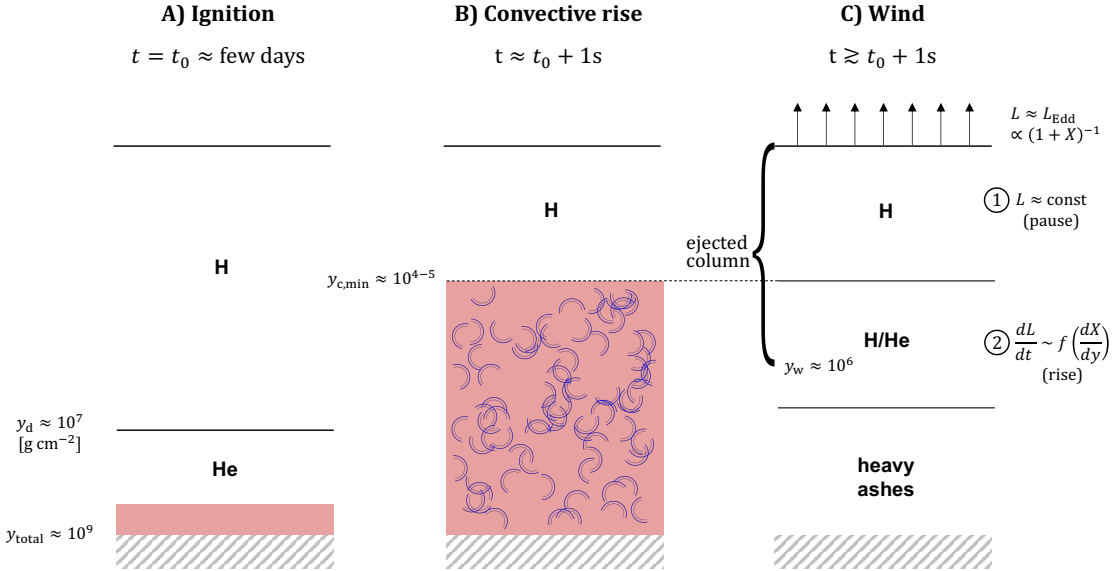


Figure 3.1: Diagram illustrating the three main stages of the mixed H/He burst. *A)* As hydrogen burns stably throughout accretion, distinct hydrogen and helium-rich layers build up in the envelope, their boundary being at a known column depth of y_d (Equation (3.2)). We are interested in bursts that ignite at $y > y_d$ (red color indicates nuclear burning). *B)* Heat from nuclear burning creates a growing convection zone (blue semicircles) which penetrates into the H-rich layer, resulting in additional nuclear burning. *C)* As the convection zone retreats, it leaves behind a layer of constant hydrogen fraction at a column $y_{c,\min} < y_d$, a mixed H-He layer and nuclear ashes at depth. Winds progressively eject the layers, up to a column $y_w > y_{c,\min}$, during which the observed luminosity at infinity is the Eddington luminosity, which depends on the hydrogen fraction X of the material. Since X is initially constant, we first observe a pause after the initial burst rise. After the H layer is ejected, the luminosity once again rises in a manner that depends on the hydrogen gradient dX/dy . See text for further details.

observed pause, and its duration is

$$\begin{aligned}\Delta t_p &\approx \frac{4\pi R^2 y_{c,\min}}{\dot{M}} \\ &\approx 0.18 \text{ s} \left(\frac{y_{c,\min}}{10^4 \text{ g cm}^{-2}} \right) \dot{M}_{18}^{-1},\end{aligned}\quad (3.3)$$

where $\dot{M}_{18} = \dot{M}/(10^{18} \text{ g s}^{-1})$ is the mass-loss rate, which we assume to be constant during the pause.

After the pause, the ejection of the mixed layers will begin, and the luminosity will rise as the hydrogen fraction X in the ejecta decreases. The rate dL/dt at which the luminosity will increase, assuming it stays near Eddington, will be proportional to $dX/dt \propto \dot{M}(dX/dy)$, thus linking the shape of the lightcurve to the hydrogen gradient in the envelope. Column C of Figure 3.1 illustrates the compositional nature of these two stages, the pause and the rise. Note that if $X = 0$ at columns $y < y_w$, a third stage will appear where the luminosity peaks at the helium L_{Edd} and remains there for the rest of the PRE (until all of y_w has been ejected).

The burst lightcurve is therefore determined by 1) the nuclear burning and convection that occur during the rising phase, setting the hydrogen profile, and 2) the mass-loss rate during the wind phase. In the next section, we describe simulations with **MESA** to investigate both of these factors.

3.3 MESA Simulations

We model a single burst with several separate **MESA** runs³, in an approach similar to [Yu & Weinberg \(2018\)](#). First, we follow the ignition and convective rise of the burst under the assumption of hydrostatic equilibrium, then use **MESA**'s hydrodynamic solver to follow the super-Eddington wind phase. However, unlike [Yu & Weinberg \(2018\)](#), we leave nuclear burning on during the wind, as much of the energy in bursts with hydrogen comes from slower reactions that continue into the wind phase.

³Our **MESA** inlists, models and simulation setup are available at <https://doi.org/10.5281/zenodo.8048553>.

3.3.1 Accumulation and formation of the layers

The basic physical setup is the same for all simulations: we assume a non-rotating neutron star of mass $M = 1.4 M_{\odot}$ and radius $R = 12$ km, and ignore general relativistic corrections. The envelope initially consists of an ^{56}Fe substrate⁴ with a column depth $y = 10^{11} \text{ g cm}^{-2}$. The outer boundary is initially set at an optical depth $\tau = 100$ to avoid numerical issues caused by radiation-dominated regions becoming convective (Paxton et al. 2013)⁵. We begin accreting a solar-like composition (^1H , ^4He and ^{12}C with mass fractions $X = 0.7$, $Y = 0.28$ and $Z = Z_{\text{CNO}} = 0.02$ respectively) at a constant rate of $\dot{M}_{\text{acc}} = 3 \times 10^{-10} M_{\odot} \text{ yr}^{-1} = 0.014 \dot{M}_{\text{Edd}}$. We assume carbon to be the only metal being accreted for simplicity. What matters for the ignition of this type of burst is to achieve hydrogen depletion, and any isotope part of the CNO cycle would work, because the CNO abundances quickly adjust to the equilibrium ratio of ^{14}O and ^{15}O in the hot CNO cycle (Bildsten 1998)⁶. Throughout accretion,

⁴To build the starting model, we took the the `ns_env` model file from the `ns_he` problem provided as part of `MESA`'s test suite, then relaxed the neutron star radius from 10 to 12 km, and finally accreted additional ^{56}Fe to the target column depth. The point of increasing the mass of the iron substrate is to build a large enough buffer between the flashing zone and the inner boundary, allowing heat to diffuse inward without reflecting back.

⁵In this first part of the simulation, the outer layers do not expand significantly and we mainly focus on the effects of convection at large depths. We later relax this outer boundary to a more appropriate value to model the wind and lightcurve (Section 3.3.3).

⁶We assume that all of the metallicity is in CNO elements. A more realistic solar composition would also contain non-CNO species, which would reduce the hot CNO burning rate. However, the change in the hydrogen depletion and ignition depths would be smaller than that associated with the uncertain accretion rate and crust heating parameter.

the luminosity at the base of the substrate is fixed to 1.8×10^{34} erg s $^{-1}$, equivalent to \dot{M}_{acc} times 1 MeV per nucleon which is roughly the expected crust heating at low accretion rates (Brown 2000). As discussed in Yu & Weinberg (2018), \dot{M}_{acc} and L_{base} determine the ignition depth, which we have chosen to be at $y \approx 3 \times 10^8$ g cm $^{-2}$, greater than y_d so that the burst ignites in a pure He layer.

To reduce the complexity of the computations, especially during the wind phase, we use MESA’s `cno_extras.net` nuclear network to model the nuclear burning, which includes 17 isotopes up to ^{24}Mg (we also add ^{56}Fe as an additional inert element). This is fewer and lighter isotopes than the `approx21.net` network used by Yu & Weinberg (2018) for He bursts (which has α -capture reactions up to iron-group elements), but contains a similar number of reactions due to the addition of hot CNO. It is also a much smaller network than that used by Woosley et al. (2004), who studied the energy generation carefully but did not model the hydrodynamic wind. Since we are focused primarily on the wind, this limited network is adequate because most of the energy generated during the burst comes from hydrogen and helium burning in CNO and triple- α reactions. However, this assumption means that our calculations do not accurately predict the nuclear burning ashes, both ejected in the wind and leftover afterward.

The left panel of Figure 3.2 shows the composition profile of the envelope after 5.9 days of accretion. The infalling CNO species convert to equilibrium oxygen ratios in under an hour. The hydrogen depletion column is $y_d = 3.7 \times 10^7$ g cm $^{-2}$, consistent with Equation (3.2) for the chosen \dot{M}_{acc} . At larger column depths, the CNO cycle is starved of protons, and the abundances are determined by β -decay rates only. Prior to ignition, some helium has already started stably burning and converting to ^{12}C .

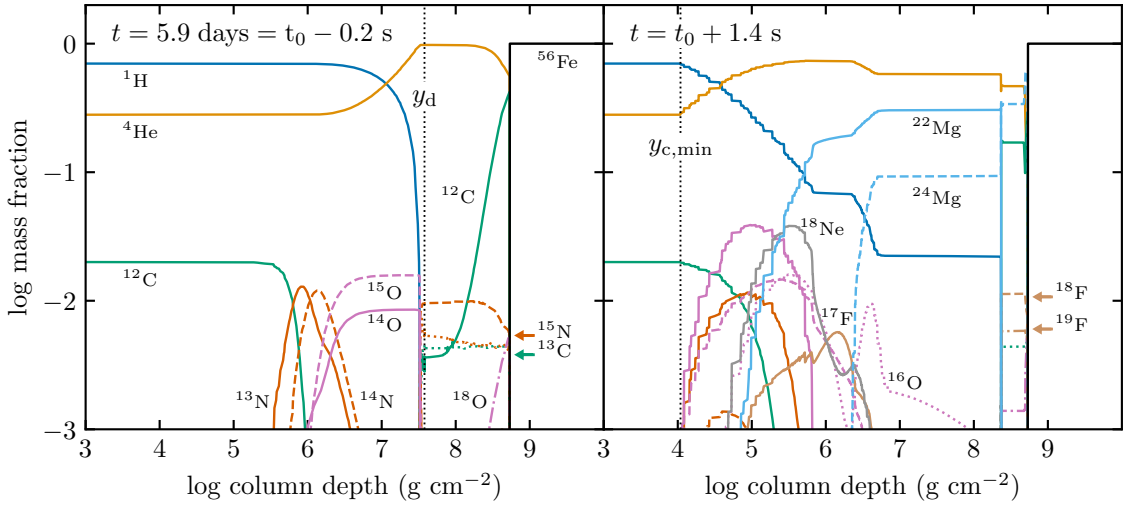


Figure 3.2: Composition profiles before (left) and after (right) the thermonuclear flash, which ignites at $t = t_0$. The lines for different elements have the same color in left and right panels. In the ~ 1.4 s to reach the Eddington luminosity, convection has significantly mixed the He and H layers. Dotted lines show the depletion column y_d (left) and the minimum extent of convection $y_{c,\min}$ (right). All runs shown in this paper begin at the ignited model $t = t_0$, which the left panel leads up to. The panel on the right shows the result of mixing using the Schwarzschild criterion prescription for convective boundaries (see Section 3.3.2).

3.3.2 Ignition and Convective Rise

After having built up the He layer, unstable triple- α burning triggers the thermonuclear runaway. We define “ignition” as the moment $t = t_0$ when the He layer is convective and has a larger maximum nuclear energy generation rate than the H layer. The convection zone begins growing in the He layer as it would in a pure He burst, then hits the H layer about 1.1s later. The mixing of H into the convection zone leads to a sudden increase in the nuclear energy generation rate at the top of the zone. The outcome of this mixing event depends strongly on the prescription used in the code for convection. Here, we use the prescription of [Heney et al. \(1965\)](#) for mixing length theory, with the dimensionless parameter $\alpha_{\text{mlt}} = 1.5$ dictating the

ratio between the mixing length and local pressure scale height. In this section, we present results using the Schwarzschild criterion to determine convective boundaries (as assumed also by [Yu & Weinberg 2018](#)). This ignores the effects of composition gradients on the convective stability, but simplifies the interpretation of our results. We explore the effect of changing the prescription for convection in Section 3.4.

In Figure 3.3, we show Kippenhahn diagrams for the history of convection and nuclear burning as a function of depth, throughout the flash phase and beginning of the wind. The bottom panel is zoomed in to show short timescales following the collision between the He convection zone and the H layer. In this collision, fresh protons are brought in below the depletion depth y_d where they can capture onto seed nuclei, causing a rapid injection of energy and a local steepening of the temperature gradient, which in turns drives further expansion of the convection zone. The first proton captures to happen are $^{18}\text{O}(\text{p}, \alpha)^{15}\text{N}$ and $^{15}\text{N}(\text{p}, \alpha)^{12}\text{C}$. The remaining protons (and fresh ones coming from the top) then quickly capture onto the carbon and build up ^{13}N . The nuclear reactions in this first stage do not produce enough heat to generate large scale convection. Instead, the convection splits into many zones, as radiative gaps as small as 0.1% of the scale height appear. These zones and gaps are clearly seen in the bottom panel of Figure 3.3. The maximum number of individual convective zones is 66, and it occurs 0.1 ms after the collision. The maximal extent of the convection during this initial stage is to a column $\approx 10^6 \text{ g cm}^{-2}$. We later refer to this stage as the *precursor*.

About 0.4 ms after the initial collision, enough nitrogen has built up to trigger a “second ignition” via the $^{13}\text{N}(\text{p}, \gamma)^{14}\text{O}$ reaction. This time, so much heat is released that the convection zone grows massively in less than 0.1 ms, its column depth extent

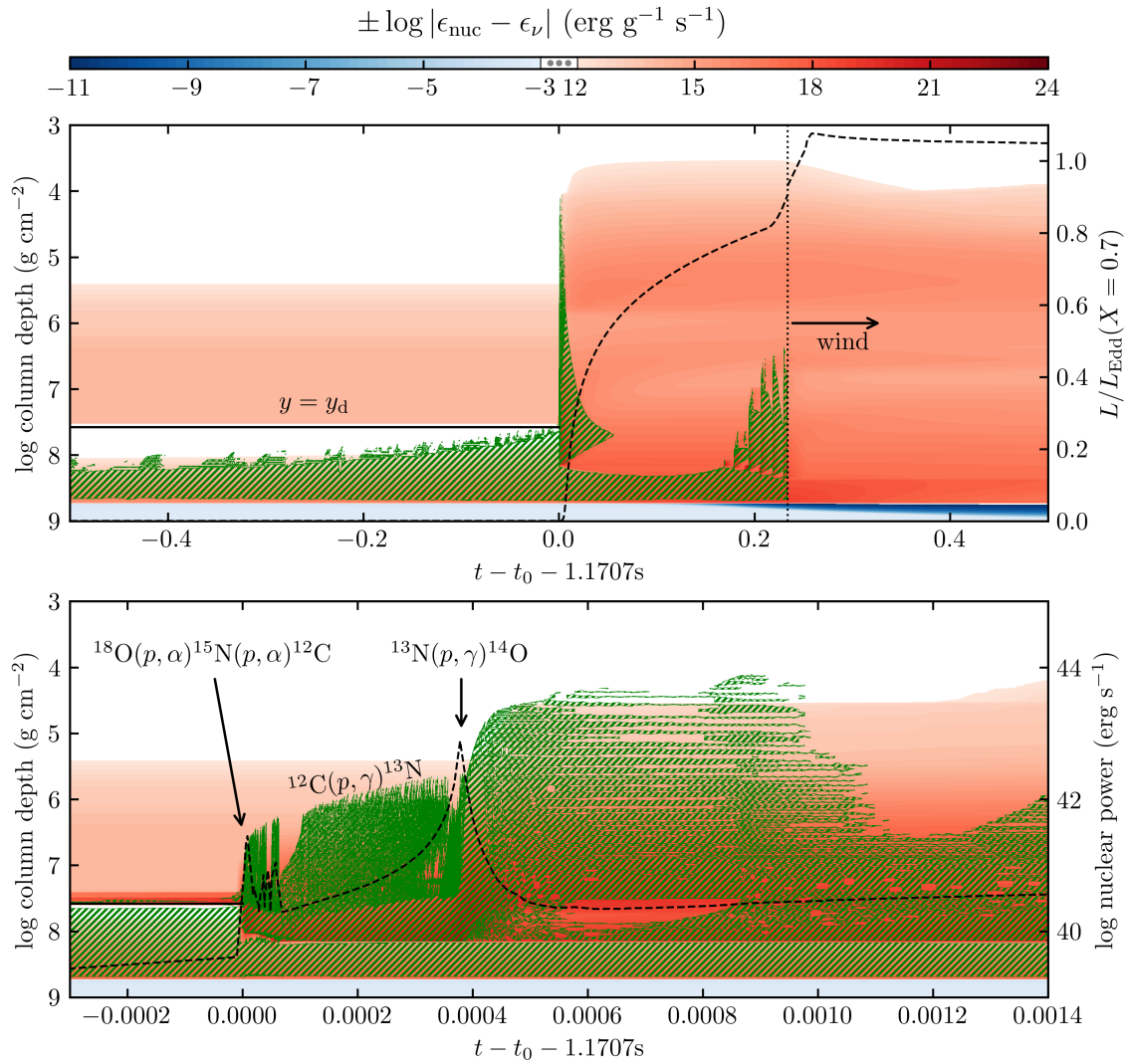


Figure 3.3: Kippenhahn diagrams for the Schwarzschild run, centered on the moment of collision between the convection zone and the H layer. The bottom panel is zoomed into a 1.5 ms window following the collision. The color scale traces the energy generation or loss (nuclear burning minus all neutrino losses), while the green hatches mark the convection zones. The solid black lines show the location of the depletion depth y_d . In the top panel, the dashed line shows the luminosity coming out of the atmosphere, normalized by the Eddington luminosity of the accreted gas (scale on the right-hand side). In the bottom panel, it shows the integrated nuclear power ($\int dm \epsilon_{\text{nuc}}$). Moments where certain reactions dominate are labeled (see Section 3.3.2).

decreasing by a factor of ≈ 30 . The convection is still split but the radiative gaps now maintain over time, resulting in a period of layered convection, which extends down to a minimum column $y_{c,\min} = 1.1 \times 10^4 \text{ g cm}^{-2}$. The remnants of this period of rapid burning appear in the final composition profiles (see e.g. the magenta and orange lines for ^{14}O and ^{13}N respectively in the right panel of Figure 3.2), and will later be partly ejected by the wind. Further oxygen, neon and finally sodium-burning reaches the end-point of our network at ^{24}Mg . The final composition profiles that go into the hydrodynamic calculation are shown in the right panel of Figure 3.2. If a more complete network were to be used, we would expect the ashes to proton and α capture to heavier elements, namely Ca and Si, over the following \sim tens of seconds ([Woosley et al. 2004](#)).

At the onset of both of these stages, the precursor and ^{13}N ignition, convective velocities on the order of 10^7 cm s^{-1} are generated, which allow for the overall convective envelope (disregarding gaps) to expand by meters in tens of microseconds. In most of the envelope, the large temperatures are such that these velocities remain well below the sound speed. However, in some convective zones, the local Mach number does reach up to $\sim 15\%$. This implies that the rapid burning is approaching a dynamical regime, but not so much as to make the hydrostatic assumption invalid. We return to the question of convective velocities in Section 3.4.

As we have explained in Section 3.2, the main predictor for the shape of the lightcurve is the hydrogen gradient left over by convection. We now investigate what creates this gradient. Figure 3.4 is another Kippenhahn diagram of the same simulation that shows the evolution of the hydrogen abundance after the collision. A few ms after the collision, once the convection retreats, the hydrogen gradient is already set.

The dashed line traces how much hydrogen has burned away since ignition. At the collision, a significant amount of protons capture onto seed nuclei, and this continues throughout the burst even as the convection zone retreats. At ignition, the total mass of the envelope (minus the iron substrate) is $\sim 10^{22}$ g, and $\sim 2\%$ of it is H. By the time the gradient is set, about 25% of the hydrogen has burned away (another 10% burns in the rest of the flash, mostly at depths $y > y_w$, before ejection by winds). What is important in determining the gradient is not the details of the nuclear burning; once convection subsides, hydrogen burning at shallow depths (near $y_{c,\min}$) is slow and does not substantially affect the gradient and therefore the lightcurve. Instead, it is the efficiency of the convective mixing which determines how fast and how far protons can be brought downward to regions of high temperatures where they can quickly burn away. We further investigate the point about the efficiency of mixing in Section 3.4.

3.3.3 Wind and Collapse

As the outgoing luminosity rises and approaches the Eddington limit a short time after ignition, the outer layers become radiation pressure dominated and the envelope begins to expand. In Newtonian gravity, we know from previous work that appreciable expansion of ~ 100 m above the stellar surface occurs at $\approx 90\%$ of L_{Edd} (see Figure 12 of [Guichandut et al. 2021](#)). At this point, we turn off convection⁷ and accretion, turn on MESA’s hydrodynamics calculation, and relax the outer boundary to an optical depth

⁷This is done to avoid complications associated with radiation-dominated artificially becoming convective.

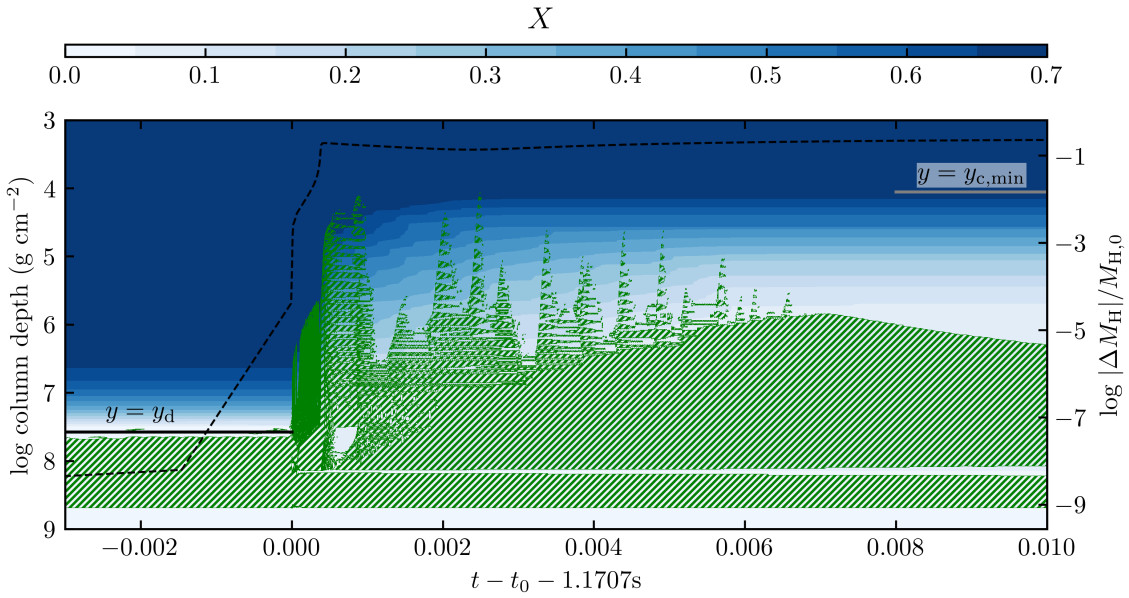


Figure 3.4: Kippenhahn diagram for the Schwarzschild run as in Figure 3.3, now with the color scale representing the hydrogen abundance. The solid black and gray lines show y_d and $y_{c,\min}$ (same values as in Figure 3.2). The dashed line shows the relative change in the total mass of hydrogen at a given time compared to the initial amount at ignition (scale on the right-hand side).

$\tau = 2/3$ in order to resolve the photosphere, as in [Yu & Weinberg \(2018\)](#). Mass-loss is then done by removing any grid points with a density $\rho < \rho_{\text{thresh}} = 10^{-7} \text{ g cm}^{-3}$. To avoid issues caused by going off the opacity tables at low density, we switch to an interpolation formula for electron scattering opacity as a function of temperature from [Paczynski \(1983\)](#). This is a good approximation at the high temperatures of the wind where electron scattering dominates.

The presence of jumps in the ${}^1\text{H}$ mass fractions as a result of convection (see right panel of Figure 3.2) added some numerical difficulties in the simulation of the winds. Since the acceleration of a fluid parcel due to radiation is proportional to its opacity, a jump in the hydrogen fraction X will result in a density inversion, as the uppermost fluid element is ejected faster than the bottom one can follow. We found

that these density inversions tended to expand as they moved outward, and caused the MESA integration to diverge as they approached ρ_{thresh} . A solution that worked in all cases was to manually soften those composition jumps using a smoothing spline on the ${}^1\text{H}$ mass fractions prior to running the wind simulation, as shown in the top panel of Figure 3.6. In order to preserve the overall gradient, this smoothing was done using monotonic functions. The ${}^4\text{He}$ profiles were then adjusted such that the sum of mass fractions of all species remained 1 everywhere.

During the wind, the rate of change of composition in the atmosphere is determined by the mass-loss rate

$$\dot{M}(r, t) = 4\pi r^2 \rho(r, t) v(r, t), \quad (3.4)$$

where ρ and v are the gas density and velocity at a radial distance r from the center of the star. We evaluated \dot{M} at three different locations: a) the “sonic point”, i.e. where the velocity $v = \sqrt{kT/\mu m_p}$ where μ is the mean molecular weight of the gas, b) the photosphere, i.e. the location $r = r_{\text{ph}}$ where the luminosity $L = 4\pi r_{\text{ph}}^2 \sigma T^4$, and c) the surface of the model or outer boundary of the grid. As shown in Figure 3.5, despite some small variations, the mass-loss rate is overall constant across all locations. This is no surprise, as we expect these winds to reach a steady-state, characterized by a constant $\dot{M}(r)$ at fixed t , in a time much shorter than the evolution timescale of the burst ([Joss & Melia 1987](#); [Guichandut et al. 2021](#)). We can then write the total column ejected as a function of time,

$$y_{\text{ej}}(t) = \frac{1}{4\pi R^2} \int_0^t \dot{M}(t') dt', \quad (3.5)$$

independently of location. The total ejected column y_{w} is the final value of y_{ej} , equal to $5.83 \times 10^5 \text{ g cm}^{-2}$ in this simulation (see dashed line in Figure 3.5). This is roughly

consistent with results obtained by [Yu & Weinberg \(2018\)](#) for the total ejected mass of pure He bursts igniting at a similar column depth as we have here. As shown by these authors, the total ejected column, and therefore the total duration of the PRE, would increase (decrease) for bursts which ignite at larger (smaller) column depths.

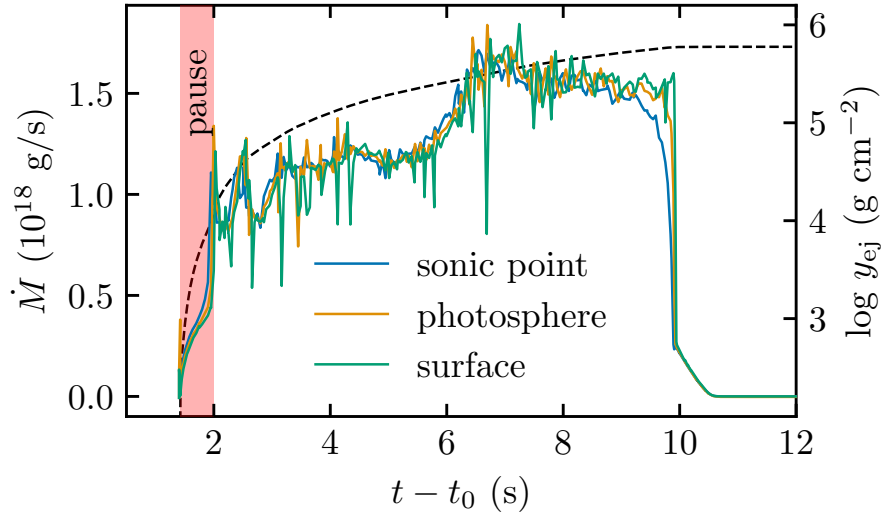


Figure 3.5: The mass-loss rate of the wind as a function of time for the Schwarzschild run, in solid lines. The different colors show \dot{M} evaluated with Equation (3.4) at different locations (see text). The dashed lines show the ejected column y_{ej} (scale on the right-hand side). The red shaded region marks the pause in the lightcurve (bottom panel of Figure 3.6).

Approaching the end of the super-Eddington phase of the burst, the nuclear luminosity which is driving the wind begins to die down. The outflow then separates into two regions, an outer unbound wind of high velocity which is being ejected, and an inner atmosphere which is collapsing back into, eventually, a hydrostatic configuration. This can be seen from Figure 3.5 at $t - t_0 > 9$ s, where the mass-loss rate first drops sequentially from the inside (lower radii first). The timescale for the collapse to reach the surface from the sonic point is $\lesssim 1$ s, which is roughly the sound crossing time between those two locations ([Guichandut et al. 2021](#)). In some other

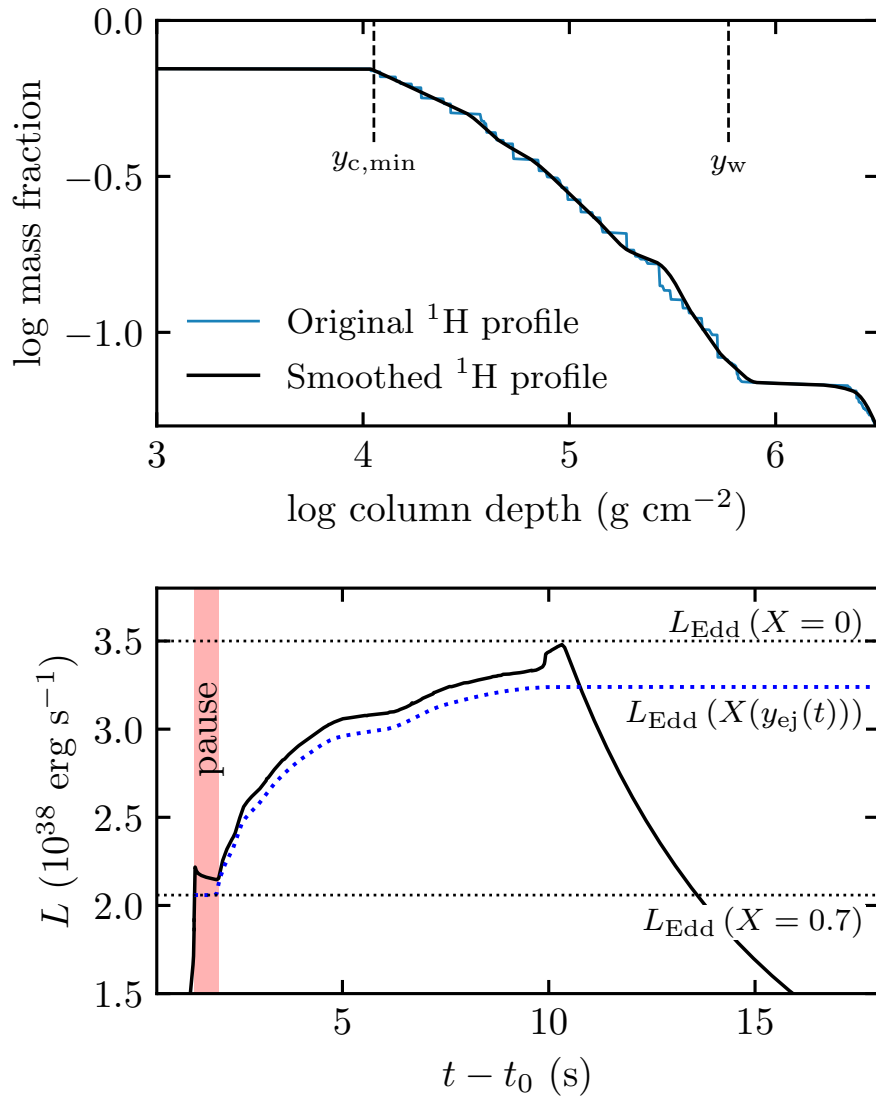


Figure 3.6: Results of the Schwarzschild run. *Top:* Hydrogen profile after convective mixing. To avoid numerical difficulties during the hydrodynamic wind (see Section 3.3.3), the profile was smoothed using a monotonic cubic spline. The dashed lines show the minimum column reached by convection $y_{c,\min}$, and the total column ejected by winds y_w . *Bottom:* Lightcurve of the burst. The pause occurs after surpassing L_{Edd} of the accreted material ($X = 0.7$, bottom dotted line). The following rise takes place over a much longer timescale since $y_w \gg y_{c,\min}$. In general, the outgoing luminosity follows the Eddington luminosity of the material which is currently being ejected (blue dotted line), which we can track using $y_{\text{ej}}(t)$ (see Section 3.3.4).

simulations (Section 3.4), the collapse results in numerical issues as the infalling gas becomes supersonic, which causes the time-step to drop and the evolution of the model to come to a stop. The moment where these numerical issues arise coincides with the sonic point crossing the photosphere and the wind effectively becoming optically thin. Then, the implicit optically thick assumption made by MESA to treat the radiative transfer becomes incorrect. Future work is needed to investigate the infall phase in more detail.

3.3.4 Lightcurve

In order to plot the observed lightcurve, we evaluate the radiative luminosity of our models as a function of time at the photosphere. We show the lightcurve for the main Schwarzschild run in the bottom panel of Figure 3.6. Its shape is consistent with the hydrogen profile in the envelope post-convection, shown in the top panel. On the luminosity axis, the ratio between the peak and pause luminosities is ≈ 1.6 , consistent with the ratio of Eddington luminosities $(1 + X_0)/(1 + X(y_w))$ with $X(y_w) = 0.07$ (Figure 3.6 top panel). On the time axis, we also have to take into account how the mass-loss rate varies throughout the burst. The pause duration is 0.6 s which, for $y_{c,\min} = 1.1 \times 10^4 \text{ g cm}^{-2}$, corresponds to a mass-loss rate $\dot{M}_{18} = 0.33$ according to Equation (3.3). This is in good agreement with the time-averaged value of \dot{M} during the pause, $3.5 \times 10^{17} \text{ g s}^{-1}$ (note however that \dot{M} changes significantly during the pause, from $\approx 6.5 \times 10^{16} \text{ g s}^{-1}$ to $\approx 7.6 \times 10^{17} \text{ g s}^{-1}$, see Figure 3.5). If the mass-loss rate remained at this value throughout the remainder of the wind, the total duration of the PRE phase would be $(y_w/y_{c,\min})\Delta t_{\text{pause}} \approx 32 \text{ s}$. But since \dot{M} increases by a

factor of ~ 3 after the pause (Figure 3.5), the ejection is much faster and the PRE only lasts ≈ 9 s.

As expected, the lightcurve can be obtained by tracking L_{Edd} as the hydrogen mass fraction in the ejecta $X(y_{\text{ej}}(t))$ evolves in time. This is shown by the blue dotted line in Figure 3.6 which closely follows the luminosity from the simulation (black line). Comparing the two, we see that two features of the observed lightcurve are unexplained by composition changes. First, the luminosity during the pause is not exactly flat, but instead slowly decreases throughout its duration. This effect can be understood by considering the energetics of the expansion. At the beginning of the pause, the wind is not yet established. To do so, it needs to both lift material out of the gravitational potential and expand it (effectively raising its enthalpy). These two contributions account for the observed decrease in luminosity⁸. Second, near the end of the super-Eddington phase and before the decay, a bump in luminosity appears. This is related to the wind dying down, which “returns” the gravitational energy and enthalpy that was required to sustain it back to the radiation. However, as discussed in the previous section, this part of the lightcurve is uncertain because of the wind becoming optically thin.

From the observational perspective, it could in principle be possible to infer the shape of the hydrogen profile from the lightcurve only. Assuming that the energy used to eject mass (GMM_{w}/R where $M_{\text{w}} = 4\pi R^2 y_{\text{w}}$) is equal to a fraction η of

⁸Note that this effect is not related to the pause itself but rather to the onset of the wind, when L first exceeds L_{Edd} , and should therefore be a common feature across all PRE bursts. In fact, all lightcurves of pure He bursts in [Yu & Weinberg \(2018\)](#) (see their Figure 12) also show a slowly descending flux throughout the wind, which can likely be attributed to the same effect.

the observed burst energy (integrated luminosity which can be determined from the fluence if the distance to the source is known), one could infer y_w from the lightcurve only. Then, given the total duration of the PRE, one could find the average \dot{M} , and finally use Equation (3.3) to obtain $y_{c,\min}$. In our simulations, we find $\eta \approx 0.31 - 0.37$, but this is likely to change for different ignition depths. We plan to study the energy budget of PRE bursts in more detail in future work.

3.4 Impact of Changing the Treatment of Convection

It is unlikely that the implementation of convection in Section 3.3 with the Schwarzschild criterion is an accurate representation of the true hydrodynamic phenomena. For one, the rapid nuclear burning induces local changes in composition toward heavier species, and locally increases the mean molecular weight μ . The creation of μ -gradients can either have a stabilizing or de-stabilizing effect on the thermal profile. This is especially relevant starting at the collision, where the growth of the He-rich convection zone will be inhibited by the H-rich material on top, as pointed out by [Weinberg et al. \(2006\)](#). They showed that a jump in temperature between the convection zone and the overlying radiative layer would develop in order to overcome the stabilization of the boundary due to composition. However, the effectiveness of the composition jump may be decreased by entrainment of fluid at the convective-radiative boundary which would erode the stabilizing composition gradient (e.g. [Anders et al. 2022](#)). Second, we may expect that the tiny radiative gaps

that appear in between convection zones (see Section 3.3.2) will be destroyed by some form of overshoot mixing. This is because, at the Schwarzschild convective boundary, the fluid parcel has zero acceleration by definition, but it may have enough inertia to continue rising and mix the fluid all the way to the next convective zone.

To better understand the importance of these effects, we ran additional simulations, starting from the same model at ignition (Figure 3.2, left panel), but changing the prescription for convection during the thermonuclear flash. We first ran a simulation using the Ledoux criterion instead of Schwarzschild for locating convective boundaries, which takes into account compositional gradients. When this is used, semiconvective and thermohaline mixing become available. For these, we set the dimensionless parameters $\alpha_{\text{sc}} = 0.1$, and $\alpha_{\text{th}} = 2$ (`MESA` uses these to determine diffusion coefficients, see [Paxton et al. 2013](#)), following the `ns_he` test suite problem in `MESA`. Then, we ran simulations using both the Schwarzschild and Ledoux criteria where we also forced all radiative gaps of radial extent less than 10% of the scale height to close and become convective instead⁹. This is meant to, in a simplified way, mimic the overshoot at the top of each convective zone. Finally, we tested the convergence of our simulations by running a high resolution version of every prescription. For these, the number of grid points during the flash phase was increased from ~ 5000 to ~ 15000 (the exact number varies in time and is adjusted by `MESA` using the

⁹To implement this, we used `MESA`'s existing optional routine (activated with the `min_convective_gap` control), but added an option to set a minimum pressure for the routine to operate, which we set to the pressure of the top of the iron substrate in order to prevent “accidental” undershoot mixing with the iron. These additions are provided with the package linked in footnote 3.

`mesh_delta_coeff` control).

We show in Figure 3.7 the hydrogen composition profiles and lightcurves for all the simulations mentioned above. In each case, the main two features of our simplified model hold: 1) a larger $y_{c,\min}$ results in a longer pause, and 2) a steeper hydrogen gradient leads to a faster rise in luminosity. The peak luminosity of the burst is then inversely proportional to $X(y_w)$, where $y_w \lesssim 10^6 \text{ g cm}^{-2}$ is roughly constant across different bursts, and reaches the helium L_{Edd} in half of the simulations. Moreover, lightcurves with higher peak luminosities have shorter PRE times – this is because the fluence is conserved for a given ignition depth, no matter the exact shape of the lightcurve. The slow decrease of the luminosity during the pause is also observed in every case. For runs which managed to integrate through the decay phase (ones which do not end in an “x” in Figure 3.7), the bump at the end of the super-Eddington phase is also present. Once y_w has been completely ejected, all models join on the same exponential cooling track.

While Figure 3.7 demonstrates agreement with the basic model described in Section 3.2, it also clearly shows that the results, and in particular the observable lightcurve, depend on the prescription for convection. We cannot confidently claim that one prescription is more realistic than another, given the complex interactions between nuclear burning and mixing in this inherently multi-dimensional process, and so cannot predict lightcurves using these simulations. Nevertheless, we can assess the impact that different convective prescriptions have on the overall simulation. First, using the Ledoux criterion instead of the Schwarzschild criterion means that formerly convective regions become semi-convective instead, as the composition gradients stabilize the thermal profile. This effect inhibits the mixing, and, therefore

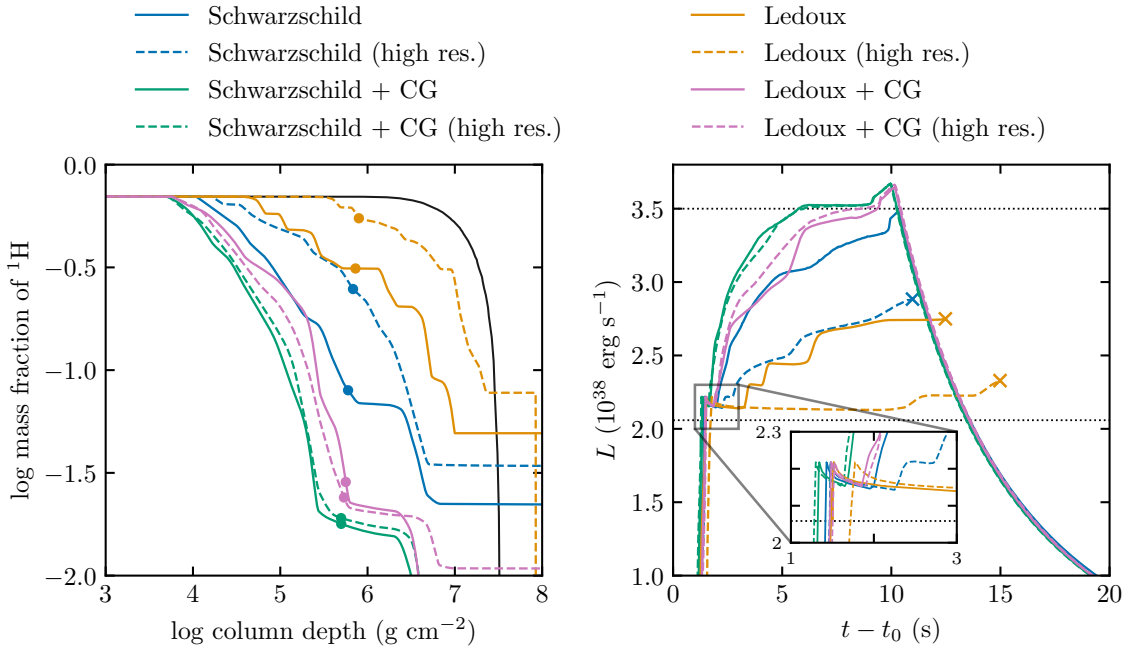


Figure 3.7: Results for all convective prescriptions and spatial resolutions tested in this work. *Left:* Mass fraction of ${}^1\text{H}$ in the atmosphere after the convective rise and before the ejection by winds. The circles label the locations of y_w resulting from each simulations. The black line shows the hydrogen gradient at ignition, from which all runs start. *Right:* Lightcurve of the bursts. The dotted lines mark the locations of L_{Edd} for $X = 0.7$ and $X = 0$, as in Figure 3.6. Some simulations could not integrate through the decay phase and were stopped short at the “x” symbols. The inset zooms in on the pauses.

(Section 3.3.2), reduces the amount of hydrogen burned away. This can be seen in the left panel of Figure 3.7 by comparing the orange and blue lines. Closing the radiative gaps between convective zones (“CG” in the figure legend) naturally has the opposite effect, with the mixing becoming stronger. The impact of spatial resolution is also interesting (compare solid and dashed lines in Figure 3.7). In the Schwarzschild and Ledoux runs, we obtain an increase in the total number of convective zones when increasing the resolution. Indeed, the addition of grid points in the convection zone allows it to split even more. Therefore, these runs are clearly not converged. How-

ever, in the CG runs, this splitting is effectively cancelled, as tiny zones are merged together at the end of every step, and we find good agreement between the models with different resolutions.

Another aspect to consider is the criterion for locating convective boundaries. In the presence of composition discontinuities, as is the case in our simulations, simplified applications of the Schwarzschild or Ledoux criteria can lead to unphysical scenarios and ultimately impede the growth of convective zones (see [Gabriel et al. 2014](#) for an extensive discussion). In [Paxton et al. \(2018\)](#), an optional “predictive mixing” scheme was implemented in `MESA` to address this issue. This algorithm iteratively tests if the convective boundary is still correctly located once the material becomes fully mixed on the convective side, applying corrections otherwise. This may not be accurate in our situation where mixing also leads to rapid burning¹⁰. Nonetheless, we ran some exploratory simulations of the flash including predictive mixing. The results were very similar in all cases, except when using the Ledoux criterion without closing gaps. Then, the hydrogen abundances were reduced (mixing was enhanced) compared to the original model without predictive mixing, but not all the way to the models with the Schwarzschild criterion.

Finally, as mentioned in section 3.3.2, we found some large convective velocities resulting from the rapid nuclear burning, implying a departure from a hydrostatic envelope. We also find similar velocities in the other simulations presented in this section. However, the usual implementation of mixing-length theory does not factor

¹⁰For this same reason, the “convective premixing” scheme implemented in [Paxton et al. \(2019\)](#), which works by iteratively instantaneously mixing and changing abundances in the cells surrounding the boundary, could not be used here.

in the time required to accelerate to these velocities. To explore this, we evaluated the timescale for convective acceleration at any given step n , given by [Wood \(1974\)](#) as $\tau_a \sim \ell/(v_c^n + v_c^{n+1})$, where ℓ is the mixing length and v_c is the convective velocity. If the actual timestep taken by the code $\Delta t = t^{n+1} - t^n$ is shorter than τ_a , then velocities have increased too quickly. In our simulations, we found a few instances where $\Delta t/\tau_a \sim 10^{-3}$, but only during the precursor phase. This casts doubt on the existence and behaviour of this precursor. Alternatively, MESA has the option to enable acceleration-limited convection ([Paxton et al. 2015](#)). The most recent version also includes a more complete theory of time-dependent convection ([Jermyn et al. 2023](#)) which will also limit accelerations. However, our attempts at running simulations with either option were unfruitful, with the evolution eventually being driven to prohibitively short timesteps in trying to converge. Getting these models to converge and reach Eddington is a potential avenue for future work, as they are likely the most accurate way to model convection with rapid burning while remaining in one dimension.

3.5 Summary and Discussion

We have shown that variations in chemical composition in the envelope of neutron stars accreting mixed H/He fuel are reflected in the lightcurves of their PRE bursts. After the ignition of the thermonuclear runaway in the He-rich layer, a convective zone expands outward and mixes the fuel with the overlying H-rich shell (Figure 3.2). The resulting H abundance profile determines the shape of the lightcurve, namely the duration of initial pause and the subsequent slope in luminosity (Figure 3.6).

Due to convection, the mass of the layer with solar composition, $y_{c,\min} \sim 10^4 - 10^5$ g cm $^{-2}$, is much reduced compared to the initial $y_d \sim 10^7$ g cm $^{-2}$ set by stable hydrogen burning during accretion (Equation (3.2)). This results in a rapid ejection of a hydrogen-rich shell and a short observed pause on the order of 1 s or less (Equation (3.3)). Subsequently, the luminosity rises toward the helium Eddington luminosity as hydrogen depleted layers are exposed by the wind.

We find that the hydrogen profile in the envelope is sensitive to the details of convection and mixing following the collision with the H layer (Figures 3.3 and 3.4). As a result, the exact shape of the lightcurve of a given event is uncertain as it depends on the choice of convective prescription and spatial resolution (Figure 3.7). The critical factor in setting the hydrogen profile is the efficiency of the mixing within the convective regions. However, this mixing is inhibited when the convection splits into many zones interspersed with radiative gaps. This splitting occurs even when ignoring compositional gradients (Schwarzschild criterion), suggesting that the culprit is the local energy deposition from rapid nuclear burning. Moreover, we found that increasing the spatial resolution of the simulations led to an increase in the number of zones and gaps, significantly reducing the efficiency of mixing, such that our simulations are not converged. This non-convergence however is mitigated by overshoot mixing at the top of convective zones, which we modeled in a simplified way by closing radiative gaps less than 10% of the scale height.

Even disregarding problems related to splitting of the convection, a more fundamental issue stems from the approximate treatment of convection with mixing-length theory. In the collision event, nuclear burning releases energy on tens of microsecond timescales, which is close to or even shorter than local convective turnover times. This

is in violation of the standard assumptions of mixing length theory. It also amplifies the differences between the Schwarzschild and Ledoux criterion, in contrast to situations with long dynamical timescales such as the main-sequence, where both criteria should lead to similar outcomes (Anders et al. 2022), although we did find that an improved implementation of convective boundaries using predictive-mixing brought Ledoux closer to Schwarzschild. This timescale problem has been noted before in the context of late-stage evolution of massive population III stars. There, a helium burning convective region encroaches upon a hydrogen shell, mixing in protons which burn on timescales of hours to days, which is short compared to the month-long convective turnover times (Marigo et al. 2001). The proper modeling of these situations, which are also known as level-3 mixing or convective-reactive phases (Herwig et al. 2011), continues to be an active area of research (e.g. Davis et al. 2019; Clarkson & Herwig 2021), with a particular focus on multidimensional hydrodynamics simulations (Woodward et al. 2014; Stephens et al. 2021).

Although the general shape of the lightcurves in our simulations agrees with the burst from SAX J1808.4–3658 reported by Bult et al. (2019), there are some differences. In the observed burst, the pause is ~ 0.7 s long, similar to our principal Schwarzschild run, suggesting a similar extent of the convection. However, the subsequent rise is rapid, reaching the helium Eddington luminosity in just ~ 1.3 s. This would imply a mixing event which is strong enough to produce a very steep hydrogen gradient. Since the total pause plus rise duration is ~ 3 times that of the pause, the hydrogen profile would have to go from¹¹ $X \approx 0.7$ to $X = 0$ in the span

¹¹Goodwin et al. (2019) inferred a hydrogen mass-fraction $X_0 \approx 0.57_{-0.14}^{+0.13}$ for the companion, based on an analysis of Type I X-ray burst recurrence times and energetics. The observed ratio of

of $y_{c,\min} \approx 10^4$ g cm $^{-2}$ to $\approx 3 y_{c,\min}$. Or, if for example the mass-loss rate increases by a factor of 3 from the pause to the rise, as it does in our simulations (Section 3.3.3), then in the span of $y_{c,\min}$ to $\approx 9 y_{c,\min}$; in any case, the whole hydrogen gradient spans a decade in column depth at most. None of our simulations achieve this – our fastest rise time is $\gtrsim 6$ s for the Schwarzschild+CG model (in fact, factoring redshift, these times should be $\sim 20 - 30\%$ longer). Moreover, our Figure 3.7 shows a general trend that steep hydrogen gradients are also associated with smaller $y_{c,\min}$ values; to reproduce the rise seen in SAX J1808.4–3658, we may need such strong mixing that it would push $y_{c,\min}$ to very small columns and dissolve the pause entirely.

One way to match the rapid rise but keep the pause duration the same as observed in SAX J1808.4–3658 could be to burn hydrogen more effectively with the same mixing efficiency and convective extent. In fact, our simulations do not model hydrogen burning completely, because we were limited to a small nuclear network which reached its end at ^{24}Mg prior to the wind launch (see right panel of Figure 3.2). We investigated the effect of a larger network by running a simulation equivalent to our Schwarzschild run, but using MESA’s `rp_153.net` nuclear network, which includes isotopes up to ^{56}Ni , until the wind launch. We found that the outer hydrogen profile was unchanged, with $y_{c,\min}$ and initial hydrogen gradient staying the same. The effects of the additional hydrogen burning were limited to large columns $\gtrsim 0.3y_w$. At these depths, hydrogen completely burned away, whereas with the smaller network a small amount ($\lesssim 0.1$ for the well-mixed models) remains. The lightcurve for such a burst would initially look the same as in our original Schwarzschild run (Figure 3.6 bottom

peak to pause luminosities in [Bult et al. \(2019\)](#) favors the upper end of this range.

panel), but would continue rising all the way to the helium Eddington luminosity, instead of levelling off to $\sim 90\%$ of it. This suggests that additional burning is not the explanation for the rapid rise after the pause.

More observations of PRE bursts in the pure helium ignition regime would help to further understand and constrain the hydrogen ejection model. Note that previous PRE bursts from SAX J1808.4–3658, observed with the Rossi X-ray Timing Explorer, have shown an increase in luminosity during the Eddington phase, but only by $\sim 20\%$ and on ~ 7 s timescales (see Figure 3 in [Galloway et al. 2017](#)). In these bursts, pauses are not clearly seen, which would indicate small values of $y_{c,\min}$, although this could also be due to the choice of time bins used for the analysis. Such variations in the shape of the lightcurve (slow or fast luminosity increases) across different bursts from a single source may also imply that the dynamics of convection are very sensitive to initial conditions at ignition. Furthermore, a puzzling aspect of the burst reported in [Bult et al. \(2019\)](#) is the secondary peak following the PRE phase. This is unexplained by our hydrogen ejection model, and could instead require multidimensional effects.

On the theoretical side, the obvious next step in order to refine predictions for these bursts will be to improve the treatment of convection during the thermonuclear flash, in particular for the collision between the He and H layers. Due to the timescales involved and the limitations of mixing length theory, we know that only multidimensional hydrodynamical simulations can yield accurate results. This may pose a significant numerical challenge, although recent works by [Malone et al. \(2014\)](#) and [Zingale et al. \(2015\)](#) have shown promising results in this direction, demonstrating the use of low Mach number hydrodynamics to model two and three-dimensional convection in thermonuclear explosions.

Finally, other improvements need also be made in the hydrodynamical part of the simulation in order to correctly model the super-Eddington wind. First, we faced numerical problems with “staircases” in mass fractions leading to density inversions in the wind, which we simply smoothed out in this work. It would be interesting to investigate such density inversions as they propagate outward in future work. We also had issues at the end of the super-Eddington phase and collapse of the atmosphere. To properly model this part of the PRE, we will likely need hydrodynamical simulations which can handle optically thin radiative transfer as well as shocks (if our findings that infall velocities can be supersonic are correct). Hydrodynamical simulations would also be useful to model the super-Eddington winds in multiple dimensions, where the effects of rotation and magnetic fields could be taken into account. Lastly, for accurate observational predictions, it would be pertinent to include general relativistic corrections to the hydrodynamic equations, as they are known to result in larger photospheric radii ([Paczynski & Proszynski 1986](#); [Guichandut et al. 2021](#)).

We thank Alexander Heger for helpful discussions on convective-reactive mixing. We also thank Hang Yu for sharing results and analysis of his 2018 paper, and Rob Farmer for guidance on the `MESA` source code. Finally, we thank the anonymous referee for helpful comments that improved this manuscript. S.G. is supported by an NSERC scholarship. This work was supported by NSERC Discovery Grant RGPIN-2017-04780. SG and AC are members of the Centre de Recherche en Astrophysique du Québec (CRAQ). Simulations were ran on the Graham cluster, operated by the Digital Research Alliance of Canada.

Software: This work made use of the Python libraries *NumPy* ([Harris et al. 2020](#)), *SciPy* ([Virtanen et al. 2020](#)), and *Matplotlib* ([Hunter 2007](#)). The `py_mesa_reader` package ([Wolf & Schwab 2017](#)) was used for MESA output files.

From 1D to 2D

After successfully presenting a mechanism to produce pauses, but being unable to produce a predictive model due to uncertainties in the treatment of convection, the road ahead was clear. We needed to study this problem with hydrodynamics. What would the “collision” look like when following the actual fluid?

At Stony Brook University, Mike Zingale’s group has been developing a suite of codes to simulate reactive flows, with many astrophysical applications ranging from massive star convection, to Type Ia supernovae, to X-ray bursts. Our burst was the perfect occasion to utilize the new low Mach number code **MAESTROeX**.

I headed to Long Island to work with Mike for a few months, running simulations with hundreds of cpu cores on the Perlmutter cluster. We discovered that the growth of the convection zone was due to a more subtle mechanism than previously thought. We also found that the “explosiveness” of the collision heavily depended on the pre-burst carbon abundances.

These calculations lay the foundation for what we should really study in the future, which is a 3D fully compressible evolution of these bursts.

Chapter 4

Hydrodynamical Simulations of Proton Ingestion Flashes in Type I X-ray Bursts

*This thesis chapter originally appeared in the literature as
Guichandut, Zingale and Cumming 2024, *The Astrophysical Journal (ApJ)*,
975, 250. <https://doi.org/10.3847/1538-4357/ad81f7>*

Authors

Simon Guichandut¹, Michael Zingale², Andrew Cumming¹

¹Department of Physics and Trottier Space Institute, McGill University, 3600 rue University, Montreal, QC, H3A 2T8, Canada

²Department of Physics and Astronomy, Stony Brook University, NY 11794-3800, USA

Abstract

We perform the first multidimensional fluid simulations of thermonuclear helium ignition underneath a hydrogen-rich shell. This situation is relevant to Type I X-ray bursts on neutron stars that accrete from a hydrogen-rich companion. Using the low-Mach number fluid code **MAESTROeX**, we investigate the growth of the convection zone due to nuclear burning, and the evolution of the chemical abundances in the atmosphere of the star. We also examine the convective boundary mixing processes that cause the evolution to differ significantly from previous one-dimensional simulations that rely on mixing-length theory. We find that the convection zone grows outward as penetrating fluid elements cool the overlying radiative layer, rather than directly from the increasing entropy of the convection zone itself. Simultaneously, these flows efficiently mix composition, carrying carbon out of and protons into the convection zone even before contact with the hydrogen shell. We discuss the implications of these effects for future modeling of these events and observations.

4.1 Introduction

Type I X-ray bursts are the result of thermonuclear runaways on the surface of accreting neutron stars in low-mass X-ray binaries (Lewin et al. 1993; Galloway & Keek 2021; Strohmayer & Bildsten 2006). As the most frequent transient in the high-energy sky with over 7000 bursts cataloged (Galloway et al. 2020), these “bursts” can help us understand the properties of the neutron star surface. The challenge is to properly model the physics of nuclear burning, fluid motions, radiation, and their interaction.

A critical mechanism that controls the evolution of these bursts is convection. Even though ignition happens only a few tens of meters below the star’s surface, the density of the envelope is so large that the fluid cannot cool by radiation only. The burning fuel will therefore generate a convection zone that will grow toward the surface in a time shorter than the thermal time. Many studies have described this convection zone and its evolution. Joss (1977) derived the basic timescales for radiation and convection, and showed that convection could not reach all the way to the photosphere. Initial time-dependent calculations made the simplifying assumption that regions unstable to convection are perfectly adiabatic and instantaneously mix entropy (Joss 1978; Hanawa & Sugimoto 1982). Many simulations of bursts were performed using stellar evolution codes such as KEPLER (Wallace et al. 1982; Woosley et al. 2004), SHIVA (José et al. 2010), and MESA (Paxton et al. 2011; Yu & Weinberg 2018). These codes have in common that they treat convection with some variation of mixing-length theory (MLT, e.g. Cox & Giuli 1968; Henyey et al. 1965), in which it is assumed that convective parcels travel a fixed fraction of the local pressure scale height, at the velocity required to transport the heat flux.

Meanwhile, few studies have been dedicated to modeling the multidimensional hydrodynamic nature of convection within bursts. Numerically, this is a challenge of timescales. Burning and convection take place over many scale heights, and one therefore needs to account for the compressibility of the fluid. This introduces sound waves into the system, which travel on a sound crossing time of $\sim 10 \mu\text{s}$, much shorter than the tens of seconds burst duration, and the computational cost of the simulations easily becomes prohibitive. But since bursts proceed as subsonic deflagrations (Wallace et al. 1982), an alternative approach is to model the fluid in the low-Mach number approximation (see Almgren et al. 2006b, and references therein for the origins of this method). This was first applied to X-ray bursts by Lin et al. (2006) who performed two-dimensional (2D) simulations of a pure helium-burning layer and growing convection zone, and confirmed that the Mach number remained small ($\lesssim 15\%$) throughout, justifying the use of the low-Mach method. Malone et al. (2011) used the dedicated low-Mach number hydrodynamics code **MAESTRO** (Nonaka et al. 2010) to model a similar type of burst. Malone et al. (2014) then modeled a burst from a uniform mixture of hydrogen and helium, a more common scenario for accreting neutron stars in bursting sources. Both works found that a very high spatial resolution (few centimeters per zone or even less, depending on the temperature sensitivity of the nuclear reactions) was needed to obtain numerical convergence.

Another possibility for the composition of the envelope prior to the outburst is a layered structure, where a hydrogen-rich shell sits on top of a pure helium layer. In sources where the neutron star is accreting solar-like material (primarily H with mass fraction $X_0 \sim 0.7$, then He, and some CNO elements with Z_{CNO} of a few percent), at high enough accretion rates \dot{M}_{acc} such that the temperature T exceeds $8 \times 10^7 \text{ K}$,

hydrogen will continuously burn via the hot CNO cycle, and run out at the depletion depth

$$y_d = 2.7 \times 10^7 \text{ g cm}^{-2} \left(\frac{\dot{M}_{\text{acc}}}{0.01 \dot{M}_{\text{Edd}}} \right) \left(\frac{0.02}{Z_{\text{CNO}}} \right) \left(\frac{X_0}{0.7} \right), \quad (4.1)$$

as shown by Cumming & Bildsten (2000). Here \dot{M}_{Edd} is the Eddington accretion rate for a neutron star with a 12 km radius accreting gas with $X_0 = 0.7$. The column depth $y(r) \equiv \int_r^\infty \rho(r') dr'$ measures the amount of mass above a radial coordinate r .

Recently, in Guichandut & Cumming (2023), we suggested that the lightcurves of bursts which ignite at $y > y_d$ could be used to test the radial extent of the convection zone. In particular, we showed that the peculiar observation of a ≈ 0.7 s pause in the rise of a burst from SAX J1808.4–3658 (Bult et al. 2019) was consistent with the ejection of a hydrogen shell. For the pause to be so short, this shell would have had to be eroded by convection. We ran one-dimensional calculations using the stellar evolution code MESA (Paxton et al. 2011) and verified that convection could indeed extend to the required column depths of $y_{\text{conv}} \sim 10^4 - 10^5 \text{ g cm}^{-2} \ll y_d$. However, our results were sensitive to assumptions made about convection in the code. One reason for this is that MLT is not appropriate for situations where the thermodynamics of the gas are changing on timescales similar to the convective turnover time. In these bursts, a convection zone in the helium layer will grow and eventually “collide” with the hydrogen-rich shell above, which will introduce new fuel in the form of free protons which quickly burn and rapidly change the nature of the convection. This is an example of a “proton-ingestion flash”, which also occur for example in evolved metal poor stars (see e.g. Herwig et al. 2011, and references therein). The limitations of MLT have been noted for these events as well, and recent works have instead focused on fluid simulations (Herwig et al. 2014).

To understand how convection proceeds in X-ray bursts with proton-ingestion events, we must model the multidimensional fluid. In this paper, we use the low-Mach number hydrodynamics code `MAESTROeX` (the successor to `MAESTRO`; [Fan et al. 2019](#)) to evolve the same burst which we previously studied in [Guichandut & Cumming \(2023\)](#). As in [Malone et al. \(2011, 2014\)](#), we consider a 2D box in the plane-parallel neutron star atmosphere on the verge of thermonuclear ignition. We briefly describe the numerical method and how our initial model is created in Section 4.2, and present the results of the simulations in Section 4.3. We conclude in Section 4.4.

4.2 Methodology

4.2.1 Numerical Method

The basic idea of the low-Mach number method is to decompose the pressure into base-state plus perturbative components,

$$p = p(\mathbf{x}) = p_0(r) + \pi(\mathbf{x}), \quad (4.2)$$

where \mathbf{x} is the cartesian position vector and r is the radial coordinate in the star. The base state is assumed to be in hydrostatic equilibrium, i.e.

$$\nabla p_0 = -\rho_0 g \hat{\mathbf{r}}, \quad (4.3)$$

where $\rho_0(r)$ is the base state density. It can be shown ([Almgren et al. 2006b](#)) that if the Mach number $\mathcal{M} = |\mathbf{U}|/c_s$ (c_s being the local speed of sound) is small, then the pressure perturbations π/p_0 are of order \mathcal{M}^2 . Thus, we can ignore π in linking the pressure to the density via the equation of state, which effectively decouples the two

and filters out sound waves. For full details on the equations being solved and the algorithmic implementation, see [Fan et al. \(2019\)](#).

As in previous papers using `MAESTRO` to model bursts, we use the Helmholtz equation of state ([Timmes & Swesty 2000](#)), which has pressure contributions from ideal gas, radiation, and degenerate electrons. Our reaction network is equivalent to `MESA`’s “CNO_extras” network ([Paxton et al. 2011](#)), with inert ^{56}Fe added. The complete set of reactions linking 20 isotopes from ^1H to ^{24}Mg is assembled using `pynucastro` ([Smith Clark et al. 2023](#)).

4.2.2 Initial Model

As in [Malone et al. \(2014\)](#), we create an initial model based on a 1D stellar evolution calculation, in this case our previous `MESA` study of this type of burst in [Guichandut & Cumming \(2023\)](#). There, we considered a neutron star with a mass of $1.4M_{\odot}$, radius 12 km, and surface gravity of $1.29 \times 10^{14} \text{ cm s}^{-2}$ (ignoring relativistic corrections). We first accreted a large column of inert iron to form the bottom of the atmosphere, then let it accrete a solar mixture of fuel (^1H , ^4He and ^{12}C with mass fractions $X = 0.7$, $Y = 0.28$ and $Z = 0.02$) until ignition. This `MESA` model is plotted with dash-dotted lines in Figure 4.1, in terms of its temperature and composition.

In practice, it is difficult to directly port a `MESA` model to a fluid simulation code, because the former’s grid is by mass coordinate while the latter is spatial, and due to small differences in the equation of state of both codes. This is why we instead opt to construct a toy model which is defined by a small set of physical parameters.

The full description of our model is presented in Appendix 4.5. Briefly, our

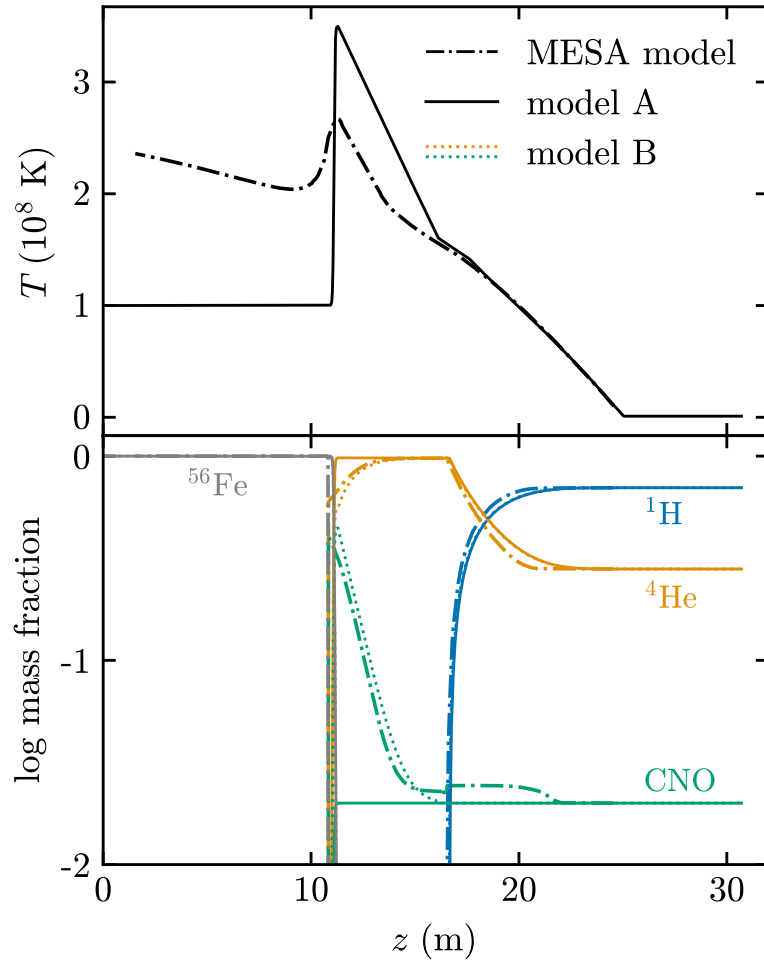


Figure 4.1: Initial model from MESA (dash-dotted lines), and the initial model A fed into the fluid simulations (solid lines). The top panel shows the temperature profile as a function of height. The bottom panel shows the composition profiles of the main chemical species, where the green color combines all CNO species. The offset in the position of the solar layer is due to the temperature kick given to the initial fluid model. An alternate initial model (model B) including deep carbon is shown in the dotted lines for CNO and helium mass fractions. See Appendix 4.5 for details.

atmosphere is composed of solar-like fuel at the top, then pure helium and CNO past the hydrogen depletion depth, then pure iron. At the bottom of the fuel layer (just above the iron) is an isentropic zone which becomes convectively unstable once the simulation begins. The temperature profile above is in radiative equilibrium, and

depends on the flux from nuclear burning. We set the temperature of the iron layer to an artificially small value so as to create a “buoyancy wall” that suppresses downward penetrating flows and inhibits mixing of the iron into the fuel above. Lastly, we “kick” the model by increasing the temperature of the isentropic zone in order to accelerate the evolution toward the thermonuclear runaway. This “model A” is shown with solid lines in Figure 4.1.

This model is simpler than the **MESA** model in two main aspects. First, we assume that the initial CNO species are ^{14}O and ^{15}O only. This is valid for $y < y_d$ where hot CNO burning is taking place and the rate-limiting step is the oxygen β -decays. (Indeed, our **MESA** simulations confirmed that most of the accreting CNO converts to oxygen before hitting the depletion depth). However, for $y < y_d$, there are no more protons to sustain the reactions and the oxygens should decay to ^{15}N , ^{14}N , then ^{13}C products (see Figure 2 in [Guichandut & Cumming 2023](#)). We do not expect this simplification to affect the results because these species only represent a few percent of the mass of the fuel, and because burning is initially dominated by triple- α , and then by its products, as we will see later.

Second, we start in a state where the helium is fully unburned, whereas in reality, over the course of days of accretion and stable burning, some of the helium would have already converted to ^{12}C . This carbon becomes the dominant CNO species in the helium layer, reaching a peak mass fraction of ≈ 0.4 at the bottom (see Figure 4.1). To investigate the impact that this carbon has on the burst evolution, we create an alternate initial model, “model B”, with the same temperature profile but with a similar total mass of carbon as the **MESA** model. The adjusted carbon and helium mass fractions for this other model are shown with dotted lines in the bottom panel

of Figure 4.1.

As in [Malone et al. \(2014\)](#), we configure a “sponge” region at the top of the model. Below a density $\rho = \rho_{\text{cutoff}} = 10^3 \text{ g cm}^{-3}$, we hold the density constant. Within this region, **MAESTROeX** solves the anelastic velocity constraint, which effectively suppresses large spurious velocities which would otherwise make the calculation diverge. The sponge initially starts at $z \approx 22 \text{ m}$, but moves upward, following the density, as the atmosphere expands during the burst.

4.3 Results

We ran simulations, starting from the initial model presented in the last section, at resolutions of 12, 6, 3 and 1.5 cm per zone. The grid is square with a width of 3072 cm. This being much less than the radius of the star, the atmosphere is effectively plane-parallel, with a constant gravity $g = 1.29 \times 10^{14} \text{ cm}^2 \text{ s}^{-1}$. The boundary conditions are periodic on the sides, outflow at the top, and slip wall (vanishing vertical velocity and tangential velocity gradient) at the bottom of the box. The density and enthalpy are held constant at the bottom and at the top. We do not include thermal diffusion as it is much slower than heat transport via convection at the depths we are considering¹.

In Section 4.3.1, we compare the general evolution of the different simulations and discuss convergence. In Section 4.3.2 we consider a single simulation to analyze

¹[Malone et al. \(2011\)](#) showed that thermal diffusion only had minor effects on the evolution of convection, which is what we are focusing on. We also verified that the thermal diffusion timescales were long ($\sim 0.1 \text{ s}$ or more) for the largest temperature gradients found in our simulations.

the evolution of convection and burning throughout the burst. In Section 4.3.3, we delve into the details of the mixing near the convective boundary. These three sections all consider model A. In Section 4.3.4, we look at a simulation of a more explosive version of this burst using model B.

4.3.1 Resolution Dependence and Convergence

In order to assess convergence, we plot the instantaneous maximum values in the grid of the temperature and Mach number in Figure 4.2. Both peaks are tracers of the evolution of the burst in time. The temperature curve clearly shows a transition from a slow increase to a full runaway. As we will see later, this transition is related to the collision of the convection zone with the overlying hydrogen-rich shell.

The evolution of the burst in time clearly depends on the resolution. At greater resolutions (smaller grid spacings), the burst evolves faster. A few factors contribute to this, which were previously observed and discussed in [Malone et al. \(2011\)](#) and [Malone et al. \(2014\)](#). First, since the nuclear burning is very sensitive to temperature, under-resolving the peak of the temperature profile will underestimate the energy generation. Second, lower resolution results in spurious large velocities which overshoot the convection zone, taking heat away from it and inhibiting its growth. In our case, this second factor is particularly important as convection is needed to bring additional fuel into the mixture.

The simulations appear to converge at a grid spacing of 3 cm, as decreasing it to 1.5 cm does not significantly change the evolution. For comparison, [Malone et al. \(2011\)](#) obtained convergence at a resolution of 0.5 cm; however, the X-ray burst under

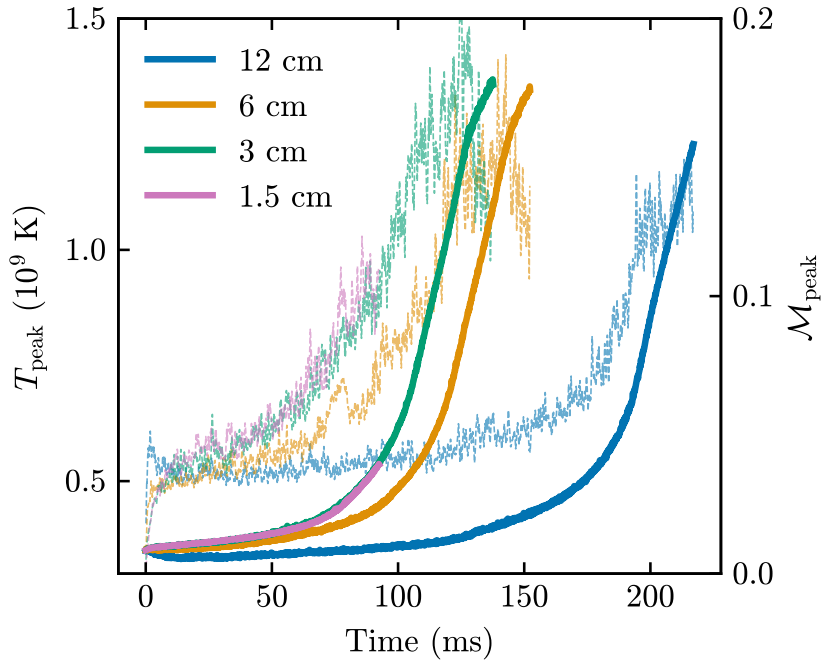


Figure 4.2: Peak values of the temperature (left axis, solid lines) and mach number (right axis, dashed lines) as a function of time for the same burst at different resolutions.

study had different initial conditions (notably a much larger initial temperature). Despite convergence demonstrating the robustness of the **MAESTROeX** calculations, our simulations do reach appreciable fractions of the mach number ($\gtrsim 15\%$). Shortly thereafter, the calculation becomes unstable, and the simulations stop. At this point, the thermonuclear runaway is still underway and the flux has not had time to escape the atmosphere. Therefore, the full evolution of Type I X-ray bursts in the low-Mach approximation remains intractable. We discuss this problem further in Section 4.4.

4.3.2 Evolution of Convection

We now look in depth at the evolution of the 3 cm model. We identify three “special” times for the three stages which we explore in this section. In Figure 4.3, we plot snapshots of the fluid at these times in terms of its vorticity, nuclear burning, hydrogen and carbon mass fractions.

Growth in the He layer. We first start the simulation by applying a gaussian random noise perturbation of 1 part in 1000 to every temperature in the grid. This triggers initial flows, which rapidly merge into a convective region in the initial isentropic zone. In the top-left panel of Figure 4.3, convection can be seen by the presence of large vortices, a distinct feature of 2D convection. These vortices travel up and down the convective region, entrained by the greater overturning convective motions. With convective velocities of $\sim \text{km s}^{-1}$, the convective turnover times at this point are on the order of milliseconds. Burning is initially confined to the bottom of the convection zone. Triple- α reactions convert helium into carbon and release heat into the convective region, causing it to expand. After ~ 10 ms, carbon becomes fully mixed in the convective region, uniformly increasing in mass-fraction as helium burns.

In Figure 4.4, we show the evolution of the temperature profile². Throughout this initial evolution, the temperature gradient of the convection zone remains adiabatic ($\nabla \equiv d \ln T / d \ln p$ is close to ∇_{ad} , as indicated in the figure). As a result, the top of the convection zone is roughly located at the intersection between this gradient and the initial radiative profile (but not exactly, as we will discuss in Section 4.3.3).

²Note that here and in upcoming figures, the profiles of a quantity with depth are obtained via horizontal averaging

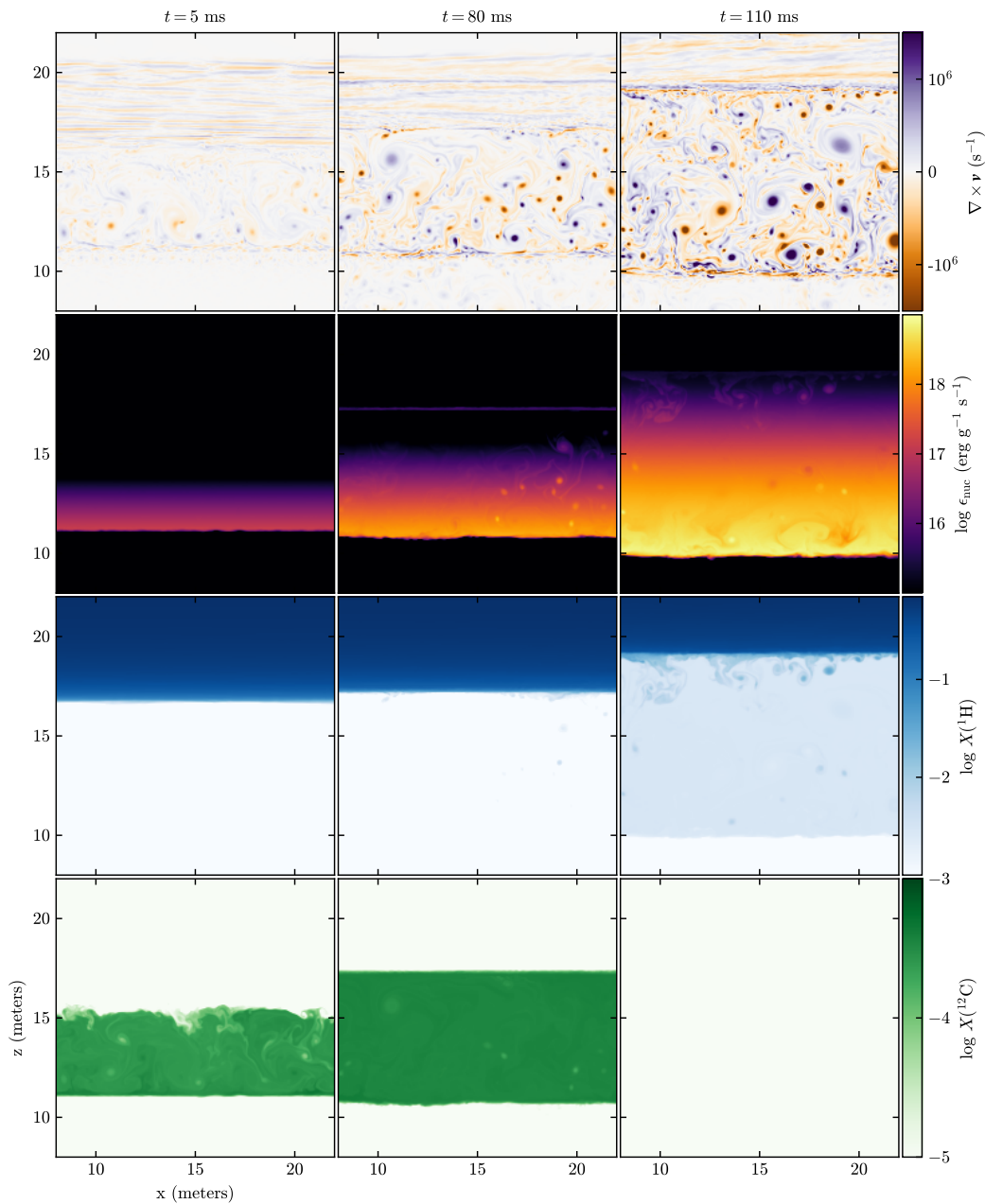


Figure 4.3: Flow, burning, and composition at different times in the 3 cm MAESTROeX simulation of model A. From top to bottom: vorticity, burning rate, mass fraction of hydrogen, mass fraction of carbon. Note the different scales in the bottom two rows. The left column is during the initial growth of the convection zone in the helium layer, the middle column is roughly at the collision with the hydrogen layer, and the right column is later during the expansion into the hydrogen. An animated version of this figure is available in the online journal.

Because the convection zone and overlying stable He zone have similar mean molecular weights, the Schwarzschild and Ledoux³ criteria agree on the location of the convective boundary, which can be seen in Figure 4.4 with the square and circle markers lying on top of each other.

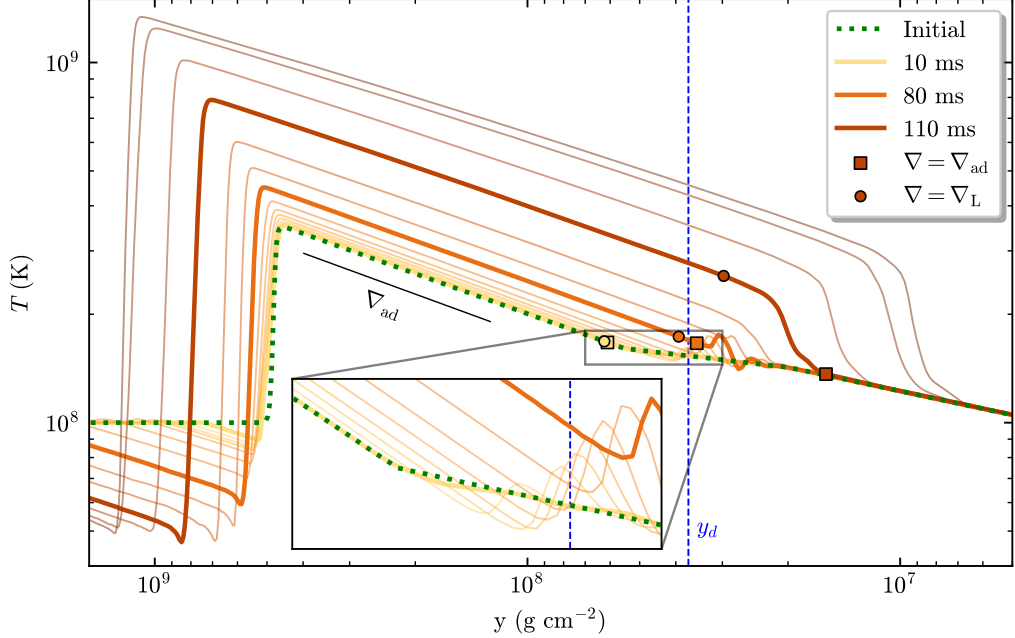


Figure 4.4: Evolution of the temperature as a function of column depth (note that the x-axis is reversed), at intervals of 10 ms. The colors get darker as time increases. The labeled and thicker lines are the three times from Figure 4.3. The circle and square markers show the convective boundaries according to the Schwarzschild and Ledoux criteria respectively. The vertical dotted line is the depletion depth, i.e. the depth of the hydrogen layer. As convection approaches this line, the Schwarzschild and Ledoux boundaries begin to separate. The inset zooms into the evolution near the hydrogen boundary.

Collision with the H shell. After about 50 ms, overshooting motions above the convective boundary reach y_d , the hydrogen depletion depth (Equation (4.1)). This is the beginning of the event which we have dubbed the “collision”. The second column

³We evaluate the Ledoux gradient ∇_L as in **MESA**, see Section 3.3 of [Paxton et al. \(2013\)](#).

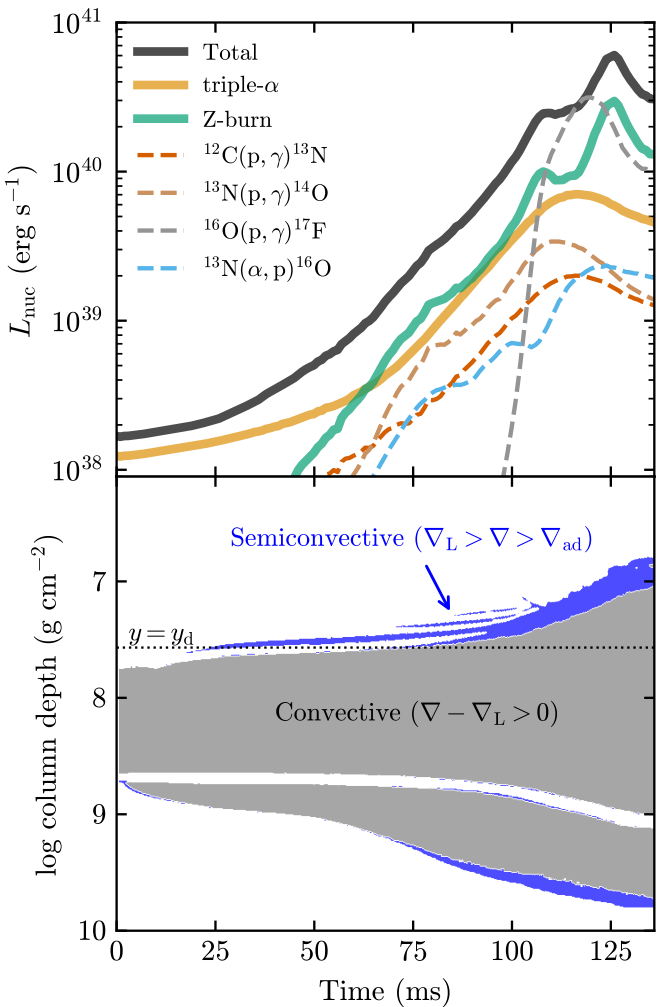


Figure 4.5: *Top:* evolution of the nuclear luminosity (Equation (4.4)) with time, for helium-burning and metal burning reactions (including CNO), and the total. The production of the most important CNO rates is plotted in dashed lines. *Bottom:* size of the convective and semiconvective regions as a function of time. The dotted line shows the depletion depth.

of Figure 4.3 shows the state of the fluid 30 ms later, once the convection zone has fully crossed $y = y_d$. In the collision, fresh fuel in the form of free protons becomes available and triggers CNO burning. A thin burning layer appears at y_d where protons are captured onto ^{12}C previously made from helium burning, and then onto the fresh ^{13}N . The protons that do not burn at this boundary are able to travel deeper into the convection zone, but not very far because the temperature is so high. Even though carbon is burning away at the boundary, more is being supplied by helium burning below, and mixing remains efficient enough such that the carbon fraction is uniform

throughout the convective region.

With the addition of protons into the mix, CNO burning overtakes helium-burning as the main energy source. One way to track the total energy production in the grid, using horizontally averaged quantities, is with the “nuclear luminosity”,

$$L_{\text{nuc}}(t) = 4\pi R^2 \int_z \epsilon_{\text{nuc}}(z', t) \rho(z', t) dz' , \quad (4.4)$$

where the integral is performed over the vertical direction in the grid. This quantity gives the total energy produced by the burst, at all depths, per unit time⁴. We plot L_{nuc} in the top panel of Figure 4.5. We see that after 50 ms, protons initially capture onto ^{12}C to produce ^{13}N , which subsequently burns either via proton or α -capture. Burning to heavier species such as ^{17}F begins ~ 50 ms later. This sequence of reactions is very similar to what we have previously obtained in 1D simulations. However, this onset of CNO burning is much weaker than in 1D. This is because the carbon mass fraction at the moment of collision is only $\approx 10^{-3}$, about 100 times smaller than in our MESA simulations. With our initial model, carbon can only come from the tens of milliseconds of helium burning since the start of the simulation, whereas the MESA model already has a significant amount of carbon at ignition (Section 4.2.2). Due to the limited CNO burning, the convection zone keeps expanding upward in a smooth fashion, albeit at an accelerated rate. This is shown in the bottom panel of Figure 4.5.

Growth into the H shell. Later, as the convection zone, which is becoming richer in heavy elements, keeps growing into the hydrogen-rich shell, it does so fighting

⁴The actual radiative luminosity coming out of the atmosphere during the burst is much smaller, both because of the thermal time to the surface, and because much of the energy will get used to drive mass loss.

against a buoyancy barrier. At this stage, composition gradients start playing an important role in setting the convective boundary. This can be seen in Figure 4.4 with the Ledoux and Schwarzschild boundaries becoming separate. In order to grow, the convection zone has to “wait” until it is hot enough that it is buoyant in the light material above. Therefore, a strong temperature gradient develops at the convective boundary. This was predicted by [Weinberg et al. \(2006\)](#). The material in this gradient region is thermally unstable, but overall convectively stable due to the composition gradient. These are the right conditions for semiconvection to develop ([Kippenhahn et al. 2012](#)), shown as the blue regions in the bottom panel of Figure 4.5. To model this type of mixing accurately would require following thermal diffusion and also diffusive mixing of species, which **MAESTR0eX** does not include. Note however that we do not expect either thermal diffusion nor semiconvection to prevent the existence of this sharp temperature gradient. The diffusion coefficient for radiation is $4acT^3/(3\kappa\rho^2c_p) \sim (10^3 \text{ cm}^2 \text{ s}^{-1}) T_8^3/\rho_5^2$, and thus thermal time over the $\sim 10 \text{ cm}$ gradient is $\sim 0.1 \text{ s}$. The diffusion coefficient for semiconvection is similar or even smaller by a factor of up to 1000 ([Langer 1991](#)).

During this period, the flow is dominated by large vortices (see top right panel of Figure 4.3), which is a consequence of the inverse energy cascade of 2D turbulence. Such large vortices are not present in three-dimensional (3D) simulations of X-ray bursts ([Zingale et al. 2015](#)). Interestingly, these vortices appear to carry within them a larger amount of hydrogen than the surrounding mean flow, and are therefore burning at a faster rate than the horizontal mean. Whether the presence of large vortices meaningfully affects the transport of hydrogen and therefore the depth at which burning is taking place is a question which can only be answered by 3D simulations

using the same setup. We leave this to future work.

Toward the end of the simulation, carbon and nitrogen have been fully converted to heavier elements, and are no longer available to capture protons, which are still inflowing from the top. The main proton-capture reaction happening at this point, $^{16}\text{O}(p, \gamma)^{17}\text{F}$, is competing with its photodisintegration inverse. As a result, an equilibrium mass fraction of $\sim 10^{-3}$ of hydrogen is left behind, which is seen in the third row of Figure 4.3. We note however that this is likely just an effect of the limited size of our network—these protons would in reality find other avenues to burn.

Throughout the simulation, a secondary convection zone has been developing in the iron substrate underneath the burning layer, as can be clearly seen in the bottom panel of Figure 4.5. This is the convective *undershoot* problem, previously noted by [Malone et al. \(2011\)](#), where down currents in the convective region are able to penetrate the stable layer despite opposing buoyancy (which was even artificially enhanced by setting the temperature of the iron substrate to a small value, Section 4.2.2). Chemical mixing between the layers occurs, in which helium and carbon are brought down and a large amount of iron gets dredged up into the burning layer (up to a mass fraction of $\sim 50\%$ toward the end of the simulation), which inhibits the burning. We discuss the validity and potential observational consequences of this undershoot in Section 4.4.

Finally, we remark that gravity waves in the stable region are being excited by convection. They can be seen in the vorticity panels of Figure 4.3 (and more clearly in the animated figure). It would be interesting to characterize these waves and their spectrum, but it is beyond the scope of this present study.

4.3.3 Convective Boundary Mixing

In [Guichandut & Cumming \(2023\)](#), the interaction between the convection zone and stable layer at the moment of collision caused an explosive transient with convective velocities at the boundary suddenly increasing, and the convection zone itself extending by many scale heights in the space of a few microseconds. It was unclear if these effects were numerical artifacts, caused by the approximate treatment of convection in the regime of rapid heating. This convective-reactive interaction is an example of a convective boundary mixing process, which are an active area of research (see [Anders & Pedersen 2023](#) for a recent review). Now, we have the necessary fluid simulations to describe what really happens at the top of the convection zone.

Starting with a simple question: How does the convection zone (CZ) grow into the radiative zone (RZ)? The simplest model goes as follows: at any point in time, convection is restricted to the adiabatic region, whereas the RZ above is unchanging. Therefore, the way to move the convective boundary upward is by raising the adiabat of the CZ, i.e. increasing its entropy. This is of course accomplished by nuclear reactions which release heat into the mixture. As such, the convective boundary is always located at the intersection between the initial entropy profile of the radiative zone, $s_{RZ,0}$ ⁵, and the *current* entropy of the convection zone, $s_{CZ} = s_{CZ,0} + \Delta s_{\text{nuc}}$. This is well illustrated in Figure 4 of [Hanawa & Sugimoto \(1982\)](#).

It turns out that this simple picture is not at all what is happening in our simulations. Surprisingly, we find that the specific entropy of the CZ is in fact slowly

⁵The entropy of the radiative zone does increase over time, but much slower than the evolution of the burst, see [Hanawa & Sugimoto \(1982\)](#).

decreasing over time. On its own, this behavior is easily explained by the dredge-up of iron from below, which increases the mean molecular weight faster than the temperature increases from nuclear burning. Nevertheless, it hints at another mechanism for the growth of the CZ. The answer starts in the inset of Figure 4.4. We see that above the convective boundary, the fluid is becoming cooler than the initial RZ. Heat is being transported away from this region by a mechanism which we describe below. This reduces the entropy of the RZ, allowing it to match to the CZ at smaller and smaller column depths—this is how the CZ grows.

In Figure 4.6, we look at different properties of the flow near the convective boundary, at $t = 45$ ms. In the top panel, we notice a temperature bump above the convective boundary. This bump is also clearly seen in Figure 4.4. The origin of this temperature excess is a spike in burning at the same location, as seen by the red dashed line. This is the same spike which appears in the second row, middle panel of Figure 4.3, and is a result of the proton captures onto ^{12}C and ^{13}N . Indeed, in the middle of Figure 4.6, we see that the rms of v_z , the vertical component of the convective velocity, does not go to zero at the convective boundary; despite strong deceleration, some amount of fluid is crossing the boundary and reaching all the way to the hydrogen layer at $y = y_d$. This is how carbon, generated from helium burning at the bottom of the CZ, is able to travel to the hydrogen layer. This is confirmed by the third panel in which we show the horizontal and time average of the carbon flux $F_C \equiv \rho v_z X(^{12}\text{C})$, which stays positive all the way to y_d . In the other direction, the returning downflows (with $v_z < 0$) preferentially carry with them hydrogen from the top, which results in a negative hydrogen flux F_H . As mentioned in the previous section, hydrogen does not burn only at the boundary; much of it is

able to travel downward many scale heights. We emphasize that this is all *before* the CZ has actually reached the hydrogen layer—due to these overshooting motions, the collision is initiated earlier than prescribed by the Schwarzschild criterion.

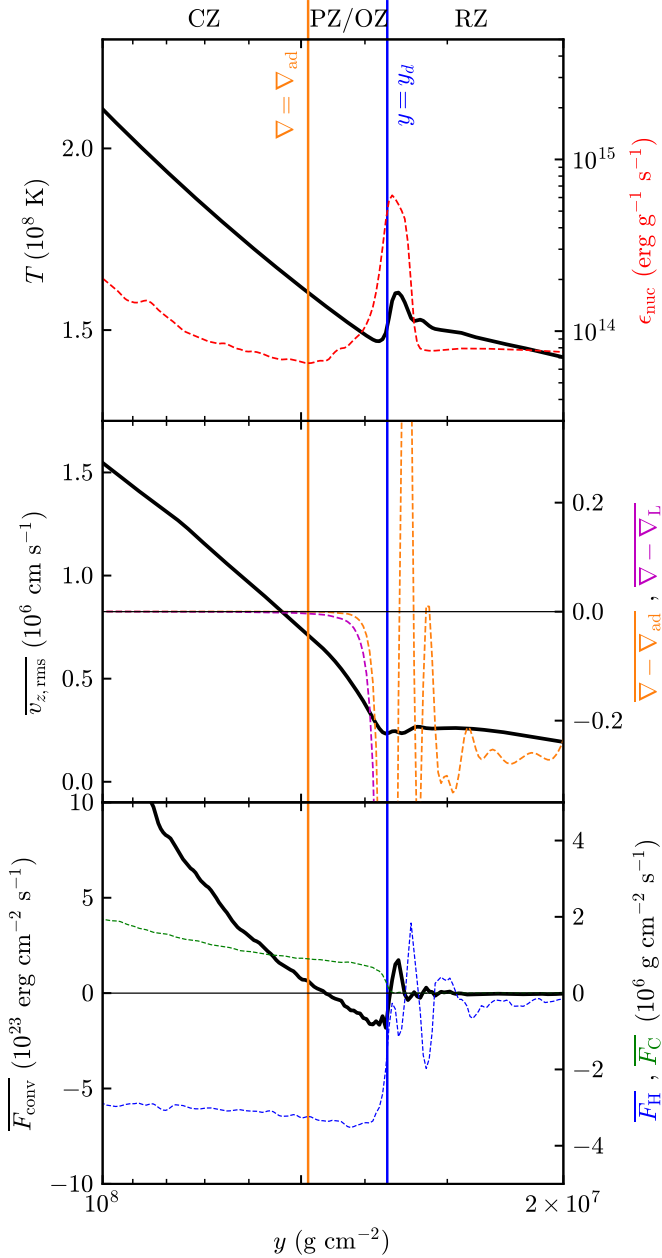


Figure 4.6: Bulk properties of the flow around the interface between the convective and stable zone prior to the collision, i.e. a moment where this boundary is below the hydrogen layer (at a column depth $y > y_d$, the vertical blue line). In each panel, the solid black line and the color dashed lines are scaled on the left-hand and right-hand sides respectively. Every quantity is horizontally averaged over the domain and each height. Overbarred quantities are time-averaged over 2 ms. *Top:* temperature profile and burning rate. *Middle:* rms velocity fluctuation and adiabatic excess. The crossing of the dashed orange with zero sets the location of the vertical orange line (Schwarzschild boundary). *Bottom:* convective heat flux and composition fluxes of ${}^1\text{H}$ and ${}^{12}\text{C}$.

Let us now return to the issue of cooling above the convective boundary. In the middle panel of Figure 4.6, we see that ∇ remains just under ∇_{ad} over a short distance

(about 20% of the local scale height), before dropping, as the temperature gradient goes to the initial radiative gradient ∇_{rad} . This structure is well understood in theories of convective boundary mixing. The marginally subadiabatic region above the Schwarzschild boundary is known as the penetrative zone (PZ), while the radiative region above with nonzero vertical velocity is the overshoot zone (OZ) (Anders & Pedersen 2023). In both regions, upflows are expanding adiabatically in a subadiabatic background, thereby cooling their surroundings. As a result, the convective heat flux, $F_{\text{conv}} \equiv \rho c_p v_z \Delta T$, where ΔT is the temperature difference relative to the horizontal mean, is negative, as seen in the third panel of Figure 4.6⁶. Negative heat fluxes in the PZ have been observed in various simulations of convection (e.g. Hurlbut et al. 1986; Singh et al. 1994; Browning et al. 2004), but this is to our knowledge the first time the effect is observed in concert with a growing convection zone. This cooling reduces the entropy in the PZ and allows the underlying CZ to expand outward.

4.3.4 Burst with Initial Carbon

Now, we simulate a burst closer to what we had in MESA, which produced a violent collision. We start with the initial model with carbon presented in Section 4.2.2, and run it on a 6 cm per zone grid. The simulation is not fully converged at this resolution according to our previous findings (see Figure 4.2). However, our aim in this section is only to discuss important differences in the evolution of the burst. To highlight these differences, we select three new special times and show snapshots of the fluid in Figure 4.7.

⁶As a quick check, the heat capacity at y_d is $\approx 10^7$ erg g⁻¹. The timescale to reproduce the observed cooling of $\approx 10^7$ K is $c_p \Delta T / (F/y) \sim 10$ ms, which is consistent with our results.

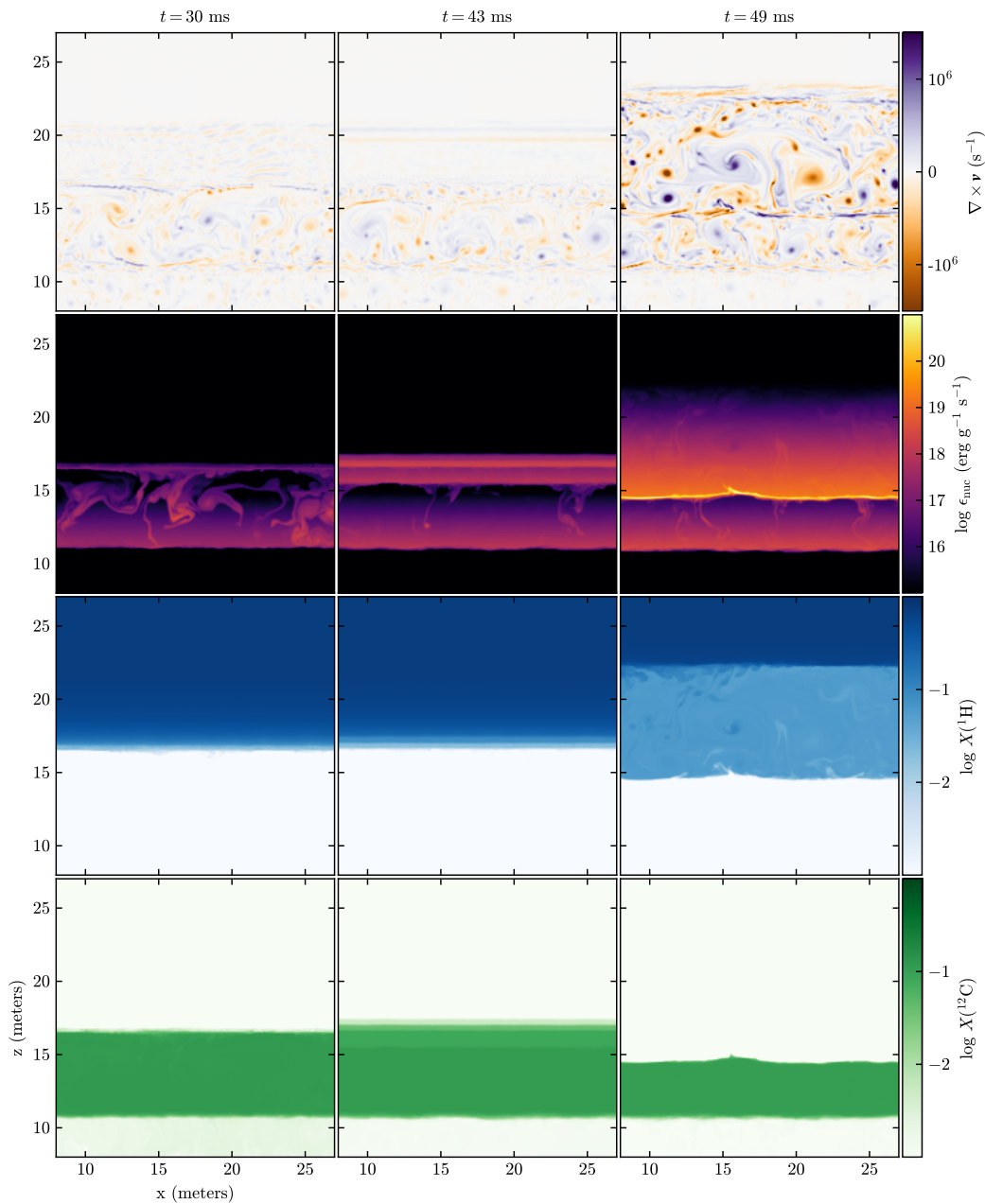


Figure 4.7: Same as Figure 4.3, but for the 6 cm resolution including initial carbon (model B). Note that the scales for nuclear burning and carbon mass fractions are different than in Figure 4.3. We are also showing a larger portion of the box (8–27 m, instead of 8–22 m), to better show the growth of the convection zone. An animated version of this figure is available in the online journal.

The early evolution of the burst is similar to before, with triple- α dominating the energy release. Starting at about 30 ms (left column of Figure 4.7), the effects of the added carbon are already noticeable. As we discussed in the previous section, even before the collision, overshooting motions above the convective boundary cause mixing between the convective and stable layers. The protons coming down now capture much faster, and CNO burning already becomes the dominant source of nuclear energy (see the first column, second row panel of Figure 4.7). This reinforces the idea that the way in which the fuel burns during the burst is very sensitive to the details of mixing at the convective boundary.

At first, burning is slow enough that heat is efficiently distributed throughout the convection zone. As burning becomes faster, the temperature profile begins to increase locally, splitting the convection zone into multiple layers. These layers are well-mixed but have different compositions (see the hydrogen and carbon fractions in the second column of Figure 4.7). Interestingly, we had also found this splitting of the convection zone in our MESA simulations, but it was much more severe. Instead of 3-4 individual layers as we have here, MESA was producing on the order of 10–100 layers, depending on resolution. We had dismissed this splitting as an artifact of the approximate treatment of convection with MLT, but these new simulations indicate that it is real effect. We return to this point in Section 4.4.

The layers are short-lived. Only a few milliseconds later, in what looks like a secondary and much more powerful runaway, the top three layers merge and drastically expand both up and down (third column of Figure 4.7). The downward propagation rapidly consumes the carbon in the bottom convective layer. The burning rate at the interface between the two layers is $\approx 10^{21}$ erg g s $^{-1}$, the highest of any of our

simulations. The top convective boundary moves from $y \approx y_d$ to $\approx 0.1y_d$ in ≈ 1 ms. In MESA, this same expansion occurred in a tenth of the time (see Figure 3 of [Guichardut & Cumming 2023](#)), so in fact the hydrodynamical collision is not as violent as in our 1D simulations, even with a similar ^{12}C fraction. We speculate that this is because we did not include an overshoot prescription in 1D. As we have seen, overshooting motions cause the proton ingestion to begin early, before the Schwarzschild boundary reaches $y = y_d$, and not all at once. The other reason is that we did not consider acceleration-limited convection in 1D, which would have prevented the fluid from spontaneously reaching large velocities, potentially slowing down the expansion of the convection zone.

In the final stage of rapid expansion, 50 ms after the start of the simulation, the Mach number becomes large, averaging at $\sim 8 - 10\%$ and peaking at almost 25% in the upper convection zone. This is pushing the limits of the low-Mach method. We conclude that a fully compressible calculation is needed to study this type of burst, especially when the collision is explosive.

4.4 Summary and Discussion

We have run low-Mach number simulations of X-ray bursts in the regime where helium is igniting and the convection zone eventually reaches new fuel in the form of protons, which accelerates the thermonuclear runaway. Our main findings are as follows:

1. The resolution required to reach convergence is 3 cm per zone or smaller (Figure 4.2). At coarser resolution, the evolution of the burst is delayed due to

improper resolving of the temperature peak.

2. Nuclear burning throughout the burst evolves in a similar fashion to 1D simulations. The burst is initially driven by helium burning. Once protons enter the mix, there is a buildup of ^{13}N , which then quickly burns to ^{14}O , increasing the nuclear energy output (Figure 4.5).
3. The collision is not a single precise moment, but rather a gradual encroaching of the convection zone into the hydrogen shell, which is mediated by convective boundary mixing processes (Figure 4.6). Early on, convective motions penetrate through the convective boundary, exchanging entropy and composition with the stable layer above. A negative heat flux reduces the entropy above the boundary, which allows the convection zone to grow.
4. The evolution of the burst is highly sensitive to the initial amount of carbon in the layer. When it is high, CNO burning dominates the energy release as soon as protons get entrained into the convection zone. The rapid burning leads to a splitting of the convection zone into separate well-mixed layers, which soon merge again in a violent CNO-driven runaway.

In simulating bursts with two different initial fuel compositions, with and without carbon, we have probed two different points in the accretion/ignition parameter space. If the burst were to ignite soon after hydrogen depletion, it would be in a pure He background, as there would be no time to make carbon. For the set of accretion parameters in our MESA simulation, hydrogen depletion was reached after 10 hours, and ignition occurred 5.5 days later. What fraction of this parameter space leads

to violent collisions, and how might this tie to observations? Since hydrodynamical simulations are computationally expensive, this is most likely a question for 1D simulations. We leave this to future work.

Our simulations are not able to follow the full evolution of convection during the burst. This is mainly a dynamic range issue; there is a ~ 4 order of magnitude difference between the density at the bottom of the fuel layer ($y \sim 10^8 \text{ g cm}^{-2}$, $\rho \sim 10^6 \text{ g cm}^{-3}$) and that of the theoretical maximal extent of the convection zone ($y \sim 10^4 \text{ g cm}^{-2}$, $\rho \sim 10^2 \text{ g cm}^{-3}$, e.g. [Weinberg et al. 2006](#)). It is difficult to track this range in the low-Mach approximation because of the need for a velocity-damping region (the sponge) at the top of the model. The smallest value of ρ_{cutoff} which would allow us to evolve the burst for a long time was 10^3 g cm^{-3} . Following the growth of the convection zone into regions of lower density therefore likely requires a fully compressible fluid simulation. These will allow us to constrain the duration of the observed “pause” as in SAX J1808.4–3658 ([Bult et al. 2019](#); [Guichandut & Cumming 2023](#)).

Our simulations did not include thermal diffusion. Although this is possible with MAESTROeX, it is not expected to be a big effect in the early stages of the burst, where convection is taking place at high densities and the conductivity is small. However, it is thermal diffusion which ultimately stops the advancement of convection at lower depths, when it becomes more efficient as a means to transport energy than convection. Future simulations will therefore need to include it to describe the full evolution of convection.

In addition, although previous comparisons between 2D and 3D simulations of

bursts have demonstrated good overall agreement in the burst evolution ([Zingale et al. 2015](#)), it is well known that the turbulent flow behaves very differently. In this work, we noticed the presence of large vortices which carry a different composition than the surroundings. These may completely disappear in 3D, which might alter the mixing and burning at different heights. We remark that a fully compressible 3D simulation of this burst is within reach with current computational resources, and we have already started some experiments with the `CASTRO` code ([Almgren et al. 2010](#)) which show a similar early burst evolution as our `MAESTR0eX` simulations. Furthermore, rotation could be important in dictating the flow patterns, as the spin period of accreting neutron stars can be on the order of milliseconds, comparable to the convective turnover time. These effects have recently been explored in the Boussinesq approximation by [Garcia et al. \(2018\)](#), who modeled burning-driven convection over the whole surface of the star.

Another potential impact of dimensionality is in the convective undershoot, which has an important impact on our simulations. As mentioned in Section 4.3.2, the dredge-up of a large amount of iron into the convective layer reduces the nuclear burning rate. Also, a large fraction of the nuclear energy (about 65% in the main 3 cm simulation) is used up to raise the temperature of the bottom layer (Figure 4.4). An interesting comparison can be drawn to the work of [Kercek et al. \(1998\)](#), who simulated 2D thermonuclear runaways on a white dwarf. Similar to us, they found large vortices, heating of the undershoot layer, and a significant dredge-up of the underlying material (see their figures 1, 3b, and 4). In a subsequent 3D study ([Kercek et al. 1999](#)), these effects were much less severe. In our own preliminary 3D calculations, we also find that undershoot and dredge-up are diminished. This is an observation-

ally relevant question, as dredge-up of heavy elements synthesized in previous bursts could have implications for the detection of spectral features in some photospheric radius expansion bursts (in ’t Zand & Weinberg 2010; Kajava et al. 2017; Strohmayer et al. 2019)

Lastly, a complete treatment of Type I X-ray bursts requires not only the vertical but also lateral heat transport around the surface of the neutron star. This is the well-studied flame-propagation problem, which has been applied to pure He (e.g. Cavecchi et al. 2013; Eiden et al. 2020; Chen et al. 2023) and most recently to mixed H/He atmospheres (Johnson & Zingale 2024), but not yet to the H/He layered case of this paper. How does our concept of “collision” fit into this alternate picture? Is the flame fast enough to propagate before convection has had time to connect with the hydrogen shell, or do these processes interact in some other way? We hope our work motivates future explorations into this question.

`MAESTROeX` is open-source and under active development. The code as well as the inputs required to run the simulations presented in this paper can be found at <https://github.com/amrex-Astro/Maestroex>.

We thank J.R. Fuentes for useful discussions on convective boundaries, E.T. Johnson and A. Smith Clark for technical assistance. We also thank the referee for useful comments that led us to appreciate the important role of the initial amount of carbon. This project was borne out of a visit at Stony Brook University, thanks to funding by the Centre de Recherche en Astrophysique du Québec (CRAQ). S.G. is also supported by an NSERC scholarship. The work at Stony Brook was supported by

DOE/Office of Nuclear Physics grant DE-FG02-87ER40317. This work was supported by NSERC Discovery Grant RGPIN-2023-03620. This research used resources of the National Energy Research Scientific Computing Center (NERSC), a Department of Energy Office of Science User Facility using NERSC award NP-ERCAP0027167.

Software: MAESTRO $\text{\textit{eX}}$ ([Nonaka et al. 2010](#)), AMReX ([Zhang et al. 2019](#)), pynucastro ([Smith Clark et al. 2023](#)), NumPy ([Harris et al. 2020](#)), SciPy ([Virtanen et al. 2020](#)), Matplotlib ([Hunter 2007](#)), and yt ([Turk et al. 2011](#)).

Facilities: NERSC

4.5 Appendix: Building the initial model

Our model is an extension of the one used in [Malone et al. \(2014\)](#), in which the main feature is an isentropic zone in the fuel layer which becomes convectively unstable once the simulation begins. For this, we provide the temperature of the “neutron star” T_{star} , i.e. the temperature in the iron substrate, the height H_{star} of this substrate, the temperature and column depth of the base of the fuel layer, T_{base} and y_{base} . At $r = H_{\text{star}}$, the composition transitions from pure iron to the fuel composition with a hyperbolic tangent of width δ (see appendix of [Malone et al. \(2014\)](#)). We set $\delta = 5$ cm so that this transition is thin, but well resolved at the largest grid resolutions.

In [Malone et al. \(2014\)](#), the fuel layer was a mixture of H and He at fixed mass fractions. Here, the composition depends on the radial location. In particular, the mass fraction of hydrogen X depends analytically on the column depth y ([Cumming & Bildsten 2000](#)),

$$X(y) = \max(0, X_0[1 - y/y_d]) \quad (4.5)$$

where X_0 , the initial hydrogen fraction, and y_d , the hydrogen depletion depth, are two more input parameters. At any point during the building of the model, y can be obtained from the pressure, since $p = gy$ in HSE. For the CNO species, we set constant mass fractions of ^{14}O and ^{15}O , with a sum of Z_0 , and a ratio of 70.621/122.266, which is the ratio of beta-decay half-lives of these isotopes ([Kondev et al. 2021](#)). Finally, the He mass fraction is simply $Y = 1 - X - Z_0$.

For the alternate model with an initial amount of carbon (model B), we fit a power law of the form $Z_C(y) = (y/y_C)^{\nabla_C}$ to the ^{12}C mass fraction in the **MESA** model. We tweak y_C such that the total mass of carbon is within 5% of the **MESA** model. Because there is slightly less fuel than in the **MESA** model, this condition requires a slightly larger initial carbon fraction (compare dash-dotted and dotted green lines in Figure 4.1). This is done so that, once the convection zone is mixed, the uniform carbon fraction is similar between the two models (about 10%). The oxygen mass fractions are kept the same as before, and $Y = 1 - X - Z_0 - Z_C$.

The initial temperature profile is also more complicated than in [Malone et al. \(2014\)](#). Above the isentropic zone where the temperature gradient, $\nabla \equiv d \ln T / d \ln y$, is the adiabatic gradient ∇_{ad} , the atmosphere is in radiative equilibrium, $dT^4/dr \propto -F$, where F is the radiative flux, which depends on the depth and nuclear burning from steady-state energy balance, $dF/dy = -\epsilon_{\text{nuc}}$. In practice, instead of solving for an exact temperature profile consistent with the burning, we divide the fuel layer into three zones and obtain the best-fitting value of ∇ in each zone from the **MESA** model. This is illustrated in Figure 4.8. On top of the three ∇ 's, the column depth boundaries between the first and second zones, y_2 , and second and third zones, y_3 , also must be specified as input parameters.

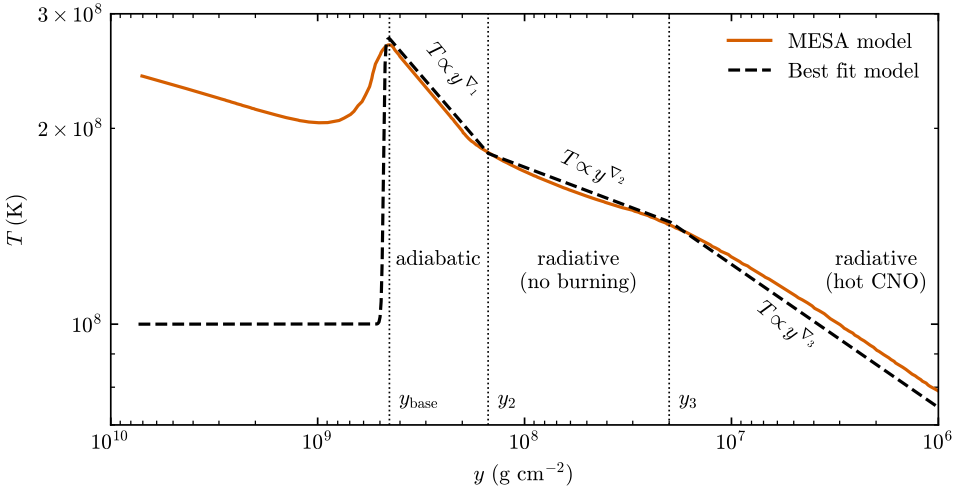


Figure 4.8: Illustration of the temperature profile considered for the toy model. In each zone demarcated by the vertical dotted lines (except for the isothermal substrate at large depths $y > y_{\text{base}}$), the best-fitting temperature gradient $\nabla = d \ln T / d \ln y$ is obtained from the **MESA** model. This temperature profile is then fed into a hydrostatic solver, which determines the density at every point, while the composition is an analytical function of the pressure with Equation (4.5). See text for further details.

In 1D calculations, ignition is manifested by a rapid reduction in the time step which is limited by the nuclear energy generation rate. However, in a fluid simulation, the time step is restricted from the start by the fluid velocity (Courant condition). Therefore, a simulation starting at this point will take a long time (many time steps) to evolve and proceed into the thermonuclear runaway. In order to accelerate it, we “kick” the initial model, i.e. we artificially increase the temperature at the base of the fuel layer (T_{base} parameter), while keeping the temperature gradient in that region ∇_1 constant. As a result, the boundary of the adiabatic region moves according to

$$y'_2 = y_2 \left(\frac{T_{\text{base}}}{T'_{\text{base}}} \right)^{(\nabla_1 - \nabla_2)^{-1}}, \quad (4.6)$$

where the prime (') values are those of the kicked model.

Table 4.1 below lists all of the parameters used to build the initial fluid model.

Table 4.1: Input parameters for initial model

Parameter	Definition	Value	Units
T_{star}	Temperature at the bottom of the atmosphere	10^8	K
H_{star}	Height of the iron substrate	1070	cm
δ	Width of the hyperbolic tangent transition between iron and fuel	5	cm
T_{base}	Temperature at the bottom of the fuel layer	3.5×10^8 ^(a)	K
∇_1	Temperature gradient in the He isentropic zone	0.37 ^(b)	
∇_2	Temperature gradient in the inert He zone	0.12	
∇_3	Temperature gradient in the H-rich zone	0.22	
y_{base}	Column depth at the base of the fuel layer	4.5×10^8	g cm^{-2}
y_2	Column depth boundary between the ∇_1 and ∇_2 zones	5.6×10^7 ^(a)	g cm^{-2}
y_3	Column depth boundary between the ∇_2 and ∇_3 zones	2×10^7	g cm^{-2}
X_0	Hydrogen fraction in the accreted material	0.7	
Z_{O}	Total oxygen ($^{14}\text{O} + ^{16}\text{O}$) mass fraction in the accreted material	0.02	
y_{d}	Hydrogen depletion depth from stable hot CNO burning	3.7×10^7	g cm^{-2}
y_C	Column depth parameter for the carbon fraction ^(c)	5.9×10^8	g cm^{-2}
∇_C	Power law index for the carbon fraction ^(c)	3.16	
T_{cutoff}	Minimum temperature in the model	10^6	K
ρ_{cutoff}	Minimum density in the model	10^3	g cm^{-3}

^(a) These are the values used for the kicked model, i.e. the one shown in Figure 4.1, not Figure 4.8.

^(b) This is approximately the correct value of ∇_{ad} in that region.

^(c) These parameters are ignored in the case of model A (which does not include carbon).

Chapter 5

Discussion and Conclusion

5.1 Summary

In this thesis, we have explored models of photospheric radius expansion type I X-ray bursts during their two main stages: 1) the ignition of the burst in the deep layers of the neutron star atmosphere and the subsequent rise of a convection zone, and 2) the radiatively-driven outflow that begins once the heat reaches the shallow layers.

In Chapter 2, we computed steady-state models of both static expanded envelopes (with base luminosities $L_b^\infty \lesssim L_{\text{Edd}}$) and super-Eddington winds ($L_b^\infty > L_{\text{Edd}}$). For the first time, we included both corrections from general relativity and a transition from optically thick to optically thin. In Chapter 3, we used the stellar evolution code **MESA** to model a source accreting a solar-like gas, leading to a burst igniting in a hydrogen-depleted layer and an outflow with a time-dependent composition. We produced full lightcurves and explored the sensitivity of the results to the treatment of convective boundaries. In Chapter 4, we modeled the same burst, this time in 2D hydrodynamics using the **MAESTROeX** code. We analyzed the nature of the mixing at

the convective boundaries, and how the explosiveness of nuclear burning depends on the composition.

We now summarize our main findings. First, from the observational perspective, we found that:

- Spectral shifts in super-Eddington winds are limited to $\lesssim 2\%$ at the photosphere (Section 2.5.2). If larger shifts are seen, it means that the lines were produced closer to the star, in which case the blueshift contribution from the wind velocity is negligible¹.
- The photospheric radius at touchdown, i.e. when the blackbody temperature peaks, is likely to be extended. In particular if one assumes that the observed luminosity is close to L_{Edd} , then the photosphere may be tens of kilometers above the neutron star surface (Section 2.5.3).
- In sources accreting in the regime where hydrogen burns stably and helium ignites (accretion rate is $0.01\dot{M}_{\text{Edd}} \lesssim \dot{M}_{\text{acc}} \lesssim 0.1\dot{M}_{\text{Edd}}$, recurrence time is \sim days), PRE bursts should quickly hit a pause during the initial rise, followed by a changing slope toward the peak (Section 3.3.4).
- If additional information (e.g. distance to the source, mass of the neutron star) suggests that the peak flux is at the helium Eddington value, then the ratio of peak to pause fluxes should be $(1 + X)$, where X is the hydrogen fraction of the companion.

¹The caveat is that this is in the context of light-element (or otherwise fully ionized) models. Line-driving could still change this conclusion, as we will discuss in Section 5.2.1.

We have also learned many important aspects about the theoretical modelling of these events:

- For the outflow, considering the optically thin regime makes a difference in the location of the photosphere. While in the wind case, $\tau = 3$ is a good approximation for the optical depth of the photosphere, there is a large variation in τ for the static atmospheres (Section 2.3.2). The exception is for very compact, geometrically thin atmospheres, where the usual $\tau = 2/3$ boundary condition is valid.
- In conditions of rapid nuclear burning (where the nuclear timescale is comparable or shorter than the turnover time), mixing-length theory can yield different results for the mixing from convection with either the Schwarzschild or Ledoux criterion (Section 3.4). Convective velocities can also increase on shorter timescales than the code's assumed timestep. To model this convection in 1D, it would be judicious to use a form of acceleration-limited convection, or ideally time-dependent convection. Overshoot mixing should also be included.
- Overshooting convective motions cool the gas above the convective boundary, reducing its entropy (Section 4.3.3). This allows the convection zone to grow faster than prescribed by the increasing entropy due to nuclear heating.
- The explosiveness of the proton-ingestion flash, or collision, depends on the mass fraction of carbon (Section 4.3.4). Depending on ignition conditions, a large portion of this carbon can come from stable nuclear burning prior to the runaway.

5.2 Future Work

After our work, many open questions remain. To name a few “obvious” ones: What do PREs really look like in 3D, as a function of time? How do the metals affect the radiation transfer and the observed spectrum? Which metals and how much of them do we expect in the ejecta, depending on the accretion regime? Where does the convection zone stop growing, and what abundance profiles does it leave behind after it retreats? And finally, how does all of this fit into the bigger picture where ignition happens in one spot and then spreads around the surface? In this section, I will present ideas for continuing each chapter of this thesis, and end with a discussion on future observations.

5.2.1 Outflows

I believe the most pressing work to do when it comes to PRE bursts, and what is most likely to change our understanding of them, is multidimensional wind simulations. Every calculation so far has been in 1D, in assumed spherical symmetry. However we know that many effects will break this symmetry. A high rotation rate can reduce the effective gravity at the equator by a few percent (Section 2.6). To first order, this should make the outflow oblate to some degree. But then how will the radiation propagate in the poloidal direction? Magnetic fields complicate this even more. As we showed, the Alfvén radius could reach > 100 km for expected surface magnetic fields of 10^9 G. Inside of it, we should expect the fluid to follow the magnetic field, carrying away angular momentum into spiral arms ([Weber & Davis 1967](#)). To what degree this may affect the photospheric radius and other observables is unknown.

Radiation magnetohydrodynamics (RadMHD) simulations are widespread nowadays. Open-source codes such as PLUTO (Mignone et al. 2012) and Athena++ (Stone et al. 2020) are being used to study many different systems such as protoplanetary disks, massive star outflows, and accreting black holes (Fuksman & Mignone 2019; Jiang et al. 2018, 2019). A first step for PREs would be to use one of these codes to compute 2D axisymmetric wind models, in a rotating frame. Ultimately, we know that general relativity should also be included; we need GR-RadMHD simulations. As this is also the case in other “hot-topics” such as compact object mergers, dedicated tools are under development, including recently a module for Athena++ (White et al. 2023).

Another way forward would be to model the frequency-dependent radiation transfer in the wind, accounting for metal line transitions. This is very important as it may explain one of the long-standing questions in the field: why are the observed photospheres so small? As we discussed in Section 2.6, the observed r_{ph} in PRE bursts are $< 100 \text{ km}$ (except in the rare superexpansion bursts, see in ’t Zand & Weinberg 2010), whereas outflow models predict the opposite for most possible values of L_b^∞ (Figure 2.8)². in ’t Zand & Weinberg (2010) showed that metals like nickel in the wind, in hydrogen-like form, would experience a radiative acceleration $\gtrsim 100$ larger than the free electrons due to line-driving. This would drive velocities much larger than $0.01c$ and increase the blueshift contribution in comparison to scattering only models.

²In other words, it is unlikely that most PREs are static envelopes rather than winds, as these only exist in a small range of base luminosities ($\sim 0.85L_{\text{Edd}}$ to L_{Edd}).

If only some of the particles in the wind are partially recombined and being accelerated by line-driving, what of the rest of the gas? Momentum transfer from the fast to the slow particles will occur so long as their Coulomb coupling is efficient. In their Section 8.1.2, [Lamers & Cassinelli \(1999\)](#) derive the following simple criterion³,

$$\left(\frac{L}{L_\odot}\right)\left(\frac{v}{\text{km s}^{-1}}\right)\left(\frac{\dot{M}}{\text{M}_\odot \text{yr}^{-1}}\right)^{-1} < 5 \times 10^{17}. \quad (5.1)$$

In our models, $L \sim 10^5 L_\odot$, $v \sim 0.01c$, $\dot{M} \sim 10^{-8} \text{ M}_\odot \text{yr}^{-1}$, and this criterion is easily satisfied. Therefore, we expect the accelerated metals to entrain the other particles with them. At constant $\dot{M} = 4\pi r^2 \rho v$, an increased velocity means a reduction in density. The overall effect will be a truncation of the photosphere, in accordance with observations. We illustrate this in Figure 5.1, where we modify one of our wind models by artificially enhancing the effective opacity. This is just a proof of concept; an entirely different type of calculation is needed to study this effect.

Where bound-bound opacities are dynamically important, Monte Carlo radiation transfer techniques can offer a computational advantage ([Abbott & Lucy 1985](#)). This is its own field with many applications across astrophysics (see [Noebauer & Sim 2019](#), for a recent review). I will simply highlight one such application, which is adjacent to PRE winds. The accretion disks in LMXBs can produce their own thermally-driven winds, sometimes with strong iron absorption lines ([Ueda et al. 2001](#)). Recently, [Tomaru et al. \(2018\)](#) performed Monte Carlo simulations of the radiation in such a wind, and reproduced some features of a spectrum produced by Chandra. It would be interesting to try this for PRE bursts as well. A fully relativistic calculation may not

³Their equation 8.13. We have only changed A to 4 for the helium background, Z to 28 for the accelerated nickel particles, and the oscillator strength f to 0.42 as in [in 't Zand & Weinberg \(2010\)](#).

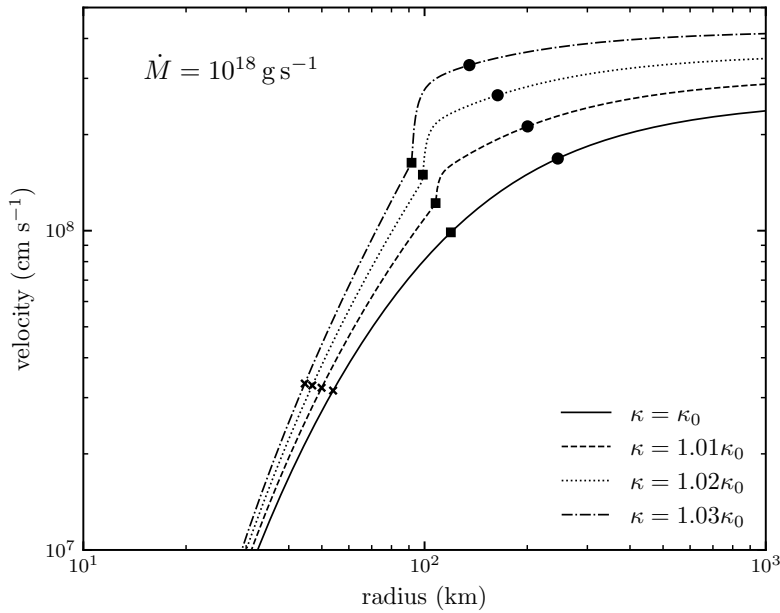


Figure 5.1: Velocity profile of a wind from Chapter 2 (solid line). Starting at an arbitrarily chosen temperature of 10^7 K (square markers), we enhance the opacity by 1%, 2%, and 3% (dashed, dotted, dash-dotted lines). The mass-loss rate is held constant, which is why the models are different even before the modified opacity takes effect. The crosses and dots indicate the location of the sonic point and photosphere in each model. The model with the most enhanced opacity has a its photosphere truncated by 110 km.

be necessary in this case, though gravitational redshift should be included in order to predict accurate spectral lines.

5.2.2 Stellar Evolution Calculations

One-dimensional simulations using stellar evolution codes are the still the best way to probe type I X-ray bursts. They are relatively computationally inexpensive, and allow the inclusion of many physical effects. They are also the only way to model the totality of the burst, including the hydrodynamic wind. Wide parameter space surveys have been performed with KEPLER (Lampe et al. 2016) and MESA (Meisel

2018). However, a detailed survey over PRE bursts is still missing. Yu & Weinberg (2018) explored six models with different ignition depths for pure helium bursts, while we only looked at one ignition depth for a burst with hydrogen. A more complete survey will be useful to investigate which metals are ejected, and in what amounts, depending on the accretion rate.

There are also other relatively unexplored effects which could change our understanding of bursts. Mixing during accretion could be altered by rotational instabilities (Piro & Bildsten 2007; Keek et al. 2009), or sedimentation (Peng et al. 2007). Both of these already have implementations within MESA (Paxton et al. 2011, 2013). Also, large enough magnetic fields could alter or inhibit convection. The relevant range for this effect is $\rho v_{\text{conv}}^2 \leq B^2/8\pi \leq gy$, or $10^9 \text{ G} \lesssim B \lesssim 10^{11} \text{ G}$ at the relevant depths (Bildsten 1995). Some X-ray bursters should exist within this range (e.g Cavecchi et al. 2011). Recently, MacDonald & Petit (2019) implemented magnetic inhibition into stellar evolution calculations of massive star envelopes. It should be straightforward to implement their modified Schwarzschild criterion and heat flux into MESA, and test this effect on burst convection.

5.2.3 Multidimensional Convection

Chapter 4 is a first multidimensional exploration of bursts with a proton-ingestion flash. As we have discussed, the convective velocity can attain some tens of percent of the sound speed, which is pushing the limitations of the low Mach method. Another difficulty with this method is that it requires a velocity-damping region at the top of the box, which prevents us from following the full evolution of convection into the

low density layers. For these reasons, we must part with **MAESTROeX** and run fully compressible calculations. It is also of interest to run 3D calculations in order to get rid of the large vortices. These shear the bottom layer, which caused significant undershoot and iron dredge-up in our simulations, inhibiting the nuclear burning. It is also probable that the vortices affect the rate of growth of the convection zone at the top. These effects make the comparison to 1D results more difficult.

CASTRO is the fully compressible counterpart to **MAESTROeX** (built on the same meshing and microphysics frameworks). We are currently using this code to run 3D simulations of our layered burst, both for initial models A & B (without and with initial carbon). A snapshot of model A is shown in Figure 5.2. As we expected, large vortices have disappeared, and the undershoot into the iron substrate is much less severe. The downside is obviously the computational time required, both because of smaller timesteps to follow sound waves, and 3D instead of 2D. Instead of a few days, the simulations now take weeks to months at the same resolution (and on superior hardware, as we are now using GPUs instead of CPUs). Although the simulations are still ongoing, they have reached later stages of the burst than the **MAESTROeX** simulations, to a point where the convection zone has crossed the nominal wind ejection column $y_w \sim 10^6 \text{ g cm}^{-2}$. Whatever the final outcome of convection, a pause will be present in the lightcurve, it was not just a 1D artefact.

A common objective with multidimensional simulations of stellar convection is to use the results to constrain the free parameters of mixing-length theory, so that future 1D simulations can be more reliable. For example, determining the mixing-length parameter α_{MLT} usually involves comparing the true convective velocity and temperature fluctuation to the predictions of MLT given the adiabatic excess $\nabla - \nabla_{\text{ad}}$,

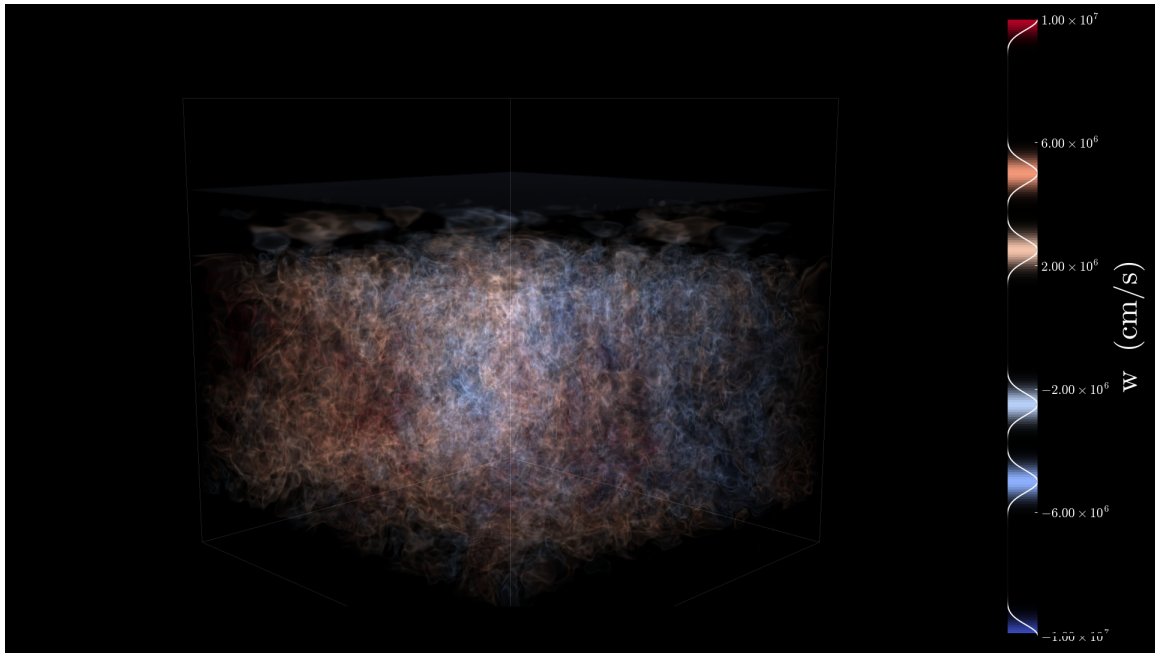


Figure 5.2: Vertical velocity in the convection zone of model A, 0.15 s after ignition. Upflows are in red colors, downflows are in blue colors.

as described in detail by Meakin & Arnett (2007). Other important parameters to be determined are the scale of the overshooting region, and the stiffness of convective boundaries (Cristini et al. 2017). This type of analysis has never been done in the context of X-ray burst convection.

Finally, the other piece of the puzzle is the lateral spreading of the thermonuclear flame over the neutron star surface. (Spitkovsky et al. 2002; Cavecchi et al. 2013; Cavecchi & Spitkovsky 2019). Due to computational limitations, the details of the lateral and vertical heat transport have so far been explored separately. The flame models are especially concerned with the effect of the Coriolis force on the spreading timescale, rather than the detailed nuclear burning and mixing. However recent advances by the Stony Brook group have brought us closer to a more global model (Eiden et al. 2020; Harpole et al. 2021; Zingale et al. 2023; Johnson & Zingale 2024).

The main difference between these works and the type of simulations that we have been running is that the flame simulations use coarse grids in the vertical direction, and assume fully mixed pure helium or hydrogen/helium. In the near future, it will be very interesting to see what the collision looks like in the context of a flame.

5.2.4 Observational Prospects

The main observational application of our work so far has been a single observation of a pause in SAX J1808.4–3658. The fact that there is only one so far could at least partially be attributed to the fact that the pause is expected to be short ($\lesssim 1$ s), and therefore requires both good enough time resolution and a large number of photons to detect with any significance. Still, observations of other pauses would lend much more credence to our model. According to the MINBAR catalogue (Galloway et al. 2020), SAX J1808.4–3658 goes into ~ 1 month-long outbursts every 3 to 4 years, with usually at least one PRE type I X-ray burst. The last outburst was observed by NICER in August 2022, although exceptionally no Type X-ray bursts were seen (Illiano et al. 2023). We will be looking forward to its next activity period, probably in 2025 or 2026. Other interesting candidates, which accrete in the right regime for stable hydrogen burning and show PRE bursts, include:

- 4U 1636–536. The PRE bursts from this source have a bimodal distribution of peak fluxes, separated by a factor ≈ 1.7 (Galloway et al. 2006). The implication is that there is a hydrogen shell which sometimes does gets ejected, other times not. When it does, and the peak flux is at the helium Eddington limit, there should be a pause. Multiple PRE bursts were seen in this source by NICER

from 2017 to 2019 ([Güver et al. 2022](#)). It would be interesting to analyze their lightcurves at high time resolution.

- HETE J1900.1–2455. Bursts were last seen from this source in 2005, during its 1 yr long outburst ([Galloway et al. 2008a](#)). This system is especially interesting as one of the sources for which strong evidence of metal absorption features were seen during PRE ([Kajava et al. 2017](#)).
- GRS 1741.9–2853. This system goes into outburst every ~ 2 yr. The last reported type I X-ray burst were in 2020 ([Pike et al. 2021](#)).
- 4U 1724–307. The last reported type I X-ray burst was in 2009 ([Iwai et al. 2017](#)), even though the LMXB goes into outburst every few months ([Vats et al. 2018](#))

The topic of neutron star radius measurements is still current. With NICER, the state-of-the-art technique has moved to the Bayesian inference of relativistic curvature from rotating surface hot spots ([Bogdanov et al. 2019](#)). This works well when the pulse profile is stable, and the emission is unobscured. As such, the ideal targets are non-accreting, rotation-powered pulsars. So far, the radii of two such objects has been inferred to roughly ± 1 km ([Riley et al. 2019; Miller et al. 2019, 2021](#)). Future X-ray missions will expand this method to neutron stars in other systems. In the next decade, the STROBE-X team ([Ray et al. 2019](#)) is planning to observe accreting millisecond X-ray pulsars, including our favourite PRE burster SAX J1808.4–3658, and measure their radii.

In this context, it would be very interesting, and important, to have another

look at radii from the touchdown method, especially with data coming from NICER and future X-ray missions. Measurements from two independent methods would be stronger if they agree, and indicative of modeling problems if they do not. At this point, we should emphasize that our results from Chapter 2 have not ruled out the touchdown method; they simply challenge the assumption that the photospheric radius r_{ph} at touchdown is exactly the neutron star radius R . It is still possible to infer R , because the method also uses data from the cooling tail of the burst, during which the photosphere is not extended and R appears inside one of the equations (Özel 2006). In fact, Steiner et al. (2010) and Kim et al. (2021) used this method, leaving r_{ph} as a free parameter⁴. They found a larger acceptance rate in their Monte Carlo runs, implying that models with $r_{\text{ph}} > R$ are statistically favored, which is of course consistent with our work. In their calculations, they are initially agnostic about r_{ph} (their prior for the parameter $h \equiv 2R/r_{\text{ph}}$ is uniform from 0 to 2, i.e. $R < r_{\text{ph}} < \infty$). It would be interesting in future work to explore the impact of using a prior on r_{ph} from theory. But once again, what we need to understand how touchdown really works is hydrodynamical simulations of the wind as it ends and collapses back onto the star.

⁴It is interesting to note that they did not cite Paczynski & Anderson (1986). As a side note, it is unfortunate that this paper seems to not have taken hold in the community, especially given how relevant near-Eddington atmospheres are to the topic of touchdown.

5.3 Final Thoughts

The variety of topics and numerical methods used throughout this thesis is testament to the multi-physics nature of type I X-ray bursts. Each stage of the burst, from ignition and nuclear burning to outflows, comes with its own set of challenges and questions. In this thesis, we have taken several steps forward in modeling each of these stages. We have also demonstrated a new way to probe the fluid motions in the neutron star atmosphere from burst observations.

As I have discussed in this chapter, there are still many improvements to be made to our models in order to explain the observations. It is fair to say that us type I X-ray bursts modelers are a bit behind our thermonuclear colleagues, who for example have been studying core-collapse & type Ia supernovae and classical novae using 3D simulations for many years now. With all of the necessary tools at our disposal, and in the face of many thousands of catalogued bursts and upcoming observations, we now need to take a leap forward toward fully global burst models.

References

- Abbott, D. C., & Lucy, L. B. 1985, ApJ, 288, 679
- Abbott, R., Abbott, T. D., Acernese, F., et al. 2023, PhRvX, 13, 011048
- Almgren, A. S., Bell, J. B., Rendleman, C. A., & Zingale, M. 2006a, ApJ, 637, 922
- . 2006b, ApJ, 649, 927
- Almgren, A. S., Beckner, V. E., Bell, J. B., et al. 2010, ApJ, 715, 1221
- Anders, E. H., Jermyn, A. S., Lecoanet, D., et al. 2022, Res. Notes AAS, 6, 41
- Anders, E. H., & Pedersen, M. G. 2023, Galaxies, 11, 56
- Baldo, M., & Burgio, G. F. 2012, RPPh, 75, 026301
- Bhattacharya, D., & van den Heuvel, E. 1991, PhR, 203, 1
- Bildsten, L. 1995, ApJ, 438, 852
- . 1998, in Many Faces Neutron Stars, ed. R. Buccieri, J. van Paradijs, & M. A. Alpar (Dordrecht: Kluwer), 419–449
- Bildsten, L., Chang, P., & Paerels, F. 2003, ApJ, 591, L29
- Bionta, R. M., Blewitt, G., Bratton, C. B., et al. 1987, PhRvL, 58, 1494
- Bogdanov, S., Lamb, F. K., Mahmoodifar, S., et al. 2019, ApJL, 887, L26
- Brown, E. F. 2000, ApJ, 531, 988
- Browning, M. K., Brun, A. S., & Toomre, J. 2004, ApJ, 601, 512
- Bult, P., Jaisawal, G. K., Güver, T., et al. 2019, ApJ, 885, L1
- Cavecchi, Y., & Spitkovsky, A. 2019, ApJ, 882, 142

- Cavecchi, Y., Watts, A. L., Braithwaite, J., & Levin, Y. 2013, MNRAS, 434, 3526
- Cavecchi, Y., Patruno, A., Haskell, B., et al. 2011, ApJ, 740, L8
- Chang, P., Bildsten, L., & Wasserman, I. 2005, ApJ, 629, 998
- Chen, Z., Zingale, M., & Eiden, K. 2023, ApJ, 955, 128
- Chomiuk, L., Metzger, B. D., & Shen, K. J. 2021, ARA&A, 59, 391
- Clarkson, O., & Herwig, F. 2021, MNRAS, 500, 2685
- Clayton, D. D. 1983, Principles of stellar evolution and nucleosynthesis (University of Chicago Press, Chicago)
- Cox, J. P., & Giuli, R. T. 1968, Principles of stellar structure (New York: Gordon and Breach)
- Cristini, A., Meakin, C., Hirschi, R., et al. 2017, MNRAS, 471, 279
- Cumming, A. 2003, ApJ, 595, 1077
- Cumming, A., & Bildsten, L. 2000, ApJ, 544, 453
- Cyburt, R. H., Amthor, A. M., Ferguson, R., et al. 2010, ApJS, 189, 240
- Damen, E., Magnier, E., Lewin, W. H., et al. 1990, A&A, 237, 103
- Davis, A., Jones, S., & Herwig, F. 2019, MNRAS, 484, 3921
- Drout, M. R., Piro, A. L., Shappee, B. J., et al. 2017, Science, 358, 1570
- Durran, D. R. 1989, J. Atmos. Sci., 46, 1453
- Ebisuzaki, T., Hanawa, T., & Sugimoto, D. 1983, PASJ, 35, 17
- Eiden, K., Zingale, M., Harpole, A., et al. 2020, ApJ, 894, 6
- Fan, D., Nonaka, A., Almgren, A. S., Harpole, A., & Zingale, M. 2019, ApJ, 887, 212
- Flammang, R. A. 1984, MNRAS, 206
- Fowler, W. A. 1964, RvMP, 36, 1104
- Fransson, C., Barlow, M. J., Kavanagh, P. J., et al. 2024, Science, 383, 898
- Fujimoto, M. Y., Hanawa, T., & Miyaji, S. 1981, ApJ, 247, 267

- Fujimoto, M. Y., Sztajno, M., Lewin, W. H. G., & van Paradijs, J. 1987, *ApJ*, 319, 902
- Fuksman, J. D. M., & Mignone, A. 2019, *ApJS*, 242, 20
- Gabriel, M., Noels, A., Montalbán, J., & Miglio, A. 2014, *A&A*, 569, A63
- Galloway, D. K., & Cumming, A. 2006, *ApJ*, 652, 559
- Galloway, D. K., Goodwin, A. J., & Keek, L. 2017, *PASA*, 34, e019
- Galloway, D. K., & Keek, L. 2021, in *Timing Neutron Stars Pulsations, Oscil. Explos.*, ed. T. M. Belloni, M. Mendez, & C. Zhang (Springer, Berlin, Heidelberg), 209–262
- Galloway, D. K., Muno, M. P., Hartman, J. M., Psaltis, D., & Chakrabarty, D. 2008a, *ApJS*, 179, 360
- Galloway, D. K., Öznel, F., & Psaltis, D. 2008b, *MNRAS*, 387, 268
- Galloway, D. K., Psaltis, D., Muno, M. P., & Chakrabarty, D. 2006, *ApJ*, 639, 1033
- Galloway, D. K., in 't Zand, J. J. M., Chenevez, J., et al. 2020, *ApJS*, 249, 32
- Garcia, F., Chambers, F. R. N., & Watts, A. L. 2018, *PhRvF*, 3, 123501
- Gendreau, K. C., Arzoumanian, Z., & Okajima, T. 2012, *Proc. SPIE*, 8443, 844313
- Goodwin, A. J., Galloway, D. K., Heger, A., Cumming, A., & Johnston, Z. 2019, *MNRAS*, 490, 2228
- Grindlay, J., Gursky, H., Schnopper, H., et al. 1976, *ApJ*, 205, L127
- Guichandut, S. 2020, Master's thesis, McGill University
- Guichandut, S., & Cumming, A. 2023, *ApJ*, 954, 54
- Guichandut, S., Cumming, A., Falanga, M., Li, Z., & Zamfir, M. 2021, *ApJ*, 914, 49
- Guichandut, S., Zingale, M., & Cumming, A. 2024, *ApJ*, 975, 250
- Güver, T., Bostancı, Z. F., Boztepe, T., et al. 2022, *ApJ*, 935, 154
- Hanawa, T., & Sugimoto, D. 1982, *PASJ*, 34, 1
- Hansen, C. J., & van Horn, H. M. 1975, *ApJ*, 195, 735

- Harpole, A., Ford, N. M., Eiden, K., et al. 2021, ApJ, 912, 36
- Harris, C. R., Millman, K. J., van der Walt, S. J., et al. 2020, Nature, 585, 357
- Heger, A., Fryer, C. L., Woosley, S. E., Langer, N., & Hartmann, D. H. 2003, ApJ, 591, 288
- Henyey, L., Vardya, M. S., & Bodenheimer, P. 1965, ApJ, 142, 841
- Herrera, Y., Sala, G., & José, J. 2020, A&A, 638, A107
- Herwig, F., Pignatari, M., Woodward, P. R., et al. 2011, ApJ, 727, 89
- Herwig, F., Woodward, P. R., Lin, P.-H., Knox, M., & Fryer, C. 2014, ApJ, 792, L3
- Hirata, K., Kajita, T., Koshiba, M., et al. 1987, PhRvL, 58, 1490
- Hunter, J. D. 2007, CSE, 9, 90
- Hurlburt, N. E., Toomre, J., & Massaguer, J. M. 1986, ApJ, 311, 563
- Iben, I., & Renzini, A. 1983, ARA&A, 21, 271
- Illiano, G., Papitto, A., Sanna, A., et al. 2023, ApJL, 942, L40
- in 't Zand, J. J. M., Cumming, A., van der Sluys, M. V., Verbunt, F., & Pols, O. R. 2005, A&A, 441, 675
- in 't Zand, J. J. M., Homan, J., Keek, L., & Palmer, D. M. 2012, A&A, 547, A47
- in 't Zand, J. J. M., & Weinberg, N. N. 2010, A&A, 520, A81
- Iwai, M., Dotani, T., Ozaki, M., et al. 2017, PASJ, 69, 1
- Jahoda, K., Swank, J. H., Giles, A. B., et al. 1996, in Proc. SPIE, ed. O. H. W. Siegmund & M. A. Gummin, Vol. 2808, 59–70
- Jermyn, A. S., Bauer, E. B., Schwab, J., et al. 2023, ApJS, 265, 15
- Jiang, Y. F., Cantiello, M., Bildsten, L., et al. 2018, Nature, 561, 498
- Jiang, Y.-F., Stone, J. M., & Davis, S. W. 2019, ApJ, 880, 67
- Johnson, E. T., & Zingale, M. 2024, J. Phys. Conf. Ser., 2742, 012005
- José, J., Moreno, F., Parikh, A., & Iliadis, C. 2010, ApJS, 189, 204

- Joss, P. C. 1977, *Nature*, 270, 310
- . 1978, *ApJ*, 225, L123
- Joss, P. C., & Melia, F. 1987, *ApJ*, 312, 700
- Joss, P. C., Salpeter, E., & Ostriker, J. 1973, *ApJ*, 181, 429
- Kaiser, E. A., Hirschi, R., David Arnett, W., et al. 2020, *MNRAS*, 496, 1967
- Kajava, J. J. E., Nätilä, J., Poutanen, J., et al. 2017, *MNRAS*, 464, L6
- Kato, M. 1983, *PASJ*, 35, 33
- . 1986, *PASJ*, 38, 29
- Kato, M., & Hachisu, I. 1994, *ApJ*, 437, 802
- Keek, L., & Heger, A. 2015, *MNRAS*, 456, L11
- Keek, L., Langer, N., & In't Zand, J. J. 2009, *A&A*, 502, 871
- Keek, L., Arzoumanian, Z., Chakrabarty, D., et al. 2018, *ApJL*, 856, L37
- Kercek, A., Hillebrandt, W., & Truran, J. W. 1998, *A&A*, 337, 379
- . 1999, *A&A*, 345, 831
- Kim, M., Kim, Y. M., Sung, K. H., Lee, C. H., & Kwak, K. 2021, *A&A*, 650, 1
- Kippenhahn, R., Weigert, A., & Weiss, A. 2012, *Astronomy and Astrophysics Library*, Vol. 192, *Stellar Structure and Evolution*, 2nd edn. (Berlin, Heidelberg: Springer)
- Kondev, F. G., Wang, M., Huang, W. J., Naimi, S., & Audi, G. 2021, *Chinese Phys. C*, 45, 15
- Kuulkers, E., den Hartog, P. R., in 't Zand, J. J. M., et al. 2003, *A&A*, 399, 663
- Lamb, D. Q., & Lamb, F. K. 1978, *ApJ*, 220, 291
- Lamers, H. J. G. L. M., & Cassinelli, J. P. 1999, *Introduction to Stellar Winds* (Cambridge, UK: Cambridge University Press), 452
- Lampe, N., Heger, A., & Galloway, D. K. 2016, *ApJ*, 819, 46
- Langer, N. 1991, *A&A*, 252, 669

- Larson, R. B. 1969, MNRAS, 145, 297
- Lattimer, J. M. 2012, AR, 62, 485
- Lattimer, J. M., & Prakash, M. 2004, Science, 304, 536
- Ledoux, W. P. 1947, ApJ, 105, 305
- Levermore, C. 1984, JQRST, 31, 149
- Levermore, C. D., & Pomraning, G. C. 1981, ApJ, 248, 321
- Lewin, W. H. G., van Paradijs, J., & Taam, R. E. 1993, SSRv, 62, 223
- Li, Z., Suleimanov, V. F., Poutanen, J., et al. 2018, ApJ, 866, 53
- Lin, D. J., Bayliss, A., & Taam, R. E. 2006, ApJ, 653, 545
- MacDonald, J., & Petit, V. 2019, MNRAS, 487, 3904
- Malone, C. M., Nonaka, A., Almgren, A. S., Bell, J. B., & Zingale, M. 2011, ApJ, 728, 118
- Malone, C. M., Zingale, M., Nonaka, A., Almgren, A. S., & Bell, J. B. 2014, ApJ, 788, 115
- Marigo, P., Girardi, L., Chiosi, C., & Wood, P. R. 2001, A&A, 371, 152
- Meakin, C. A., & Arnett, D. 2007, ApJ, 667, 448
- Meisel, Z. 2018, ApJ, 860, 147
- Mignone, A., Zanni, C., Tzeferacos, P., et al. 2012, ApJS, 198, 7
- Miller, M. C., Lamb, F. K., Dittmann, A. J., et al. 2019, ApJL, 887, L24
- . 2021, ApJL, 918, L28
- Niedzwiecki, A., & Zdziarski, A. A. 2006, MNRAS, 365, 606
- Nobili, L., Turolla, R., & Lapidus, I. 1994, ApJ, 433, 276
- Noebauer, U. M., & Sim, S. A. 2019, Living Rev. Comput. Astrophys., 5, 1
- Nonaka, A., Almgren, A. S., Bell, J. B., et al. 2010, ApJS, 188, 358
- Oppenheimer, J. R., & Volkoff, G. M. 1939, Phys. Rev., 55, 374

- Özel, F. 2006, *Nature*, 441, 1115
- Özel, F., & Freire, P. 2016, *ARA&A*, 54, 401
- Özel, F., Psaltis, D., Guver, T., et al. 2016, *ApJ*, 820, 28
- Paczynski, B. 1971, *ARA&A*, 9, 183
- . 1983, *ApJ*, 267, 315
- Paczynski, B., & Anderson, N. 1986, *ApJ*, 302, 1
- Paczynski, B., & Proszynski, M. 1986, *ApJ*, 302, 519
- Page, D., Beznogov, M. V., Garibay, I., et al. 2020, *ApJ*, 898, 125
- Parikh, A., José, J., Sala, G., & Iliadis, C. 2013, *PrPnP*, 69, 225
- Park, M. G. 2006, *MNRAS*, 367, 1739
- Parker, E. N. 1963, *Interplanetary dynamical processes* (New York: Interscience Publishers)
- Pavlov, G., Shibanov, Y. . A., & Zavlin, V. 1991, *MNRAS*, 253, 193
- Paxton, B., Bildsten, L., Dotter, A., et al. 2011, *ApJS*, 192, 3
- Paxton, B., Cantiello, M., Arras, P., et al. 2013, *ApJS*, 208, 4
- Paxton, B., Marchant, P., Schwab, J., et al. 2015, *ApJS*, 220, 15
- Paxton, B., Schwab, J., Bauer, E. B., et al. 2018, *ApJS*, 234, 34
- Paxton, B., Smolec, R., Schwab, J., et al. 2019, *ApJS*, 243, 10
- Peng, F., Brown, E. F., & Truran, J. W. 2007, *ApJ*, 654, 1022
- Pike, S. N., Harrison, F. A., Tomsick, J. A., et al. 2021, *ApJ*, 918, 9
- Piro, A. L., & Bildsten, L. 2007, *ApJ*, 663, 1252
- Podsiadlowski, P. 2014, in *Accretion Processes in Astrophysics*, ed. I. González Martínez-Páis, T. Shahbaz, & J. Casares Velázquez (Cambridge University Press), 45—88
- Poutanen, J. 2017, *ApJ*, 835, 119
- Quinn, T., & Paczynski, B. 1985, *ApJ*, 289, 634

- Rahman, N., Just, O., & Janka, H.-T. 2019, MNRAS, 490, 3545
- Ray, P. S., Arzoumanian, Z., Ballantyne, D., et al. 2019, arXiv e-prints, arXiv:1903.03035
- Riley, T. E., Watts, A. L., Bogdanov, S., et al. 2019, ApJL, 887, L21
- Savonije, G. J. 1978, A&A, 62, 317
- Schatz, H., Bildsten, L., Cumming, A., & Ouellette, M. 2003, Nucl. Phys. A, 718, 247
- Schatz, H., Bildsten, L., Cumming, A., & Wiescher, M. 1999, ApJ, 524, 1014
- Shaposhnikov, N., & Titarchuk, L. 2002, ApJ, 567, 1077
- Singh, H. P., Roxburgh, I. W., & Chan, K. L. 1994, A&A, 281, L73
- Smith Clark, A., Johnson, E. T., Chen, Z., et al. 2023, ApJ, 947, 65
- Spitkovsky, A., Levin, Y., & Ushomirsky, G. 2002, ApJ, 566, 1018
- Steiner, A. W., Lattimer, J. M., & Brown, E. F. 2010, ApJ, 722, 33
- Stephens, D., Herwig, F., Woodward, P., et al. 2021, MNRAS, 504, 744
- Stone, J. M., Tomida, K., White, C. J., & Felker, K. G. 2020, ApJS, 249, 4
- Strohmayer, T., & Bildsten, L. 2006, in Compact Stellar X-ray Sources, ed. W. Lewin & M. van der Klis (Cambridge University Press), 113–156
- Strohmayer, T. E., & Brown, E. F. 2002, ApJ, 566, 1045
- Strohmayer, T. E., Altamirano, D., Arzoumanian, Z., et al. 2019, ApJL, 878, L27
- Sugimoto, D., Ebisuzaki, T., & Hanawa, T. 1984, PASJ, 36, 839
- Suleimanov, V., Poutanen, J., & Werner, K. 2011, A&A, 527, A139
- Suleimanov, V. F., Poutanen, J., & Werner, K. 2020, A&A, 639, 1
- Taam, R. E., & Picklum, R. E. 1978, ApJ, 224, 210
- . 1979, ApJ, 233, 327
- Thorne, K. S., Flammang, R. A., & Zytkow, A. N. 1981, MNRAS, 194, 475
- Timmes, F. X., & Swesty, F. D. 2000, ApJS, 126, 501

- Titarchuk, L. 1994, ApJ, 429, 340
- Tomaru, R., Done, C., Odaka, H., Watanabe, S., & Takahashi, T. 2018, MNRAS, 476, 1776
- Turk, M. J., Smith, B. D., Oishi, J. S., et al. 2011, ApJS, 192, 9
- Turolla, R., Nobili, L., & Calvani, M. 1986, ApJ, 303, 573
- Ueda, Y., Asai, K., Yamaoka, K., Dotani, T., & Inoue, H. 2001, ApJ, 556, L87
- Vats, S., Wijnands, R., Parikh, A. S., et al. 2018, MNRAS, 477, 2494
- Virtanen, P., Gommers, R., Oliphant, T. E., et al. 2020, NatMe, 17, 261
- Wallace, R. K., & Woosley, S. E. 1981, ApJS, 45, 389
- Wallace, R. K., Woosley, S. E., & Weaver, T. A. 1982, ApJ, 258, 696
- Weber, E. J., & Davis, L. J. 1967, ApJ, 148, 217
- Weinberg, N. N., Bildsten, L., & Schatz, H. 2006, ApJ, 639, 1018
- White, C. J., Mullen, P. D., Jiang, Y.-F., et al. 2023, ApJ, 949, 103
- Wijnands, R., & Van Der Klis, M. 1998, Nature, 394, 344
- Wolf, B., & Schwab, J. 2017, py_mesa_reader, doi:10.5281/zenodo.826958
- Wood, P. R. 1974, ApJ, 190, 609
- Woodward, P. R., Herwig, F., & Lin, P.-H. 2014, ApJ, 798, 49
- Woosley, S. E., Heger, A., & Weaver, T. A. 2002, RvMP, 74, 1015
- Woosley, S. E., & Weaver, T. A. 1986, ARA&A, 24, 205
- Woosley, S. E., Heger, A., Cumming, A., et al. 2004, ApJS, 151, 75
- Yakovlev, D. G. 2016, Int. J. Mod. Phys. A, 31, 1641017
- Yu, H., & Weinberg, N. N. 2018, ApJ, 863, 53
- Zhang, W., Almgren, A., Beckner, V., et al. 2019, J. Open Source Softw., 4, 1370
- Zingale, M., Eiden, K., & Katz, M. 2023, ApJ, 952, 160
- Zingale, M., Malone, C. M., Nonaka, A., Almgren, A. S., & Bell, J. B. 2015, ApJ, 807, 60